Autorul tezei de abilitare: Conf. Dr. LAURA FLOROIAN
Titlul tezei de abilitare: ASPECTE GENERALE ȘI PARTICULARE ÎN MĂSURĂTORILE ELECTRONICE DIN DOMENIUL NANOMATERIALELOR
Domeniul: Inginerie electronică, telecomunicații şi tehnologii informaționale

PORTOFOLIU LUCRĂRI

1. Ginerica, C., Zaha, M., Floroian, L., Cojocaru, D., Grigorescu, S. A Vision Dynamics Learning Approach to Robotic Navigation in Unstructured Environments, Robotics 2024, 13, 15, ISSN: 2218-6581 (Factor de Impact: 2,9) https://doi.org/10.3390/robotics13010015

2. Cotfas D.T., Cotfas P. A., Floroian D., Floroian L., *Accelerated life test for photovoltaic cells using concentrated light*, International Journal of Photoenergy, 2016, Article ID 9825683, 7 pages, ISSN:1110-662X, (Factor de Impact: 2,535), http://dx.doi.org/10.1155/2016/98256832016

3. D.T. Cotfas ; P.A Cotfas ; D. Floroian ; L. Floroian ; Mihai Cernat, *Ageing of Photovoltaic Cells Under Concentrated Light*, IEEExplore, 2015 Intl Aegean Conference on Electrical Machines & Power Electronics (ACEMP), 2015 Intl Conference on Optimization of Electrical & Electronic Equipment (OPTIM) & 2015 Intl Symposium on Advanced Electromechanical Motion Systems (ELECTROMOTION), DOI:10.1109/OPTIM.2015.7427048

4. D.T. Cotfas; D. Floroian, P.A Cotfas ; L. Floroian, Rubin, R., Lieberman, D., *The study of the photovoltaic cells parameters in concentrated sunlight*, IEEExplore, mai 2014, DOI: 10.1109/OPTIM.2014.6850916, Print ISSN: 1842-0133, https://ieeexplore.ieee.org/document/6850916

5. Floroian, D., Floroian, L., Rubin, R., Lieberman, D., Cotfas, P., Cotfas, D., Ursuțiu, D., Samoilă, C., *Measurements in concentrated sun using a remote controlled robot*, International Journal of Online Engineering, vol.4., pp. 50-55, 2013, ISSN: 1868-1646, http://online-journals.org/i-joe/article/view/2544

6. Cotfas P.A., Cotfas D. T., Floroian L., Floroian D., *General Physics Remote Laboratory based on the NI ELVIS Platform and Moodle*, IEEExplore, apr. 2014, ISBN: 978-1-4799-2024-2, DOI: 10.1109/REV.2014.6784244, https://ieeexplore.ieee.org/document/6784244

7. S. Coman, C. Boldisor, L. Floroian, *Fractional adaptive control for a fractional - order insuline - glucose dynamic model*, IEEExplore, 2017, DOI: 10.1109/OPTIM.2017.7975082, ISBN:978-1-5090-4489-4, https://ieeexplore.ieee.org/document/7975082

8. Floroian L., Ristoscu C., Candiani G., Pastori N., Moscatelli M., Mihailescu N., Negut I., Badea M., Gilca M., Chiesa R., Mihailescu I.N., *Antimicrobial thin films based on ayurvedic plants extracts embedded in a bioactive glass matrix*, Applied Surface Science, 2017, ISSN:0169-4332 (Factor de Impact: 7,392), http://dx.doi.org/10.1016/j.apsusc.2017.02.197

9. Badea M., Floroian L., Restani P., Cobzac S.C., Moga M., Ochratoxin A Detection on Antibody- Immobilized on BSA-Functionalized Gold Electrodes, PLoS ONE 2016, ISSN:1932-6203, 11(7): e0160021. doi:10.1371/journal.pone.0160021, (Factor de Impact: 3,752) https://www.ncbi.nlm.nih.gov/pubmed/27467684

10. Floroian, D., Ursutiu, D., Moldoveanu F., Floroian, L., *RoboSmith: Wireless Networked Architecture for Multiagent Robotic System*, International Journal of Online Engineering, 6 (4), pp. 14-19, 2010, DOI: 10.3991/ijoe.v6i4.1468, WOS:000422505100003, ISSN 1868-1646, eISSN 1861-2121, (Factor de Impact: 0,13), https://online-journals.org/index.php/i-joe/article/view/1468

10.07.2025

robotics

MDPI

Article

A Vision Dynamics Learning Approach to Robotic Navigation in Unstructured Environments

Cosmin Ginerica [1,*], Mihai Zaha [1], Laura Floroian [1], Dorian Cojocaru [2] and Sorin Grigorescu [1]

[1] Robotics, Vision and Control Laboratory (ROVIS), Transilvania University of Brasov, 500036 Brasov, Romania; mihai.zaha@unitbv.ro (M.Z.); lauraf@unitbv.ro (L.F.); s.grigorescu@unitbv.ro (S.G.)
[2] Electronics and Mechatronics, Department of Automatic Control, University of Craiova, 200585 Craiova, Romania; cojocaru@robotics.ucv.ro
* Correspondence: cosmin.ginerica@unitbv.ro

Abstract: Autonomous legged navigation in unstructured environments is still an open problem which requires the ability of an intelligent agent to detect and react to potential obstacles found in its area. These obstacles may range from vehicles, pedestrians, or immovable objects in a structured environment, like in highway or city navigation, to unpredictable static and dynamic obstacles in the case of navigating in an unstructured environment, such as a forest road. The latter scenario is usually more difficult to handle, due to the higher unpredictability. In this paper, we propose a vision dynamics approach to the path planning and navigation problem for a quadruped robot, which navigates in an unstructured environment, more specifically on a forest road. Our vision dynamics approach is based on a recurrent neural network that uses an RGB-D sensor as its source of data, constructing sequences of previous depth sensor observations and predicting future observations over a finite time span. We compare our approach with other state-of-the-art methods in obstacle-driven path planning algorithms and perform ablation studies to analyze the impact of architectural changes to our model components, demonstrating that our approach achieves superior performance in terms of successfully generating collision-free trajectories for the intelligent agent.

Keywords: deep learning; planning; recurrent neural network; robotics

check for updates

Citation: Ginerica, C.; Zaha, M.; Floroian, L.; Cojocaru, D.; Grigorescu, S. A Vision Dynamics Learning Approach to Robotic Navigation in Unstructured Environments. *Robotics* **2024**, *13*, 15. https://doi.org/10.3390/robotics13010015

Academic Editors: Hong Zhang and Marco Ceccarelli

Received: 3 December 2023
Revised: 2 January 2024
Accepted: 15 January 2024
Published: 17 January 2024

Copyright: © 2024 by the authors. Licensee MDPI, Basel, Switzerland. This article is an open access article distributed under the terms and conditions of the Creative Commons Attribution (CC BY) license (https://creativecommons.org/licenses/by/4.0/).

1. Introduction

One of the most important sub-tasks of autonomous navigation, especially navigation bound to an unstructured environment, is an intelligent agent's ability to perform collision-free path planning. It is paramount that the robot's surroundings are understood to its best ability, such that it can safely navigate in difficult environments. Traditional approaches rely on heuristic rules of handcrafted features for solving the path planning task. However, these methods may not extend well enough in the context of dynamic environments.

With the accelerated development of computing hardware, the Artificial Intelligence domain has also seen an enormous rise in popularity. As a consequence, an alternative approach to self-driving tasks is based on AI algorithms, commonly implemented as deep neural networks. These algorithms, which are usually trained using sensory data acquired from the autonomous agent, show potential in generalizing to new and/or evolving environments.

Some AI-based approaches to the autonomous driving challenge divide the navigation problem into smaller sub-problems and approach them individually. Others model the entire navigation task as a black-box, expecting sensor data inputs and directly outputting vehicle commands. Some of these algorithms use RGB image data in order to detect obstacles in the vicinity of the autonomous agent and plan collision-free trajectories based on the detected obstacles.

In this paper, we propose a different approach for tackling the autonomous navigation problem, by using a recurrent neural network to model the dynamics of the environment

in which the robot navigates. The environment dynamics, in the context of this work, refer to dynamic obstacles present in the scene. Recurrent neural networks are a type of model that can capture temporal dependencies and process sequence data, like objects moving within the scene. By incorporating historic data in the form of previous sensor observations from the mobile robot, a Recurrent Neural Network (RNN) can improve the accuracy and robustness of a collision prediction algorithm, especially in complex, unstructured environments.

We have chosen a recurrent neural network architecture due to its ability to capture temporal dependencies within the input data. This enables the encoding of obstacle dynamics within its layers and allows for using this additional information in the path planning component in order to generate a safer trajectory for the mobile robot.

We conducted our experiments with data collected while the mobile robot shown in Figure 1a was navigating on a forest road, with dynamic obstacles present in its vicinity. Dynamic obstacles were represented by human subjects approaching the mobile robot while it navigated in the forest road environment. Our experiments indicate a better performance than the baseline.

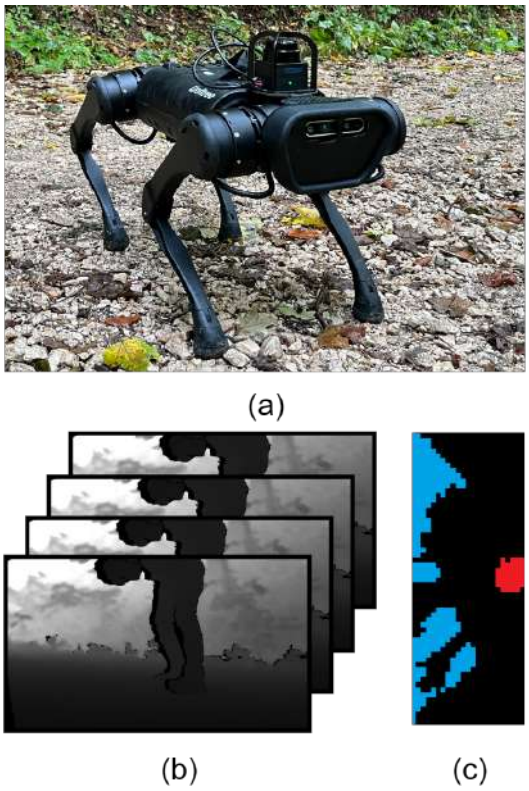

Figure 1. Vision Dynamics–Collision Detection. (**a**) A legged robot navigating in an unstructured environment. (**b**) RGB-D sequence of observations provided as input to a deep neural network. (**c**) Collision detection output as an occupancy birds-eye view grid.

The main contributions of this paper are as follows:

- The deep neural network architecture used to encode the dynamics of the robot's environment and predict future sensor observations based on previously gathered information.
- The self-supervised training of our encoder network with processed sensor information from an RGB-D camera.
- The processing of the acquired RGB-D data in the scope of reducing the search space of the planning algorithm.
- The usage of a custom asymmetrical loss function for training the neural network.

- The path planning component, which incorporates the predicted observations when generating safe trajectories for the mobile robot.

The rest of the work is organized as follows. The related work is covered in Section 2. Our proposed vision dynamics algorithm is presented in Section 3. The experimental setup, a detailed description, and comparisons with other algorithms are presented in Section 4. The conclusions are presented in the final section.

2. Related Work

In recent years, the development of autonomous navigation solutions has seen a rise in popularity in the scientific community, mainly due to the advances of artificial intelligence. Several papers which explore various aspects of the autonomous navigation task, like perception and control, have been published.

Some research treats the entire autonomous navigation problem as a black-box. The proposed algorithms expect sensory information as input to a deep learning model and directly output control signals. For example, one such approach can be found in reference [1], where the authors train a convolutional neural network to directly map pixel information from a monocular camera to vehicle steering commands. This approach tries to simplify the autonomous navigation problem by eliminating the necessity of individual sub-systems like lane marking detection or path planning. Another approach uses the Deep Reinforcement Learning (DRL) technique, where the agent is controlled via action–reward systems and is stimulated to take actions to advance toward its goal, as in [2].

Both End-to-End and DRL approaches show promising results in a controlled simulated environment; however, the deployment of such algorithms in real-world scenarios is difficult, due to the high unpredictability of the environment dynamics.

One example of Deep Reinforcement Learning being used in an unstructured navigation task is the work presented in [3]. The authors used a simulated environment to perform the training of their model, enabling the system to learn navigation policies and then perform transfer learning as *sim-to-real*.

Another example of Reinforcement Learning employed to solve the unstructured navigation problem is presented in [4]. Their proposal contains a framework based on an uncertainty-aware learning based model and a self-supervised traversability estimation model. The traversability model is then integrated with a model predictive controller, which optimizes the vehicle's trajectory while simultaneously avoiding obstacles present in the environment.

Other work relies on object detection algorithms in order to identify obstacles from the scene and to generate collision-free trajectories for the autonomous agent. Given the large number of publicly available driving databases, object detection based on image data is a widely researched area as well. In [5], the authors propose training a state-of-the-art object detector algorithm in the hope of improving performance for self-driving scenarios. Wang et al. proposed a collision detection mechanism based on a convolutional neural network in [6] within the context of autonomous driving. Pramanik et al. proposed an object detection and tracking system which handles video sequences in [7].

More recently, in [8], an obstacle avoidance method was proposed based on object detection, with certain improvements in their model, like in the variable learning rate.

Object detection algorithms have high computational requirements and necessitate various optimizations and improvements before being able to run in real-time. They also face issues such as robustness to occlusions, illumination changes, and object deformation.

Another approach to the autonomous driving challenge, particularly to the collision avoidance strategy, is based on occupancy grids, where the environment is represented as a grid of cells, each cell having an assigned probability that indicates whether or not the respective cell is occupied. Shepei et al. proposed an occupancy grid generation algorithm based on stereo image input in [9]. Their architecture is based on ResNet, trained to highlight static and dynamic obstacles within the scene.

Another type of occupancy grid generation algorithm makes use of LiDAR data instead of stereo cameras, such as the one proposed in [10], where the authors integrate this algorithm into a quadrotor system and perform benchmark flights. Usually, algorithms that handle LiDAR data suffer from high computation costs and limited scalability, as they require the processing of large amounts of data.

Recurrent neural networks have also been in the spotlight for autonomous navigation solutions. For example, the authors of [11] present a multi-step prediction of drivable space in the form of occupancy grid sequences, using an RNN architecture that was trained on the KITTI dataset, in the scope of learning motion-related features from the input sequences.

There are also approaches to the unstructured navigation problem which do not rely on artificial intelligence. One example of such a work is [12], where the authors use *A** for calculating the global trajectory for their robotic platform, combined with a local planner and a reactive planner to ensure that the robot will keep track of the computed global trajectory.

A similar approach for a legged robot without using artificial intelligence is presented in [13]. In this study, the authors propose an end-to-end path planning and navigation system which is used by the robot to navigate in its' environment. The legged robot's trajectory is generated with the use of a nonlinear optimization method.

The method proposed in [14] uses LiDAR data, coupled with an autonomous map-less navigation method based on [15] in order to perform legged robot navigation in an unstructured, urban environment. This approach combines ranging sensing with Deep Reinforment Learning and classical path planning in order for the robot to successfully avoid the dynamic obstacles present in an urban environment.

These works demonstrate the potential of using object detection and deep-learning-based approaches for obstacle avoidance in dynamic environments. However, they still face challenges such as robustness to occlusions, illumination changes, and object deformation. The training process for these object detectors is label-intensive as well. Additionally, some of the methods use expensive sensors (e.g., LiDAR) to map the mobile robot's environment and avoid collisions with obstacles.

Basing our work on [16–18], we propose a vision dynamics approach for solving the unstructured navigation problem for a legged mobile robot, based on processing information coming from an RGB-D sensor through the use of a recurrent neural network which predicts future sensory observations and feeds these observations into a modified DWA algorithm in order to produce an obstacle-free trajectory for the mobile robot. We demonstrate the effectiveness of the approach in a real-world scenario during a navigation task on a forest road.

3. Methodology

The following notation is used throughout this paper. Superscript <*t*> is used to denote a single discrete time step t. For example, a depth sensor measurement at time step t will be written as $\theta^{<t>}$. Predicted values are defined with the hat notation. A predicted observation at time step $t+n$ is defined as $\hat{\theta}^{<t+n>}$. Vectors are represented by bold symbols. A vector of sensor observations is marked as $\mathbf{\Theta}^{<t-\tau,t-1>}$, which represents a series of sensor observations from time step $t-\tau$ to time step $t-1$.

3.1. Problem Definition

Given a set of historical depth sensing observations $\Theta^{<t-\tau,t-1>}$, the current sensor observation $\theta^{<t>}$, the mobile robot's current state $s^{<t>} = [x^{<t>}, y^{<t>}, v^{<t>}, \phi^{<t>}]$, and a global reference trajectory $\mathbf{Z}_{ref}^{<t-\infty,t+\infty>}$, the objective is to construct a recurrent deep neural network model which can encode within its layers the dynamics of the environment and, based on historical sensor observations, can predict future observations for a finite time horizon $[t+1,\ldots,t+n]$, where each time step $t+1, t+2, \ldots$ represents one future sampling time, bound by a time constraint of 100 ms. The agent's belief, modelled with the

neural network, is passed to the path planner algorithm based on the Dynamic Window Approach and a collision-free local trajectory is generated for the mobile robot: $\mathbf{Z}_L^{<t+1,t+n>}$.

Both local and global trajectories are represented as sequences of vehicle states: $\mathbf{Z}_{ref} = \{[x_i, y_i, v_i, \phi_i] | \forall i \in [1, \ldots, N]\}$ and, respectively, $\mathbf{Z}_L = \{[x_i, y_i, v_i, \phi_i] | \forall i \in [1, n]\}$, where x_i and y_i are the Cartesian coordinates of the vehicle, v_i the velocity, and ϕ_i is the orientation angle of the vehicle with respect to its initial orientation. n is the length of the generated local trajectory, $\mathbf{Z}_{ref}$ is the global reference trajectory, and $\mathbf{Z}_L$ is the generated local trajectory.

3.2. Scene Dynamics Encoder Network

The architecture of the encoder model is presented in Figure 2. The observations coming from the RGB-D sensor are not directly processed by the network, but undergo a series of preprocessing operations beforehand, as described in Equations (2)–(4). The input sequence (historic observations) is accumulating in the *Encoder memory unit*, formatted appropriately by the *Sequence formatter* block, and then passed through to the recurrent neural network. The *Clustering unit* clusters the predictions coming from the neural network and eliminates outliers. Encoding scene dynamics involves processing data coming from the RGB-D sensor in order to create a representation of the current scene, as well as predicting the evolution of the scene over a fixed time period. LSTM networks are well suited for encoding scene dynamics due to their ability to learn the temporal dependencies of the input data and use these dependencies for predicting future states.

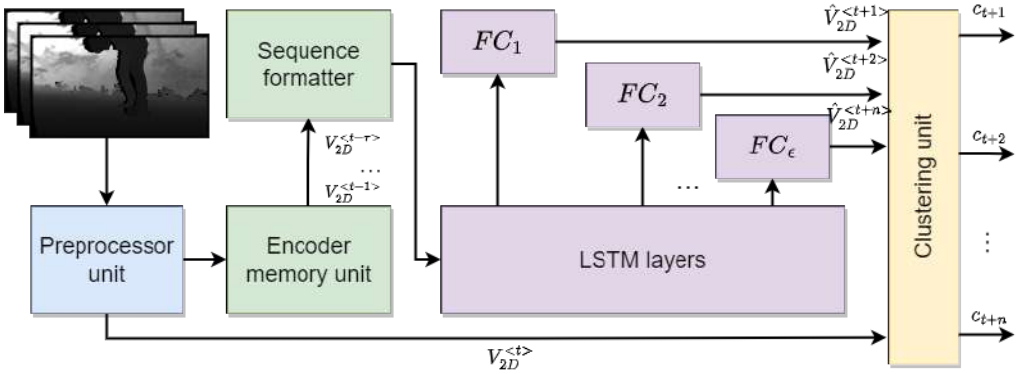

Figure 2. Encoder model architecture. The input of the deep neural network is a sequence of length τ observations coming from the RGB-D sensor.

The encoder model is based on an LSTM architecture which contains multiple cells for processing time-series data in the form of historical depth sensor observations of length τ. The output of the model is a sequence of future observations of length n.

Depth information coming from the RGB-D sensor is not fed directly into the network, but it is processed beforehand.

First, using depth measurements from the sensor and, respectively, the depth camera intrinsic matrix, the three-dimensional environment is recreated:

$$\mathbf{P}_{3D} = \{[X_i, Y_i, Z_i] | \forall i \in \mathbf{D}_{img}\} \tag{1}$$

where X_i, Y_i, and Z_i are the three-dimensional coordinates of the points P; D_{img} is the depth image. For every point in the depth image domain, corresponding $3D$ points are calculated:

$$\begin{aligned} X &= (j - c_x)\frac{z}{f_x} \\ Y &= (i - c_y)\frac{z}{f_y} \\ Z &= z \end{aligned} \tag{2}$$

where j is the column coordinate of the current pixel from the depth image, i is the row coordinate of the current pixel from the depth image, c_x and c_y are the optical center coordinates, f_x and f_y are the focal distance coordinates, and z is the depth value at coordinates (i, j).

Second, only candidate points that are closer than a threshold value are kept:

$$p \Leftarrow p_c \iff T_{min} \leq d(o, p_c) \leq T_{max}, \forall p_c \in P_{3D} \tag{3}$$

where p is the filtered point, p_c is the candidate point, o is the vehicle coordinate system origin, T_{min} is the minimum threshold value, T_{max} is the maximum threshold value, and d is the L2 norm, calculated as $||o - p_c||^2$.

Third, points that are below or above a certain height are eliminated:

$$p \Leftarrow p_c \iff T_{min} \leq Y_{p_c} \leq T_{max}, \forall p_c \in P_{3D} \tag{4}$$

where p is the filtered point, p_c is the candidate point, T_{min} is the minimum threshold value, T_{max} is the maximum threshold value, and Y_{p_c} is the height of the candidate point p_c. Eliminating points below the minimum threshold will also eliminate points that belong to the ground, therefore easing further computation steps.

The resulting point cloud is then converted into a voxel representation in order to reduce the input data dimension:

$$\mathbf{V_{3D}} = \begin{cases} 1 & , if P_i \in v(i, j, k) \\ 0 & , otherwise \end{cases} \tag{5}$$

where $v(i, j, k)$ is a 3D space within the voxel grid.

Furthermore, the voxel representation is then projected onto a top-view occupancy grid:

$$\mathbf{V_{2D}} = \{(X_i, Y_i) | X_i \in V_{3D}, Y_i \in V_{3D}\} \tag{6}$$

These two-dimensional grids accumulate into a historical sequence that is then fed as input to the sequence formatter module from our algorithm.

$$\mathbf{V_{2D}}^{<t-\tau, t-1>} \Leftarrow \{V_{2D}^{<i>}, \forall i \in [t - \tau, t - 1]\} \tag{7}$$

A visual representation of the processing chain applied to the input depth images can be seen in Figure 3. The history sequences $\mathbf{V}_{2D}^{<t-\tau, t-1>}$ are, again, processed by the sequence formatter module, which reshapes them to a suitable format for the LSTM module of our algorithm.

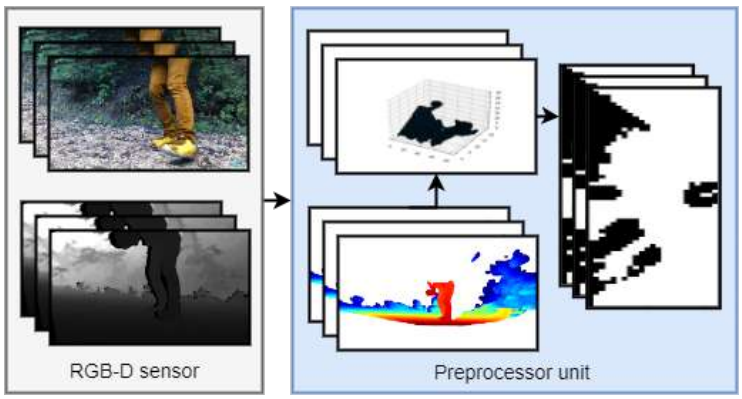

Figure 3. Preprocessing chain. Sensor data coming from the RGB-D camera is processed before being stored into the *Encoder memory unit*. Depth information is reconstructed using the camera intrinsic parameters into a three-dimensional point cloud. The point cloud is then converted to a voxel grid representation. The three-dimensional voxel grid is then projected into a top-down view.

At the heart of the scene dynamics encoder model there is a stacked LSTM module with n layers. The output of each layer is then fed through a series of fully connected layers in order to produce the predictions at time steps $[t+1, \ldots, t+n]$.

The resulting predictions $\hat{\mathbf{V}}_{\mathbf{2D}}^{<t+1,t+n>}$ coming from the neural network, in the form of predicted voxel grids for future time steps $[t+1, \ldots, t+n]$, are passed to the *clustering unit* for further processing. The clustering unit takes each predicted observation $V_{2D}^{<t+i>}$ and performs DBSCAN, according to [19]. The output of this layer is, for each time step $t+i$, a list of centroids plus the object size corresponding to each obstacle present in the current time step. Obstacle points are sampled based on the centroids and sizes provided by the clustering unit for each predicted time step $t+i$ and are accumulated in order to be fed to the DWA algorithm.

The clustering unit also acts as a filter mechanism for the output data, using the *Log Odds* method.

The data processing main workflow is presented in Algorithm 1.

Algorithm 1 Processing loop

Require: $\mathbf{\Theta}^{<t-\tau,t-1>}$
Require: $\theta^{<t>}$ ▷ Current depth sensor observation
Require: $obstacles = \{\}$ ▷ Empty list of obstacles
for $i \in [t-\tau, t]$ **do**
  $P_{3D}^{<i>} \leftarrow$ to_pcl($\theta^{<i>}$)
  $P_{3D}^{<i>} \leftarrow$ reject_outliers($P_{3D}^{<i>}$)
  $V_{3D}^{<i>} \leftarrow$ to_3d_voxel($P_{3D}^{<i>}$)
  $V_{2D}^{<i>} \leftarrow$ project_2d($V_{3D}^{<i>}$)
end for
$m \leftarrow \{V_{2D}^{<i>} | \forall i \in [t-\tau, t-1]\}$
$\hat{\mathbf{V}}_{2D}^{<t+1,t+n>} \leftarrow m(\mathbf{V}_{2D}^{<t-\tau,t-1>})$ ▷ Obtain predictions
$\mathbf{c}_j \leftarrow$ cluster_outputs($\hat{\vec{v}}_{2D}^{<t+1,t+n>}, V_{2D}^{<t>}$) ▷ Cluster outputs
for $j \in [0, c_{len}]$ **do**
  $obstacles \leftarrow c_j$ ▷ Append obstacle
end for

The RNN has been trained in a self-supervised way, over a number of 1000 epochs, using an Adam optimizer with a learning rate of 0.001. The history size used for training was $\tau = 50$ and the prediction horizon size was $n = 30$. This is equivalent to 5 s for the history sequence and 3 s for prediction, respectively. For training the network, we used a total number of 30 K pairs of input historical depth observations and target predictions.

A custom asymmetrical loss function was used, as shown in Equation (8), because of the sparse nature of the output sequence data.

$$L(V, \hat{V}) = \frac{1}{n} \sum_{i=1}^{n} (\hat{V}_i - V_i)^2 [(1 - 1_+)\alpha + 1_+(1 - \alpha)] \tag{8}$$

where α is a scale factor that increases the loss value for predictions that diverge from target values and 1_+ is a function defined as follows:

$$1_+(V, \hat{V}) = \begin{cases} 1 & , \hat{V} - V \geq 0 \\ 0 & , otherwise \end{cases} \tag{9}$$

After experimenting with the architecture and the loss function, the scale factor α was set to 0.1.

A visual representation of the asymmetrical loss function is presented in Figure 4. It can be observed that the function penalizes the model if the predicted voxels are marked as occupied, when, instead, they should be marked as free-space.

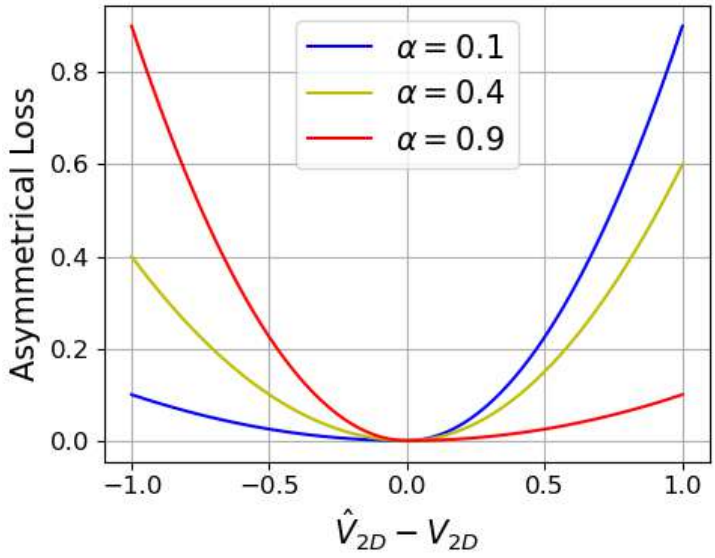

Figure 4. Asymmetrical Loss function. The asymmetrical loss function calculated for different values of the scale factor α.

3.3. Path Planning Algorithm

For controlling the mobile robot, we used the Zero Moment Point (ZMP) algorithm [20], which is described briefly in the following:

The Zero Moment Point can be described as the point $\vec{z}$ on the ground where the net moment along the vertical axis passing through $\vec{z}$ is zero:

$$\sum_i (\vec{r}_i - \vec{z}) \times \vec{f}_i = 0 \tag{10}$$

where $\vec{r}_i$ is the position of the i-th foot contact point relative to $\vec{z}$ and $\vec{f}_i$ is the ground reaction force at the i-th foot contact point

Assuming the center of mass does not move, the ZMP can be approximated as follows:

$$\vec{z} = \vec{p} - \frac{1}{mg} \sum_i \vec{f}_i \times \vec{r}_i \tag{11}$$

where m is the mass of the robot, g is the gravitational acceleration, and $\vec{p}$ is the position of the robot's center of mass.

The desired target ZMP $\vec{z}_d$ is calculated based on the desired motion (e.g., walking forward):

$$\vec{z}_d = f(\vec{p}_d, \vec{f}_1, \ldots, \vec{f}_n) \tag{12}$$

where f is a function that maps the desired motion to the target ZMP. The robot motion is then adjusted to bring the actual ZMP close to the target ZMP. The desired ZMP $\vec{z}_d$ was chosen based on the output of the Dynamic Window Approach algorithm, by selecting the destination point from the optimal generated trajectory. Our DWA implementation is based on a simplified non-holonomic robot model commonly encoutered in wheeled locomotion:

$$\begin{cases} x_{t+1} = x_t + v_{t+1} \cos \Theta \\ y_{t+1} = y_t + v_{t+1} \sin \Theta \\ \Theta_{t+1} = \Theta_t + \delta_{t+1} \end{cases} \tag{13}$$

where x and y represent the robot's position in the 2D birds-eye view moving space, Θ is the heading, and δ the desired direction.

DWA first calculates a dynamic window w for the commands of the robot, based on physical constraints regarding velocity and acceleration. Each command v_{t+1}, δ_{t+1} from the generated dynamic window is used to produce a candidate trajectory. Afterwards, predictions coming from the scene dynamics encoder network are used, together with current sensor observations to reject candidate trajectories that intersect any obstacle (predicted or observed). Each candidate trajectory that was not rejected in the previous step is then analyzed with respect to several performance indicators, and the following penalties are computed (see Algorithm 2):

- Goal cost (ϵ_G), which represents the distance between the Cartesian coordinates of the final state on the candidate trajectory and the coordinates of the goal point located on the global reference trajectory.
- Orientation cost (ϵ_ϕ), which represents the difference between the orientation angle from the final state of the candidate trajectory and the orientation angle from the reference orientation angle.
- Velocity cost (ϵ_v), which represents the difference between the mobile robot's velocity and the reference velocity.
- Smoothness cost (ϵ_s), which represents the difference between the previous command and the current command (if there is a significant difference between successive commands, then the motion of the mobile robot will become course).
- Trajectory cost (ϵ_t), which represents the sum of distances between Cartesian coordinates of the candidate trajectory and the reference trajectory.

Algorithm 2 DWA control loop

Require: $\mathbf{Z}_{ref}^{<t-\infty,t+\infty>}$ ▷ Global trajectory
Require: $\hat{\mathbf{V}}_{2D}^{<t+1,t+n>}$ ▷ Predicted observations
Require: $V_{2D}^{<t>}$ ▷ Current observation
Require: $s^{<t>}$ ▷ Current robot state
Require: $ZMP \leftarrow []$
$w \leftarrow$ dwa_window() ▷ Calculate dynamic window
$min_C = \infty$
for $v, \delta \in w$ **do**
    candidate $\leftarrow$ dwa_loop(v, δ)
    candidate $\leftarrow$ reject_collision(candidate, $s^{<t>}$, $\hat{\mathbf{V}}_{2D}$)
    if candidate $\neq \emptyset$ **then**
        $\epsilon_G \leftarrow$ goal_cost($v, \delta, \mathbf{Z}_{ref}$)
        $\epsilon_\phi \leftarrow$ orientation_cost($v, \delta, \mathbf{Z}_{ref}$)
        $\epsilon_v \leftarrow$ velocity_cost($v, \delta, \mathbf{Z}_{ref}$)
        $\epsilon_s \leftarrow$ smoothness_cost($v, \delta, v^{<t-1>}$,
        $\delta^{<t-1>}$)
        $\epsilon_t \leftarrow$ trajectory_cost($v, \delta, \mathbf{Z}_{ref}$)
        $C = K_G\epsilon_G + K_\phi\epsilon_\phi + K_v\epsilon_v + K_s\epsilon_s + K_t\epsilon_t$
        if $C < min_C$ **then**
            $min_C \leftarrow C$
            $ZMP \leftarrow candidate[n]$
        end if
    end if
end for

The collision rejection method parses all the centroids returned by the scene dynamics encoder module and rejects all candidate trajectories which intersect obstacles, either seen in the current timestamp observations or predicted by the neural network. After evaluating the total cost C for each of the candidate trajectories, the one with the minimum cost is selected and the ZMP gets updated.

4. Experiments

For evaluating our algorithm, we used sequences of data recorded during the navigation process of our mobile robot in the unstructured environment, more specifically, a forest road navigation task. The mobile robot shown in Figure 1a navigated within the environment, while potential collision situations were generated. In the meantime, depth sensor data were captured and analyzed during navigation. A global reference trajectory $\mathbf{Z}_{ref}^{<t-\infty,t+\infty>}$ was recorded for the mobile robot.

Samples of the data processed by the algorithm can be viewed in Figure 5. Depth images—Figure 5b—are used coupled with the camera parameters in order to obtain a 3D representation of the scene—Figure 5c. Then, 3D points are processed according to Section 3.2 and the three-dimensional voxel grid is computed—Figure 5d. This voxel grid is afterwards projected in a top-down view—Figure 5e. RGB and depth images were collected while the legged robot navigated on forest roads and interacted with humans, who acted as obstacles for our algorithm. In Figure 5a, a multiple-obstacle scenario is presented; the two persons are approaching the legged robot while it records RGB and depth images. The thresholding performed on the reconstructed three-dimensional points can be observed in Figure 5c. Ground points, as well as points that are too high or too far away from the robot, are eliminated from the resulting point cloud before the 3D voxel grid is computed.

Figure 5. Experimental data processing chain. The experimental data used by the algorithm. From top to bottom: (**a**)—RGB data, (**b**)—depth image, (**c**)—3D representation, (**d**)—3D voxel grid, and (**e**)—2D voxel grid.

The experiments were structured as follows:

- Training and testing data were acquired from the navigation scenario.
- The scene dynamics encoder network was trained using the preprocessed training data.
- The path planning algorithm was evaluated on the preprocessed test data.

We defined a safe distance $s = 0.5$ m for our mobile robot. Each violation of this distance, which meant that the mobile robot approached any obstacle within a radius less than s, automatically triggered a *collision event*. Collision events were counted, producing the first quality measure: n_{col}.

The second evaluation metric was the cross-track error, defined as the difference between the reference trajectory Z_{ref} and the generated local trajectory:

$$\bar{e}_{ct} = \frac{1}{n}\sum_{i=0}^{n} |f(x) - y_i| \tag{14}$$

where $f(x)$ is the polynomial approximation of the generated local trajectory evaluated in x and y_i is the measured point y coordinate.

The third evaluation metric was the orientation error:

$$\bar{e}_{\phi} = \frac{1}{n}\sum_{i=0}^{n} |\phi^{<i>} - \phi_d^{<i>}| \tag{15}$$

where $\phi^{<i>}$ is the robot's orientation at time step i and $\phi_d^{<i>}$ is the desired orientation from the global reference trajectory.

In order to reproduce potentially hazardous situations for the mobile robot, we experimented with people interacting with it during navigation. Interactions consisted of people approaching the robot from different angles and with varying velocity, in order to simulate dynamic obstacles.

We simulated four scenarios: front collision, side left, side right, and multiple obstacles. For the first scenario, a single person approached the mobile robot head on, while for the side collision left and side collision right scenarios, the human would approach the robot from the left and from the right sides, respectively. For the multiple obstacles setup, we considered two persons for our experiments.

We compared our approach to the classic Dynamic Window Approach path planner, configured with the same dynamic window generation parameters, as described in the Section 3.

Additionally, we strictly compared our scene dynamics encoder network with a state-of-the-art object detection algorithm, YoloV7 trained on the MS COCO dataset, as in the original implementation from [21], in terms of accuracy, false positive rate—FP_R and time to collision—ttc on our test data. The MS COCO dataset contains annotations for object detection (bounding boxes), semantic and instance segmentation, etc. [22] The time to collision is the estimated time elapsed between the first available detection of an obstacle until the respective obstacle crosses the safe distance threshold.

The results of the comparison between path planning algorithms are summarized in Table 1, while the results of the comparison between neural networks are presented in Table 2.

It can be observed that our proposal surpasses the baseline in all four test scenarios, both in the first experiment, as a path planning component, and in the second one, as a means of detecting dynamic obstacles present in the scene.

Table 1. Qualitative results on real-world mobile robot setup for path planning algorithm.

Scenario	Algorithm	n_{col}	$\bar{e}_{ct}(m)$	$\bar{e}_{\phi}(rad)$
Front	Ours	**7**	**0.35**	**0.12**
	DWA	27	0.43	0.15
Left	Ours	**5**	**0.37**	0.12
	DWA	33	0.43	0.12
Right	Ours	**3**	**0.29**	**0.1**
	DWA	32	0.39	0.11
Multiple	Ours	**5**	0.32	0.16
	DWA	37	0.32	**0.12**

Table 2. Qualitative results on real-world mobile robot setup for deep learning architectures.

Scenario	Algorithm	$t\bar{t}c(s)$	$FP_R(\%)$	$A(\%)$
Front	Ours	**2.5**	**10**	**95**
	YoloV7	2.3	12	92
Left	Ours	**1.2**	**10**	**93**
	YoloV7	1.3	11	92
Right	Ours	**1.3**	11	92
	YoloV7	1.0	11	92
Multiple	Ours	**1.7**	14	**88**
	YoloV7	1.3	**13**	82

The number of collisions n_c was significantly lower in all four testing scenarios in our approach than in the case of classical DWA. This suggests that including predicted observations in the trajectory generation step improves the obstacle avoidance capability of the system. The cross-track error $\bar{e}_{ct}$ and orientation error $\bar{e}_{\phi}$, respectively, were predominantly lower using our proposed algorithm than in the case of classical DWA. This is caused by the experimental tuning of the parameters included in our version of DWA (trajectory cost ϵ_t and orientation cost ϵ_{ϕ}).

The time to collision (ttc), false positive rate (FP_R), and accuracy (A) values were better in our approach than the YoloV7 variant because, in our proposal, the algorithm had more data to decide upon, due to the inclusion of predictions for future voxel grids. Additionally, using depth information instead of image data benefits the algorithm due to the fact that there is no need to perform error-prone object recognition.

Ablation Study

For the purpose of assessing the performance of the components from our algorithm, we performed three ablation studies.

In the first one, we compared three loss functions for our neural network: Mean Squared Error, Mean Absolute Error, and Asymmetrical Loss, respectively. It can be observed that the Asymmetrical Loss function converges the fastest out of the three functions, while the loss value is the lowest. We compared the three functions over 500 epochs for data in the validation set. The results can be viewed in Figure 6.

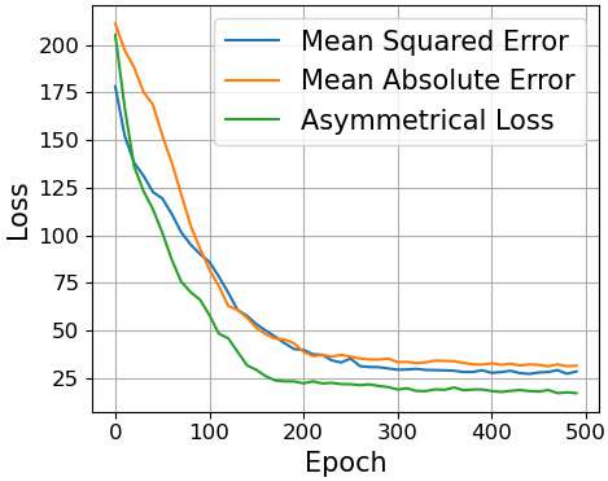

Figure 6. Loss functions ablation. Ablation of Mean Squared Error, Mean Absolute Error and Asymmetrical Loss functions. The Asymmetrical Loss function produces the lowest loss and converges the fastest out of the three functions.

The second study concerns the ablation of the prediction horizon size versus the time to collision estimate (*ttc*) and false positive rate FP_R. It is obvious that, by increasing the prediction horizon size, the *ttc* values improve slightly; however, this also produces a higher FP_R. Our experiments suggest that the increase of the prediction horizon size generates more noise in the predicted observations, which implicitly causes the algorithm to signal more collisions. The results of the prediction horizon size ablation are shown in Figure 7.

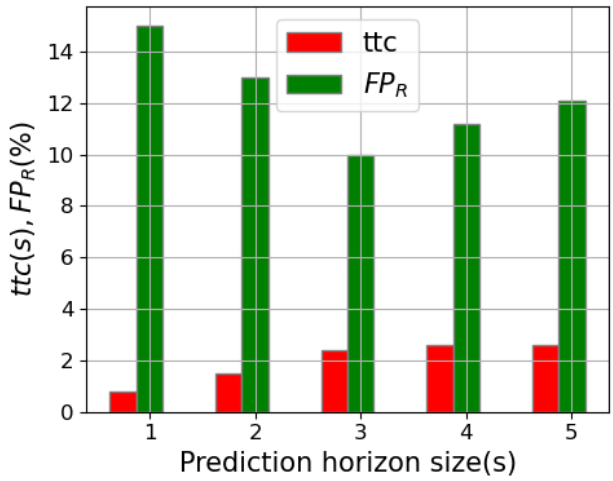

Figure 7. Prediction horizon size ablation. Prediction horizon size vs. performance metrics: *ttc* and FP_R. A slight improvement of the time to collision metric is observed when the algorithm predicts observations for a longer prediction horizon.

For the third ablation study, we compared the performance of the algorithm for different values of the history size parameter. For the comparison, we used the following values (in seconds): $[1, 3, 5, 7, 10]$. It can be observed that increasing the history size to a value larger than 5 s does not bring significant improvements to our algorithm. There is a slight improvement in the test result; however, the disadvantages outweigh the benefits. The results of the history size ablation are presented in Figure 8.

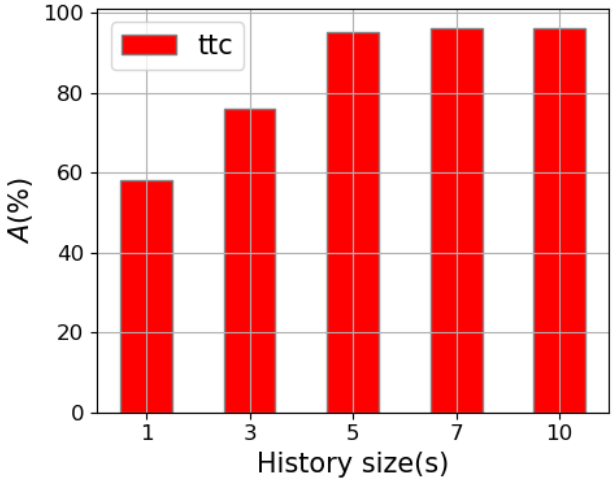

Figure 8. History size ablation. History size vs. accuracy performance metric. A slight improvement can be seen when presenting a longer sequence of historical data.

5. Conclusions

In this paper, we have introduced a vision dynamics learning approach for mobile robot navigation in unstructured environments. Our model is based on a recurrent neural

network that processes historical data coming from a depth sensor and produces predictions for future time steps over a fixed prediction horizon. We also described the process of converting the depth image into a three-dimensional point cloud, and then voxelizing the point cloud to a bidimensional grid of voxels that can serve as input for our deep learning model.

We have evaluated our model on real-world data, which was gathered during the mobile robot's navigation on a forest road. The ability to directly encode scene dynamics using a deep learning model has significant implications for robotics, as it can enable a more accurate understanding of the surroundings and more precise interactions between the robot and its environment, thus contributing to better decision making in tasks such as autonomous navigation.

Future work can explore using more complex neural network architectures, as well as integrating additional sensor inputs to the deep learning model, such as images or LiDAR data, in order to further improve the accuracy and robustness of the model.

Author Contributions: Conceptualization, L.F. and S.G.; methodology, C.G. and M.Z.; software, C.G.; validation, M.Z., L.F., D.C. and S.G.; formal analysis, C.G., D.C. and S.G.; investigation, C.G. and M.Z.; resources, L.F.; writing—original draft, C.G.; writing—review and editing, M.Z. and D.C.; supervision, S.G. All authors have read and agreed to the published version of the manuscript.

Funding: This work was supported by the Romanian Executive Agency for Higher Education, Research, Development, and Innovation Funding under Grant no. PED675/2022.

Data Availability Statement: Data are contained within the article.

Conflicts of Interest: The authors declare no conflicts of interest.

References

1. Bojarski, M.; Testa, D.D.; Dworakowski, D.; Firner, B.; Flepp, B.; Goyal, P.; Jackel, L.D.; Monfort, M.; Muller, U.; Zhang, J.; et al. End to End Learning for Self-Driving Cars. *arXiv* **2016**, arXiv:1604.07316.
2. Jaritz, M.; de Charette, R.; Toromanoff, M.; Perot, E.; Nashashibi, F. End-to-End Race Driving with Deep Reinforcement Learning. In Proceedings of the 2018 IEEE International Conference on Robotics and Automation (ICRA), Brisbane, Australia, 21–25 May 2018; pp. 2070–2075. [CrossRef]
3. Truong, J.; Yarats, D.; Li, T.; Meier, F.; Chernova, S.; Batra, D.; Rai, A. Learning Navigation Skills for Legged Robots with Learned Robot Embeddings. In Proceedings of the 2021 IEEE/RSJ International Conference on Intelligent Robots and Systems (IROS), Prague, Czech Republic, 27 September–1 October 2021; pp. 484–491. [CrossRef]
4. Seo, J.; Mun, J.; Kim, T. Safe Navigation in Unstructured Environments by Minimizing Uncertainty in Control and Perception. *arXiv* **2023**, arXiv:2306.14601.
5. Li, G.; Ji, Z.; Qu, X.; Zhou, R.; Cao, D. Cross-Domain Object Detection for Autonomous Driving: A Stepwise Domain Adaptative YOLO Approach. *IEEE Trans. Intell. Veh.* **2022**, *7*, 603–615. [CrossRef]
6. Wang, X.; Liu, J.; Qiu, T.; Mu, C.; Chen, C.; Zhou, P. A Real-Time Collision Prediction Mechanism With Deep Learning for Intelligent Transportation System. *IEEE Trans. Veh. Technol.* **2020**, *69*, 9497–9508. [CrossRef]
7. Pramanik, A.; Pal, S.K.; Maiti, J.; Mitra, P. Granulated RCNN and Multi-Class Deep SORT for Multi-Object Detection and Tracking. *IEEE Trans. Emerg. Top. Comput. Intell.* **2022**, *6*, 171–181. [CrossRef]
8. Rezaei, N.; Darabi, S. Mobile robot monocular vision-based obstacle avoidance algorithm using a deep neural network. *Evol. Intell.* **2023**, *16*, 1999–2014. [CrossRef]
9. Shepel, I.; Adeshkin, V.; Belkin, I.; Yudin, D.A. Occupancy Grid Generation With Dynamic Obstacle Segmentation in Stereo Images. *IEEE Trans. Intell. Transp. Syst.* **2022**, *23*, 14779–14789. [CrossRef]
10. Ren, Y.; Cai, Y.; Zhu, F.; Liang, S.; Zhang, F. ROG-Map: An Efficient Robocentric Occupancy Grid Map for Large-scene and High-resolution LiDAR-based Motion Planning. *arXiv* **2023**, arXiv:2302.14819.
11. Mohajerin, N.; Rohani, M. Multi-Step Prediction of Occupancy Grid Maps With Recurrent Neural Networks. In Proceedings of the IEEE/CVF Conference on Computer Vision and Pattern Recognition, Long Beach, CA, USA, 15–20 June 2019; pp. 10592–10600. [CrossRef]
12. Li, Z.; Zeng, J.; Chen, S.; Sreenath, K. Autonomous navigation of underactuated bipedal robots in height-constrained environments. *Int. J. Robot. Res.* **2023**, *42*, 565–585. [CrossRef]
13. Gilroy, S.; Lau, D.; Yang, L.; Izaguirre, E.; Biermayer, K.; Xiao, A.; Sun, M.; Agrawal, A.; Zeng, J.; Li, Z.; et al. Autonomous Navigation for Quadrupedal Robots with Optimized Jumping through Constrained Obstacles. In Proceedings of the 2021 IEEE 17th International Conference on Automation Science and Engineering (CASE), Lyon, France, 23–27 August 2021; pp. 2132–2139. [CrossRef]

14. Fan, T.; Chen, Z.; Zhao, X.; Liang, J.; Shen, C.; Manocha, D.; Pan, J.; Zhang, W. Autonomous Social Distancing in Urban Environments using a Quadruped Robot. *IEEE Access* **2021**, *9*, 8392–8403.
15. Fan, T.; Cheng, X.; Pan, J.; Manocha, D.; Yang, R. CrowdMove: Autonomous Mapless Navigation in Crowded Scenarios. *arXiv* **2018**, arXiv:1807.07870.
16. Grigorescu, S.; Ginerica, C.; Zaha, M.; Macesanu, G.; Trasnea, B. LVD-NMPC: A learning-based vision dynamics approach to nonlinear model predictive control for autonomous vehicles. *Int. J. Adv. Robot. Syst.* **2021**, *18*, 17298814211019544. [CrossRef]
17. Trăsnea, B.; Ginerică, C.; Zaha, M.; Măceşanu, G.; Pozna, C.; Grigorescu, S. OctoPath: An OcTree-Based Self-Supervised Learning Approach to Local Trajectory Planning for Mobile Robots. *Sensors* **2021**, *21*, 3606. [CrossRef] [PubMed]
18. Ginerica, C.; Zaha, M.; Gogianu, F.; Busoniu, L.; Trasnea, B.; Grigorescu, S. ObserveNet Control: A Vision-Dynamics Learning Approach to Predictive Control in Autonomous Vehicles. *IEEE Robot. Autom. Lett.* **2021**, *6*, 6915–6922. [CrossRef]
19. Ester, M.; Kriegel, H.P.; Sander, J.; Xu, X. *A Density-Based Algorithm for Discovering Clusters in Large Spatial Databases with Noise*; In Proceedings of the Second International Conference on Knowledge Discovery and Data Mining, Portland, OR, USA, 2–4 August 1996; AAAI Press: Portland, OR, USA, 1996.
20. Akbas, T.; Eskimez, S.E.; Ozel, S.; Adak, O.K.; Fidan, K.C.; Erbatur, K. Zero Moment Point based pace reference generation for quadruped robots via preview control. In Proceedings of the 2012 12th IEEE International Workshop on Advanced Motion Control (AMC), Sarajevo, Bosnia and Herzegovina, 25–27 March 2012; pp. 1–7. [CrossRef]
21. Wang, C.Y.; Bochkovskiy, A.; Liao, H.Y.M. YOLOv7: Trainable bag-of-freebies sets new state-of-the-art for real-time object detectors. *arXiv* **2022**, arXiv:2207.02696.
22. Lin, T.Y.; Maire, M.; Belongie, S.; Bourdev, L.; Girshick, R.; Hays, J.; Perona, P.; Ramanan, D.; Zitnick, C.L.; Dollar, P. Microsoft COCO: Common Objects in Context. In *Computer Vision—ECCV*; Springer: Cham, Switzerland, 2014; Volume 8693, pp. 740–755. [CrossRef]

Disclaimer/Publisher's Note: The statements, opinions and data contained in all publications are solely those of the individual author(s) and contributor(s) and not of MDPI and/or the editor(s). MDPI and/or the editor(s) disclaim responsibility for any injury to people or property resulting from any ideas, methods, instructions or products referred to in the content.

Hindawi Publishing Corporation
International Journal of Photoenergy
Volume 2016, Article ID 9825683, 7 pages
http://dx.doi.org/10.1155/2016/9825683

Research Article

Accelerated Life Test for Photovoltaic Cells Using Concentrated Light

Daniel Tudor Cotfas, Petru Adrian Cotfas, Dan Ion Floroian, and Laura Floroian

Electrical Engineering and Computer Science Faculty, Transilvania University of Brasov, 500036 Brasov, Romania

Correspondence should be addressed to Daniel Tudor Cotfas; dtcotfas@unitbv.ro

Received 14 April 2016; Revised 7 June 2016; Accepted 3 July 2016

Academic Editor: Prakash Basnyat

Copyright © 2016 Daniel Tudor Cotfas et al. This is an open access article distributed under the Creative Commons Attribution License, which permits unrestricted use, distribution, and reproduction in any medium, provided the original work is properly cited.

This paper presents a new method developed to significantly reduce the necessary time for the ageing tests for different types of photovoltaic cells. Two ageing factors have been applied to the photovoltaic cells: the concentrated light and the temperature. The maximum power of the photovoltaic cells was monitored during the ageing process. The electrical dc and ac parameters of the photovoltaic cells were measured and analyzed at 1 sun irradiance, before and after the test stress. During the test, two photovoltaic cells are kept at maximum power point and the other two are kept at open circuit voltage point. The method is validated through the results obtained for the monocrystalline silicon solar cell.

1. Introduction

The reliability and durability are two important factors for the new photovoltaic cells and panels, today perhaps at least as important for them as the price per watt. The lifetime of new photovoltaic cells such as, but not only, the multijunction cells used in concentrated light whose efficiency is 46% [1] and the very promising perovskite solar cells whose efficiency increases very quickly at 20.1% [2], is not known.

Therefore, a predictive model for the lifetime and the behavior of the new photovoltaic cells and panels is very important for producers as well as for customers. The accelerated ageing test for the photovoltaic cells and panels is one of the main analyses which are the base of the predictive model [3, 4].

There are several methods to realize the accelerated ageing test for photovoltaic cells and panels indoors, such as

(i) Damp Heat Test (DH): the ageing factors are the temperature and the relative humidity; the values for these two factors are 85°C and 85%; the time for the ageing test is over 2000 hours [5];

(ii) Highly Accelerated Stress Test (HAST): the ageing factors are the temperature and the relative humidity, but their values grow in comparison to DH, so the temperature can be 110°C, 130°C, or 150°C, and the humidity can be 85% or 100%; the increasing of the ageing factors values leads to the decrease of the time for the ageing test; in this case the time for the ageing test is around 400 hours;

(iii) step-stress accelerated ageing tests: the ageing factors are the temperature and the injected current to emulate constant illumination; the temperature can be 130°C, 150°C, or 170°C and the value of the current is equal to the value of the short circuit current, I_{sc}, at 1 sun multiplied with 700 or 1050; the test being made for multijunction solar cells [6];

(iv) thermal cycling test: this method uses the variation of the temperature between −40°C and 85°C and the injected current to emulate constant illumination; the amount of the cycling varies in function of the upper limit of the temperature, 500 for 110°C, 1000 for 85°C, or 2000 for 65°C; the injected current in the solar cell is equal to $1.25 \times I_{sc} \times$ no. of suns [7];

(v) potential induced degradation (PID): the ageing factors for the photovoltaic modules are the external bias voltage, the temperature, and the relative humidity; their values are 1000 V, 50°C, and 50% [5] or 600 V, 65°C, and 85% [8].

The lifetime for the Si photovoltaic panels now is known and it is over 25 years [9]. The failure criterion is when its maximum power decreases with at least 20% from the initial maximum power [10].

Núnez et al. had defined a degradation failure criterion for the multijunction cells [11]. The failure limit is when the maximum power decreases with at least 2.5% from the initial maximum power. Núnez et al. considered that a power loss of up to 20% is generated by the other elements of the concentrator photovoltaic system.

The degradation failure criterion for the silicon photovoltaic cell corresponds to losing 10% of the maximum power through light-induced power degradation, occurrence of microcracks, increase in series resistance, decrease of shunt resistance, and so forth [12–14].

2. Method

The main goal of the accelerated life test is to reduce the testing time under simulated working conditions. In DH test the necessary time is around 2000 h and the target of the new methods is tens or some hundreds of hours.

There are many methods to perform the accelerated life test, but there is scarce research using light as ageing factor, because the majority use a climatic chamber and therefore the concentrated light is difficult to use [11]. The researchers had emulated the work conditions in concentrated light by injection of the forward current equivalent to the photogenerated current by the photovoltaic cell at the level of the desired concentration [11, 15]. In this case the stress produced on the photovoltaic cells by the high concentrated light cannot be taken into consideration.

The paper presents a new method for the accelerated life test using the concentrated light obtained from a solar simulator with a xenon lamp (called ALTCL). Due to working conditions there are two stress factors: light and temperature.

The experiment set-up to apply the new method consists of the solar simulator, the photovoltaic cells, the measurement system, and the photovoltaic cells support cooled with water, which is provided with a variable flow of water [16].

2.1. Solar Simulator. The experiments were performed at Solar Technology Laboratory of Paul Scherrer Institute (PSI), Villigen, Switzerland, using the high-flux solar simulator (HFSS), which has ten xenon arc lamps cooled with high pressure water, Figure 1. The highly concentrated light, similar to the solar radiation, is obtained in the focal plane using the lamps.

The lamp reflector is designed as a truncated ellipsoid [17, 18]. The accelerated ageing test was performed using only one of the ten xenon arc lamps, which works at 10.6 kW. The electric power of the lamp was maintained quasi-constant using an automatic system.

2.2. Photovoltaic Cells' Water Cooled Support. The photovoltaic cells' water cooling support allows the mounting of the four PV cells in different configurations and the maintaining of the PV cells temperature quasi-constant during the measurements under concentrated light [16]; see Figure 2.

The facility of the various mounting of the photovoltaic cells is necessary to have the PV cells illuminated with the same or with the different levels of the concentrated light.

The temperature of the photovoltaic cells can be adjusted using the levels of illumination and also the variable water flow which can be assured by the automatic pump system. The distribution of the illumination levels obtained with one xenon lamp at PSI is presented in Figure 3.

The photovoltaic cells were positioned so all of them are uniformly illuminated, with the same radiative flux, 190 suns. The shutter of the solar simulator was gradually opened until the temperature of the photovoltaic cells was $150^{\circ}C \pm 2^{\circ}C$.

2.3. Measurement System. The measurements were performed in concentrated light and under illumination at 1 sun.

The measurements in concentrated light were performed at PSI using a system based on cRIO from National Instruments and a module developed by our team which allows measuring the current voltage characteristics, *I-V*, for all four photovoltaic cells simultaneously and also their temperature. The photovoltaic cells' temperature was measured using a thermocouple for each of them. The maximum power can be determined by measuring *I-V* characteristic of the photovoltaic cells. For measuring the current and voltage on the photovoltaic cells the NI 9227 and NI 9215 modules were used. The first module is used to measure the current through the photovoltaic cells and the second one is used for measuring their output voltage. These modules allow measuring all four channels at the same time. The dynamic load used for measuring *I-V* characteristics of the photovoltaic cell is based on a large capacitor. The solar cell temperatures are measured with a NI 9211 module which allows sampling simultaneously for all four channels. The DIO (Digital Input Output) NI 9401 module is used for starting *I-V* characteristic measurements. Between measurements of two consecutive *I-V* characteristics a load can be applied to the photovoltaic cells. The applied load is based on a MOSFET which is controlled using the four analog outputs of the NI 9269 module. Some of the studied photovoltaic cells were maintained in the maximum power point regime while the others were maintained in the open circuit regime.

The measurements under 1-sun illumination were performed using the Autolab PGSTAT100. This system allows measuring *I-V* characteristic under illumination using the potentiostat mode and also plotting and fitting the Nyquist diagram using the Fra (Frequency Response Analyzer) module.

2.4. Photovoltaic Cells. The photovoltaic cells chosen for the experiment are commercial monocrystalline silicon cells and InGaP/InGaAs/Ge multijunction cells. Four photovoltaic cells were tested, two of each type. In each pair of photovoltaic cells one of them was measured with load and one without load.

The reason of the choosing the monocrystalline silicon cells is that the lifetime is known. The monocrystalline silicon

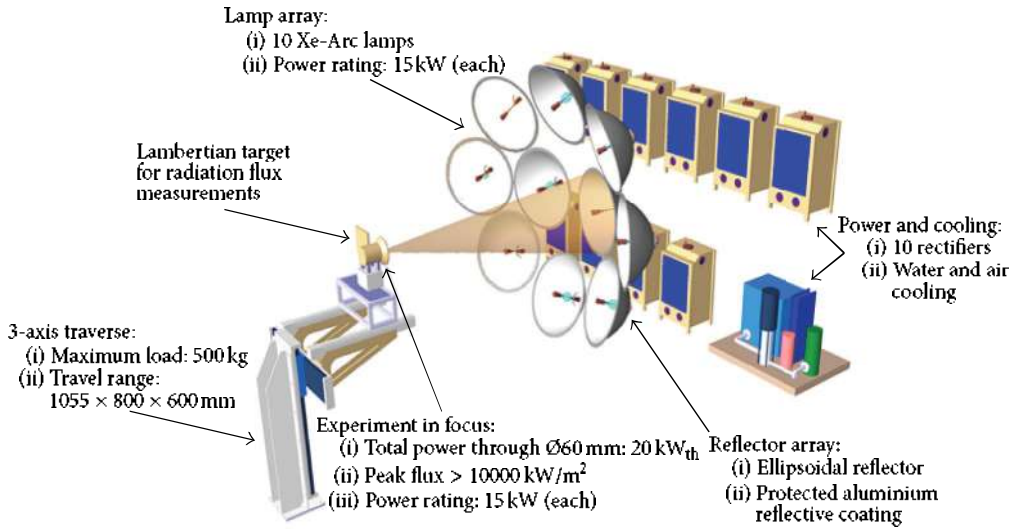

FIGURE 1: Schema of the solar simulator.

FIGURE 2: The photovoltaic cells' water cooled support with four PV cells.

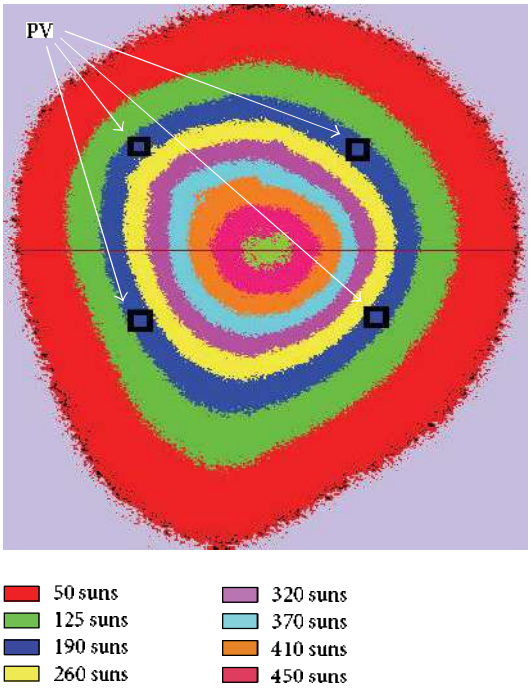

FIGURE 3: The radiative flux map and the positioning of the photovoltaic cells.

photovoltaic cells were cut at 0.5 cm/0.5 cm because the system can measure up to 5 A and for a good uniformity of the illumination. The short circuit current measured at 190 suns is 1.65 A and the open circuit voltage is 0.668 V.

InGaP/InGaAs/Ge photovoltaic cells are made to work in concentrated light. Their structure is triple junction and the dimensions are 1 cm/1 cm. The short circuit current measured at 190 suns is 2.67 A and the open circuit voltage is 2.82 V.

3. Results and Discussion

The desired temperature for the test, 150°C, was obtained and maintained quasi-constant using only the concentrated light and the cooling system.

Núnez et al. [11] proposed two criteria for reliability of the photovoltaic cell: catastrophic failure, instant drop in power of the photovoltaic cells, and degradation failure, the power decreasing with more than 2.5% for the multijunction photovoltaic cells which work in concentrated light and more than 10% for the silicon photovoltaic cells.

The photovoltaic cells were subjected to 190-sun concentrated light and 150°C for 35 hours and 7 hours per day and in the rest of day they were kept in darkness and at room temperature. After five days only the second criterion was observed.

The result of the accelerated ageing test of the monocrystalline silicon photovoltaic cell without load during the experiment is presented in Figure 4. The normalized power

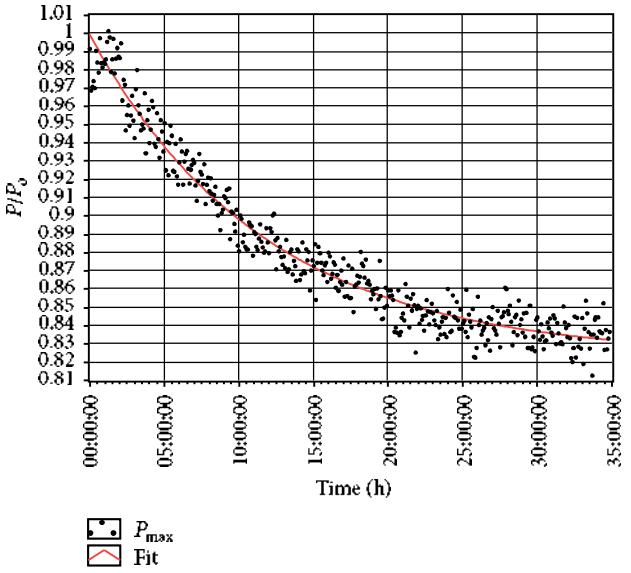

FIGURE 4: The normalized power of the monocrystalline photovoltaic cell without load evolution over time.

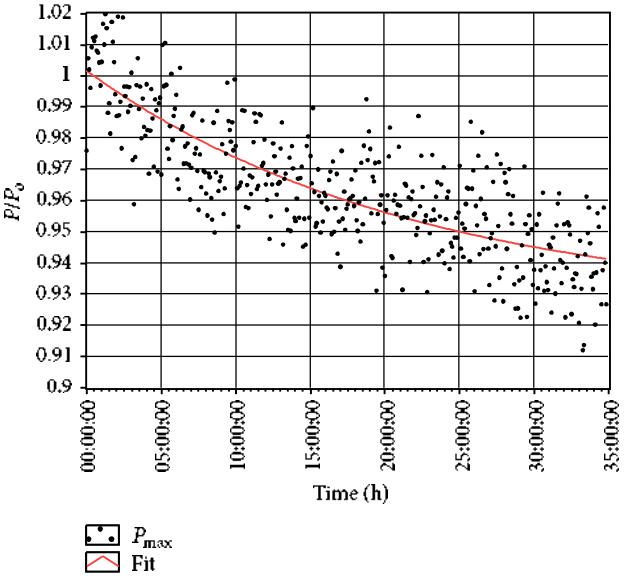

FIGURE 5: The normalized power of the monocrystalline photovoltaic cell with load evolution over time.

P/P_o, which is the ratio between the maximum power P determined during the experiment and the initial maximum power P_o of the photovoltaic cell at 190 suns and 150°C, is represented over the time. The maximum power of the photovoltaic cell was determined using *I-V* characteristic which was measured every five minutes.

The normalized power of the monocrystalline silicon photovoltaic cell without load decreases exponentially; see the red fitting curve from Figure 4, and the degradation failure criterion is reached after 10 hours. After 20 hours, an asymptotic decrease is observed in the normalized power. The normalized power after 35 hours is 0.83, which means a decrease of 17%; see Figure 4.

The normalized power InGaP/InGaAs/Ge multijunction photovoltaic cell without load decreases very slowly and after 35 hours it decreases only by 1.5%.

The decreasing ratio of the normalized power for the photovoltaic cells with load during the ageing test, after 35 hours, was lower, 6% for the monocrystalline silicon (see Figure 5), and negligible for the multijunction photovoltaic cell.

The photovoltaic cells were analyzed in static regime, dc, and dynamic regime, ac, before and after the accelerated ageing test.

I-V characteristics and power voltage, *P-V*, characteristics are measured for each photovoltaic cell. The measurements were realized with Autolab, under illumination at 1000 W/m^2 irradiance (1 sun) and at this time the temperature of the photovoltaic cells is maintained constant with thermostat at 25°C ± 0.5°C.

Figure 6 shows *I-V* and *P-V* characteristics measured for the monocrystalline silicon photovoltaic cell without load before and after the accelerated test. By analyzing the results it is observed that the short circuit current, I_{sc}, decreases with 3.9% ± 0.1%, the open circuit voltage decreases with 5.4 ± 0.1%, and the maximum power decreases with 18.2% ± 0.2%.

The shape of *I-V* characteristic around the knee (the maximum power point), for the aged photovoltaic cell, shows an important modification. This can be explained by the increasing of the series resistance, R_s, and the decreasing of the shunt resistance, R_{sh}.

I-V and *P-V* characteristics measured for the InGaP/InGaAs/Ge multijunction photovoltaic cell without load before and after the accelerated test are presented in Figure 7. The maximum power decreases with 1.5% ± 0.1%, whereas I_{sc} and V_{oc} remain quasi-constant after the ageing process. The shape of *I-V* characteristic measured after the ageing process remains almost unchanged, only the effect of the slight increase in the series resistance being observed.

The impedance spectroscopy [19, 20] with the frequency domain technique is used to analyze the parameters of the photovoltaic cells in dynamic regime before and after the ageing process. An ac pure sinusoidal signal with amplitude smaller than the thermal voltage, (kT/e), is superposed on the dc bias signal. The measurements were performed at bias voltage equal to V_{max}, the voltage corresponding to the maximum power point. The photovoltaic cells were maintained at 25°C ± 0.5°C and were illuminated at 1 sun.

The Nyquist diagrams, before and after the ageing process, for the monocrystalline silicon photovoltaic cell without load are presented in Figure 8 and those for the InGaP/InGaAs/Ge multijunction photovoltaic cell without load are presented in Figure 9. The important ac parameters of the photovoltaic cells are obtained using the fitting procedure with the equivalent ac circuit and they are presented in Table 1.

The results obtained for the ac parameters of the photovoltaic cells confirm analysis for the behavior of the photovoltaic cells in static regime. The series resistance strongly increases for the monocrystalline silicon photovoltaic cell,

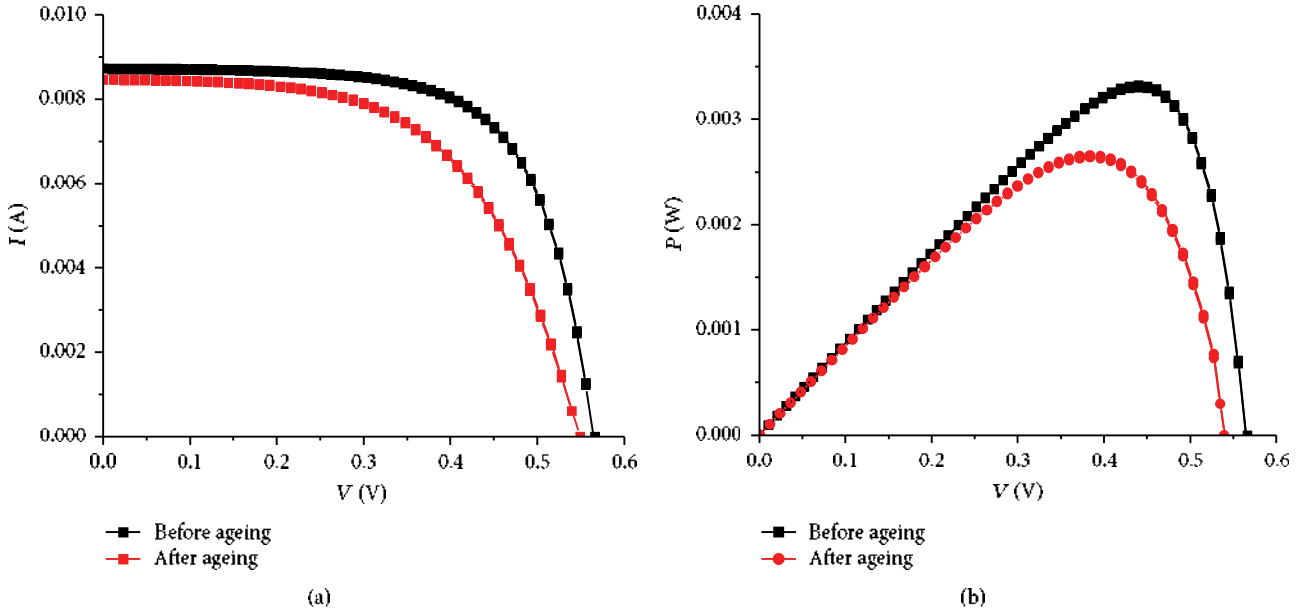

FIGURE 6: The monocrystalline silicon photovoltaic cell without load before and after ageing process. (a) *I-V* characteristics; (b) *P-V* characteristics.

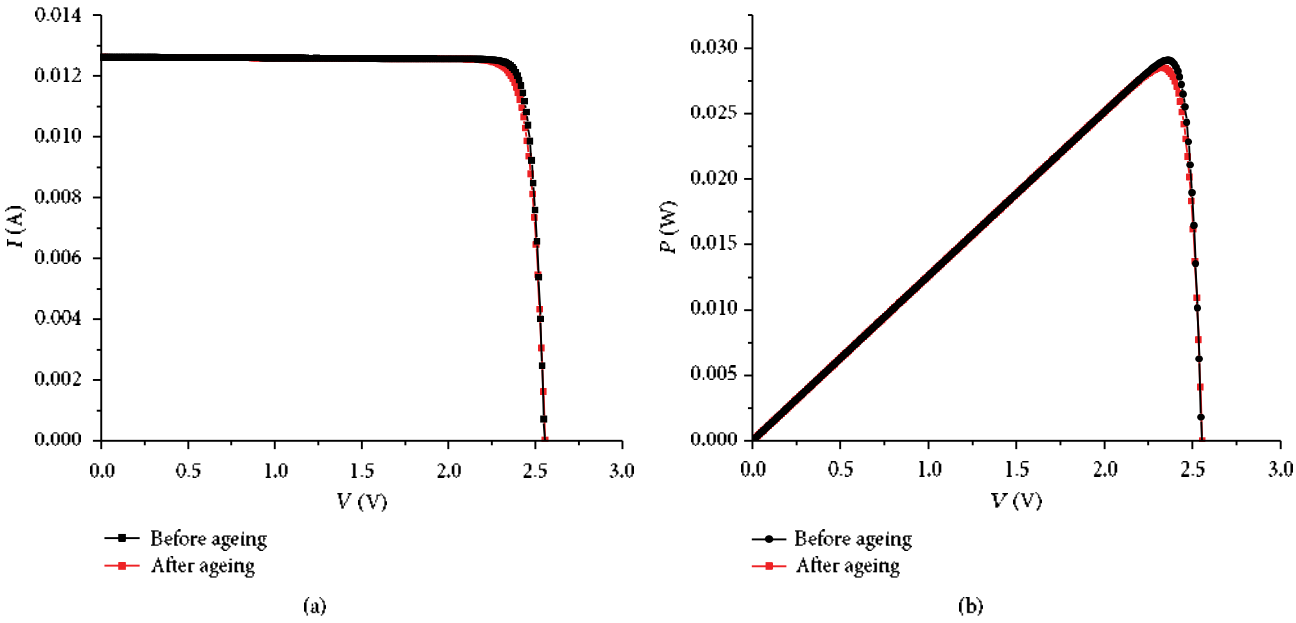

FIGURE 7: The InGaP/InGaAs/Ge multijunction photovoltaic cell without load before and after ageing process. (a) *I-V* characteristics; (b) *P-V* characteristics.

TABLE 1: The ac parameters of the photovoltaic cells at 1000 W/m^2 and 25°C.

Type of photovoltaic cell	Ageing test	R_s [Ω]	R_p [Ω]	C [nF]
Monocrystalline silicon without load	Before	0.23 ± 0.01	49.67 ± 0.2	644.3 ± 3.5
	After	0.76 ± 0.01	24,23 ± 0.16	432.4 ± 2.5
Monocrystalline silicon with load	Before	0.22 ± 0.01	49.71 ± 0.2	642.3 ± 3.5
	After	0.45 ± 0.01	38,23 ± 0.16	552.4 ± 2.5
InGaP/InGaAs/Ge without load	Before	0.87 ± 0.012	18.42 ± 0.12	(19.43 ± 0.1) * 10^3
	After	0.881 ± 0.012	18.39 ± 0.12	(19.42 ± 0.1) * 10^3

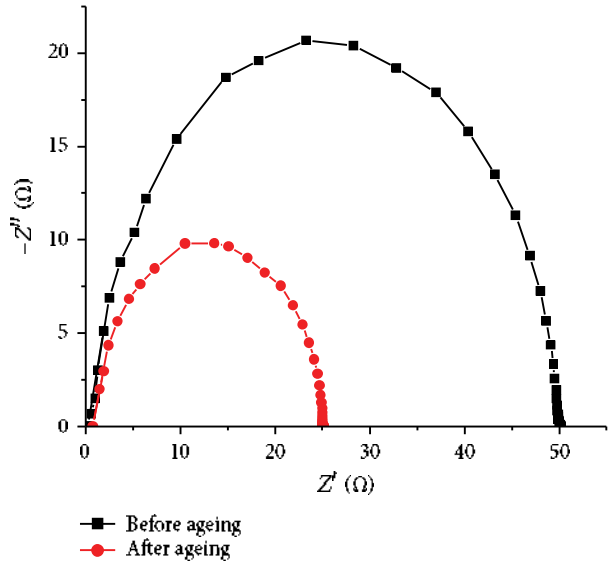

Figure 8: Nyquist plot of the monocrystalline silicon photovoltaic cell without load before and after ageing process.

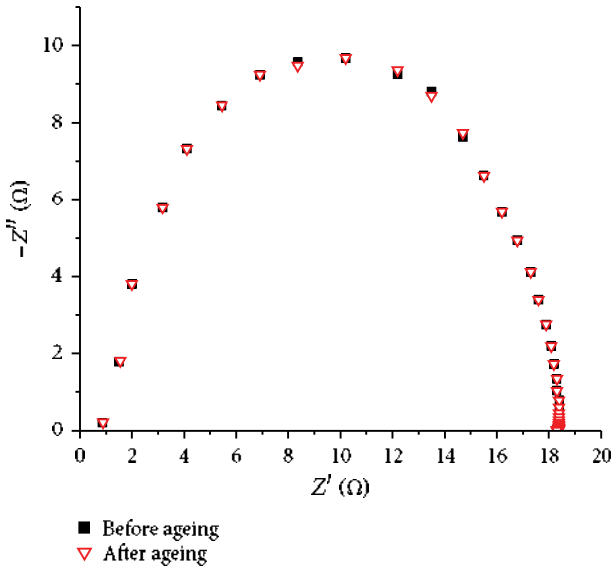

Figure 9: Nyquist plot of the InGaP/InGaAs/Ge multijunction photovoltaic cell without load before and after ageing process.

whereas for the multijunction photovoltaic cell it slightly increases. The same behavior is determined for the decrease of the shunt resistance and for the capacitance.

4. Conclusions

A new method for the accelerated life test of the photovoltaic cells was developed and verified. The novelty of the method is the use of only concentrated light and the cooling system so as to have two ageing factors: the light and the temperature.

The duration of the life test is reduced considerably, for example, 10–20 hours for the monocrystalline silicon photovoltaic cells without load at 190 suns. For monocrystalline silicon cell with load the degradation after 35 h at the same illumination is 6%. The maximum power of InGaP/InGaAs/Ge multijunction cell without load at 190 suns after 35 hours decreases with 1.5%, which means it does not reach the limit of the degradation failure.

The maximum power of the photovoltaic cells with load decreases slighter than the maximum power of the photovoltaic cells without load, which proves that lifetime of the photovoltaic panels increases if they work in load.

The parameters of the photovoltaic cells were analyzed in static and dynamic regime at 1 sun and 25°C using *I-V* and *P-V* characteristics and the Nyquist diagrams. The behavior of the short circuit current, open circuit voltage, maximum power, series and parallel resistance, and capacitance before and after the ageing process was studied.

The future research will consist of increasing the duration of the life test for the multijunction photovoltaic cells until the limit of the degradation failure criterion is reached and also we will apply the method validated by present work to test other type of photovoltaic cells.

Competing Interests

The authors declare that they have no competing interests.

Acknowledgments

Financial support by the Access to Research Infrastructures activity in the 7th Framework Programme of the EU (SFERA 2 Grant Agreement no. 312643) is gratefully acknowledged. The authors are thankful to Y. Baeuerle, D. Wuillemin, and C. Wieckert as well as further coworkers from the Solar Technology Laboratory of Paul Scherrer Institute, Villigen, Switzerland, where all the measurements in concentrated light were performed. They hereby acknowledge the structural funds project PRO-DD (POS-CCE, O.2.2.1., ID 123, SMIS 2637, no. 11/2009) for providing a part of the infrastructure used in this work.

References

[1] M. A. Green, K. Emery, Y. Hishikawa, W. Warta, and E. D. Dunlop, "Solar cell efficiency tables (version 44)," *Progress in Photovoltaics: Research and Applications*, vol. 23, pp. 1–9, 2015.

[2] M. I. Ahmed, A. Habib, and S. S. Javaid, "Perovskite solar cells: potentials, challenges, and opportunities," *International Journal of Photoenergy*, vol. 2015, Article ID 592308, 13 pages, 2015.

[3] US Department of Energy, Sandia, and NREL, "Accelerated aging testing and reliability in photovoltaics. Solar energy technology program," 2008.

[4] D. C. Jordan and S. R. Kurtz, "Photovoltaic degradation rates—an analytical review," *Progress in Photovoltaics: Research and Applications*, vol. 21, no. 1, pp. 12–29, 2013.

[5] A. Phinikarides, N. Kindyni, G. Makrides, and G. E. Georghiou, "Review of photovoltaic degradation rate methodologies," *Renewable and Sustainable Energy Reviews*, vol. 40, pp. 143–152, 2014.

[6] J. R. Gonzalez, M. Vázquez, N. Núnez, C. Algora, I. Rey-Stolle, and B. Galiana, "Reliability analysis of temperature step-stress tests on III–V high concentrator solar cells," *Microelectronics Reliability*, vol. 49, no. 7, pp. 673–680, 2009.

[7] G. J. Lin, L. J. Wang, J. Q. Liu, W. P. Xiong, M. H. Song, and Z. H. Wu, "Accelerated aging tests of high concentration multi-junction solar cells," *Procedia Environmental Sciences*, vol. 11, pp. 1147–1152, 2011.

[8] C. R. Osterwald, T. J. McMahon, and J. A. del Cueto, "Electrochemical corrosion of SnO_2:F transparent conducting layers in thin-film photovoltaic modules," *Solar Energy Materials and Solar Cells*, vol. 79, no. 1, pp. 21–33, 2003.

[9] E. Kaplani, "Detection of degradation effects in field-aged c-Si solar cells through IR thermography and digital image processing," *International Journal of Photoenergy*, vol. 2012, Article ID 396792, 11 pages, 2012.

[10] M. Vazquez and I. Rey-Stolle, "Photovoltaic module reliability model based on field degradation studies," *Progress in Photovoltaics: Research and Applications*, vol. 16, no. 5, pp. 419–433, 2008.

[11] N. Núnez, J. R. Gonzalez, M. Vazquez, C. Algora, and P. Espinet, "Evaluation of the reliability of high concentrator GaAs solar cells by means of temperature accelerated aging tests," *Progress in Photovoltaics: Research and Applications*, vol. 21, no. 5, pp. 1104–1113, 2013.

[12] M. Paggi, I. Berardone, A. Infuso, and M. Corrado, "Fatigue degradation and electric recovery in Silicon solar cells embedded in photovoltaic modules," *Scientific Reports*, vol. 4, article 4506, pp. 1–7, 2014.

[13] D. De Graaff, R. Lacerda, and Z. Campeau, "Degradation mechanisms in Si module technologies observed in the field; their analysis and statistics," in *Proceedings of the NREL Photovoltaic Module Reliability Workshop*, Golden, Colo, USA, February 2011.

[14] P. Basnyat, B. Sopori, S. Devayajanam et al., "Experimental study to separate surface and bulk contributions of light-induced degradation in crystalline silicon solar cells," *Emerging Materials Research*, vol. 4, no. 2, pp. 239–246, 2015.

[15] C. Algora, "Reliability of III–V concentrator solar cells," *Microelectronics Reliability*, vol. 50, no. 9–11, pp. 1193–1198, 2010.

[16] D. T. Cotfas, P. A. Cotfas, D. Floroian, L. Floroian, and M. Cernat, "Ageing of photovoltaic cells under concentrated light," in *Proceedings of the 2015 Intl Aegean Conference on Electrical Machines & Power Electronics (ACEMP '15) and Intl Conference on Optimization of Electrical & Electronic Equipment (OPTIM) & 2015 Intl Symposium on Advanced Electromechanical Motion Systems (ELECTROMOTION '15)*, Side, Turkey, September 2015.

[17] J. Petrasch, P. Coray, A. Meier et al., "A novel 50 kW 11,000 suns high-flux solar simulator based on an array of xenon arc lamps," *ASME Journal of Solar Energy Engineering*, vol. 129, no. 4, pp. 405–411, 2007.

[18] I. Alxneit and H. Schmit, "Spectral characterization of PSI's high-flux solar simulator," *Journal of Solar Energy Engineering*, vol. 134, no. 1, Article ID 011013, 2012.

[19] M. Toivola, J. Halme, L. Peltokorpi, and P. Lund, "Investigation of temperature and aging effects in nanostructured dye solar cells studied by electrochemical impedance spectroscopy," *International Journal of Photoenergy*, vol. 2009, Article ID 786429, 15 pages, 2009.

[20] D. T. Cotfas, P. A. Cotfas, and S. Kaplanis, "Methods and techniques to determine the dynamic parameters of solar cells: review," *Renewable and Sustainable Energy Reviews*, vol. 61, pp. 213–221, 2016.

Ageing of Photovoltaic Cells Under Concentrated Light

D.T. Cotfas[1], P.A Cotfas[1], D. Floroian[1], *Member IEEE*, L. Floroian[1], Mihai Cernat[1, 2], *Senior Member*, *IEEE*
[1]Faculty of Electrical Engineering and Computer Science, Transilvania University of Brasov, Romania
[2]Faculty of Engineering, Karabük University, Turkey
dtcotfas@unitbv.ro, pcotfas@unitbv.ro, dan.floroian@unitbv.ro, lauraf@unitbv.to, m.cernat@unitbv.ro

Abstract—**A novel Automated System for Cooling and Measurement under Concentrated Light (ASCMCL) and a new method to study the accelerated ageing of photovoltaic cells by using concentrated light are presented. The measurement system created is an autonomous one that can be used without surveillance. By using the new method proposed in this paper, the time of the ageing accelerated test is significantly reduced. The measurements performed at the Solar Technology Laboratory of Paul Scherrer Institute, Villigen, Switzerland confirm the utility of the proposed system and method.**

Keywords—photovoltaic cell; ageing; concentrated light; solar simulator

I. INTRODUCTION

Nowadays researchers and manufacturers develop many types of photovoltaic cells using different kinds of material for obtaining cells with high efficiency and/or small per-watt price, which are the most important requirements.

The life time for some of the photovoltaic cells can be relatively precise estimated, e.g. for the monocrystalline silicon, the most used, it is of 25 years. For new photovoltaic cells this important parameter is unknown or less studied, e.g. for multijunction photovoltaic cells, whose efficiency reaches 44% under concentrated sunlight [1, 2].

Photovoltaic cells parameters, such as the photo-generated, the short circuit, and the reverse saturation currents, the open circuit voltage, the maximum power, the series and the shunt resistances, the ideality factor of diode, the fill factor and the efficiency, are object of many studies [3]. However, the evolution of these parameters during the ageing process have been little studied so far.

There are also many studies dedicated to ageing of photovoltaic cells and panels depending of the temperature and humidity, but there are few studies of the ageing by using of concentrated light and high temperature.

The majority of the ageing tests used in the electronic industry, consider the temperature and the humidity as parameters [4]. The main disadvantage of this kind of testing consists in the long time required. Reduction of the test time is possible using accelerated ageing tests. There are several typical accelerated tests for studying the ageing of photovoltaic cells and panels, such as: Damp Heat test (DH), Highly Accelerated Stress Test (HAST) or Highly Accelerated Stress Test. Note that accelerated ageing tests are made in climatic chambers, where it is difficult to use a light source. The bias current is injected through the bus bar to simulate the state of photovoltaic cells, when they are exposed to concentrated light [5-7]. In the cases of the DH test and the HAST, the Arrhenius model (temperature) and the Peck model are used, the latter being a statistical thermodynamic model (which considers the influences of the temperature and the humidity) [4]. As a consequence in the aforementioned accelerated ageing tests, the degradation induced by the light is not taken into account and the measurement current-voltage characteristic of the photovoltaic cells is made in dark conditions [8].

This paper proposes a new system for the accelerated ageing test of photovoltaic cells using concentrated light.

II. THE ASCMCL SYSTEM

The experimental set-up for the accelerated ageing test in concentrated light consists of: a high flux solar simulator, the ASCMCL system and different types of photovoltaic cells.

A. The high flux solar simulator

Measurements are performed by our team at Solar Technology Laboratory, Paul Scherrer Institute (PSI), Villigen, Switzerland, using the high flux solar simulator.

As it can be seen in Fig. 1a, the high flux solar simulator (HFSS) uses an array on ten water-cooled high pressure xenon arc lamps (Ushio UXW, 15 kW) [9]. The HFSS has been designed and built to obtain in the focal plane highly concentrated light, similar to the solar radiation [9]. High-power xenon arc lamps are mostly used as radiation sources [10]. Their radiation is concentrated by specifically designed optic reflector. The arc lamps usually radiate mainly in visible domains of the spectrum, but there are also some components in the ultraviolet and in the infrared domains. For obtaining a spectral distribution closely to those of the AM1.5 solar spectrum (air mass) standard, optical filters are used [11].

Each of the 10 lamps has its own reflector, which is designed as a truncated ellipsoid, Fig.1 b. The optimized ellipsoid geometry was determined by Monte Carlo ray-tracing simulations [10]: truncation diameter of 0.95 m, ellipsoid semi-axes of 1.685 m and 0.768 m, numerical eccentricity of 0.89.

a)

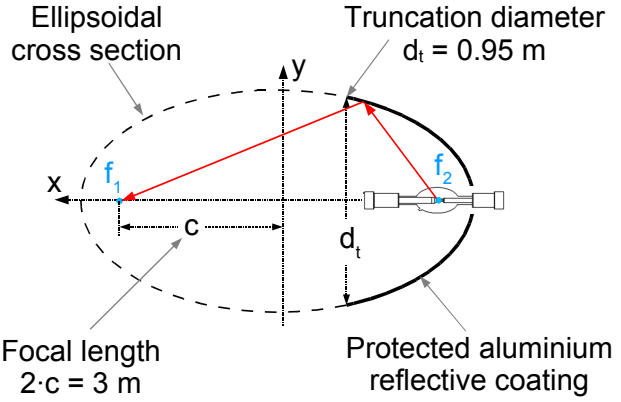

b)

Fig. 1. PSI's high flux solar simulator

The optimized reflector exhibits a focal length (distance between the two foci of the ellipsoid) of 3.0 m. The design of the lamp is made so that the brightest part of the arc coincides with the primary focus of the reflector [12]. The reflectors are mounted so that all second foci coincide.

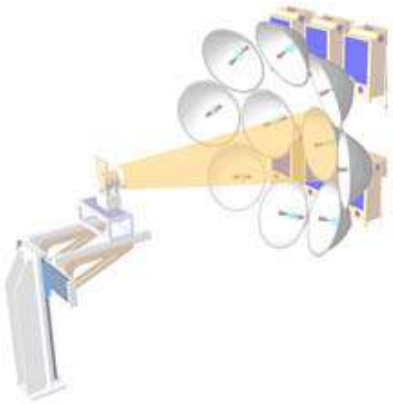

Fig. 2. The schemata of the PSI's HFSS when using one lamp [12]

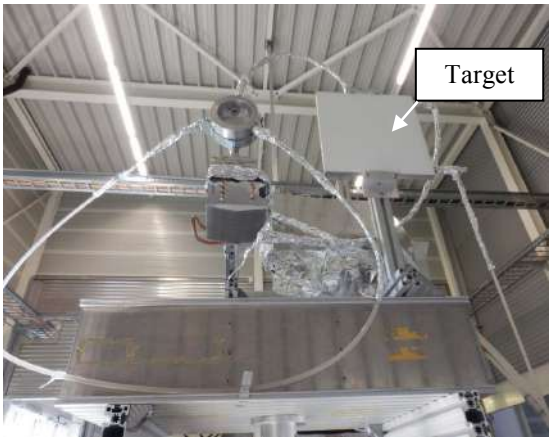

a)

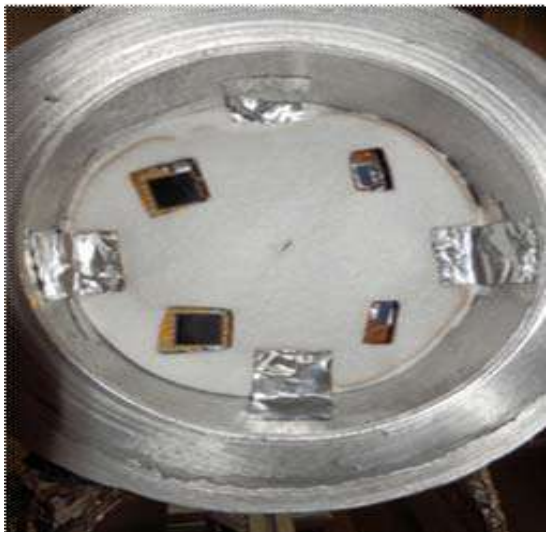

b)

Fig. 3. The cooling system

The accelerated ageing tests under concentrated light were performed using four photovoltaic cells, illuminated with 170 suns (1sun=1000 W/m^2). To obtain this illumination level, it is sufficient to use one single lamp to obtain the shortest time for the ageing test, as indicated Fig. 2.

B. The cooling system

The ASCMCL contains a cooling system since the temperature of the photovoltaic cells exposed to the concentrated light (170 suns), will increase rapidly and the photovoltaic cells will be damaged without cooling.

The cylindrical vessel cooling is made from aluminium, see Fig. 3 b. and it has two parts welded together under specific conditions. This design was made to ensure a very good water flow inside of the device and to ensure a quasi-constant temperature for the vessel base where the photovoltaic cells are mounted. It has one inlet and three outlets, see Fig.3 a.

The cooling vessel has some holes which permit the connection of the photovoltaic cells with the measure system and

also the fixing of the thermocouples used for the photovoltaic cells temperature measurement.

The automatic pump system ensures an adjustable flow of the cooling liquid that was established at 7 l/min during all measurements.

C. The measurement system

The measurement system consists of an electronic circuit able to measure the current-voltage characteristic of the photovoltaic cells with dynamic loads, a holder, the cRIO acquisition system and a remote connected (via Ethernet) to a PC with LabVIEW (Fig. 4).

The measurement system also allows the determining of the maximum power and of the current temperature for each of the four photovoltaic cells. These measurements allow studying the photovoltaic cells ageing process. The thermal camera also serves as back-up link in order to monitor the system temperature and as an alarm system for monitoring the temperature of photovoltaic cells.

The photovoltaic cells chosen for this experiment are: two multijunction Emcore photovoltaic cells with 1 cm^2 area and two monocrystalline photovoltaic cells with 0.3 cm^2 area each.

The photovoltaic cells were soldered on the small cooper plates which are in very good thermal contact with the cooling vessel, but are electrically isolated.

Four K thermocouples used to measure the photovoltaic cells temperature are mounted in intimal contact with the cooper plates.

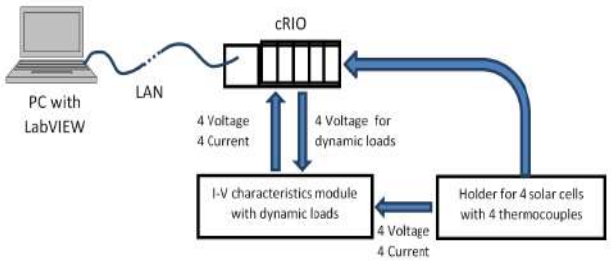

Fig. 4. The measurement system schemata

The measurement system was developed along the NI cRIO 9074 platform equipped with the following modules:

- NI 9215 –16 bits four simultaneously sampled analog input channels dedicated for measuring the solar cells voltage.
- NI 9227 – 24 bits four simultaneously sampled analog input channels dedicated for measuring the solar cells current;
- NI 9401 – 8 bidirectional digital I/O dedicated for independently triggering the four I-V solar cells characteristics measurement.

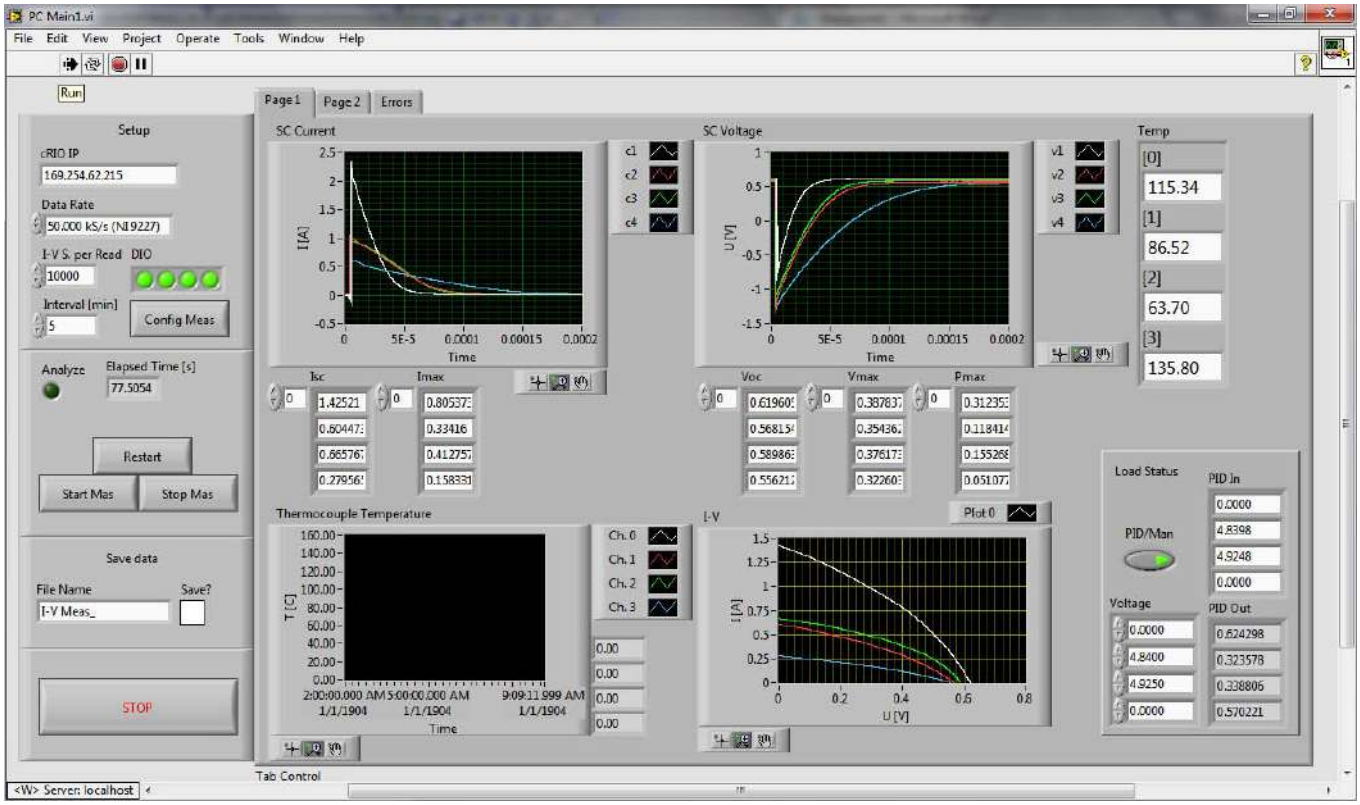

Fig. 5. The user interface of the PC monitoring application

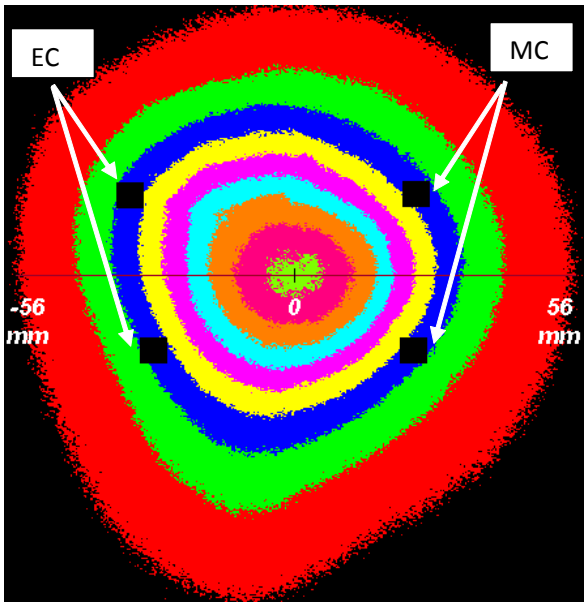

a)

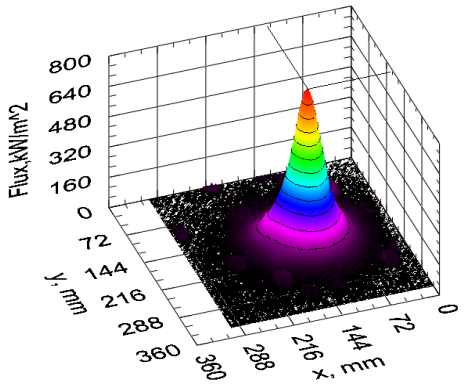

b)

Fig. 6. The radiative flux map and the positioning of the photovoltaic cells

- NI 9211 – four simultaneously sampled thermocouple channels used for measuring the each solar cell temperature.
- NI 9269 - four analog output channel-to-channel isolated modules used for controlling the load applied to the solar cell during the exposing period.

The NI cRIO platform was chosen because of the possibility to build an autonomous monitoring system which can work without the PC control, because the aging process is a long period process. So, the PC was used for measurement visualizing and for starting and stopping the measurement application. The measured data were stored in the internal memory of the NI cRIO platform, and at the end of the process were moved to the PC in order to be analysed. All applications was built in NI LabVIEW with LabVIEW FPGA add-on.

For the characteristic measurement, the capacitor method was used [13]. The value of the used capacitor is 22mF. The corresponding electronic circuit has four independently channels (one for each solar cell) and offers the possibility to apply a controlled load for each photovoltaic cell between two successive current-voltage characteristic measurements. The dynamic load was built based of a MOSFET, controlled by the NI 9269 module. In automatic operating mode, by using a PID algorithm, the load was fixed at values that kept the solar cell in the maxim power point, calculated for each measured current-voltage characteristic.

Fig. 5 shows the PC application used for visualizing the measured data from the cRIO module. This application allows the sending of the measurement parameters and also of the parameters for controlling the dynamic load applied to the solar cell.

The desired light intensity for the four photovoltaic cells was obtained through positioning the photovoltaic cells on the surface with the same light intensity (Fig. 6). The blue surface of the radiative flux map of Fig. 6 corresponds to 170 suns. To ensure a homogenous light intensity, the monocrystalline silicon photovoltaic (MC) cells were cut at a smaller area (0.3 cm^2) than Emcore (EM) cells (1 cm^2).

The flux distribution was measured using the Al_2O_3-coated target and CCD camera. The target that can be seen in Fig 3 is cooled by water, too [12].

The target and the cylindrical vessel were mounted on the XYZ table so that the photovoltaic cells are in the same plan with the front plane of the target and the vessel center at the same height with the center of the target. The flux distribution was measured on the target and after that the vessel was moved instead of the target.

For protecting the contact wires against radiation, Alumina paper was used.

III. Tests, Results and Discussion

Nowadays the life time for the monocrystalline silicon photovoltaic cells is considered to be of 25 years. In this period, the maximum power delivered by the photovoltaic cells decreases with 20%.

The accelerated ageing test targets also the decrease of the maximum power of the photovoltaic cells by these 20%.

The previous accelerated ageing test did not use light during the test. This paper introduces a new accelerated ageing test for the photovoltaic cells using the concentrated light.

Using the concentrated light, the photovoltaic cells are excessively warmed and no longer need a supplementary heating device in order to maintain the temperature of the photovoltaic cells at a specific desired temperature (e.g. 130°C in our experiment).

There are two significant effects which appear when the concentrated light falls on the photovoltaic cells: the light induced degradation and the thermal degradation, because the molecules at higher temperature have a high velocity and the number of collisions increases.

At the start of a test, the level of illuminations was increased step by step until 170 suns, in order to check the system's reliability.

The measurements were performed in four days at Paul Scherrer Institute, after testing the reliability of the system. The test duration in each day was seven hours. The intensity of the light the water flow were maintained constant on the entire measurement period.

The current-voltage characteristics and the temperature for each of the photovoltaic cells were measured at every five minutes and have been saved.

The maximum power of the photovoltaic cells was determined in real time, during the measurements to monitor the performance.

The measurements show that the maximum power of the photovoltaic cells decrease faster for the monocrystalline silicon photovoltaic cells than for Emcore multijunction photovoltaic cells. This result had to be expected because the Emcore cells are made to work at this intensity, but not at a temperature of 130°C.

One of the photovoltaic cells was measured with load and the other was measured without load for each of the two pairs of the photovoltaic cells. This was made to analyze the ageing behavior of the photovoltaic cells when these work or not.

The measurements show a faster ageing for the photovoltaic cells used without load than the ones used with load.

The current-voltage characteristic of the photovoltaic cells was measured in the same conditions at 1000W/m^2 before and after the ageing accelerated test. The current-voltage characteristics for the Emcore multijunction photovoltaic cell without load are presented in Fig. 7. The maximum power of the Emcore multijunction photovoltaic cell decreases with 1.5% and of the monocrystalline silicon photovoltaic cell decreases with 14% after the accelerated ageing test (28 hours, 170 suns and 130 °C). The ageing test is considered completed when the maximum power of the monocrystalline silicon photovoltaic cell decreases with 20%.

IV. Conclusions

The system which uses the concentrated light for the ageing accelerated test of the photovoltaic cells is presented in detail and also its functionality and reliability. The thermal device to warm the photovoltaic cells is avoided by using the concentrated light.

The created measurement systems is an autonomous one and it can be used without surveillance.

The time of the ageing accelerated test can be significantly reduced by using the new method proposed in this paper.

The measurements realized at Paul Scherrer Institute show a decrease of 14% for the maximum power of the monocrystalline silicon photovoltaic cell without load.

The reliability of the system allows determining the necessary time for the failure of the photovoltaic cell, which means that the maximum power has to decrease with 20%. These studies will be presented in the future works.

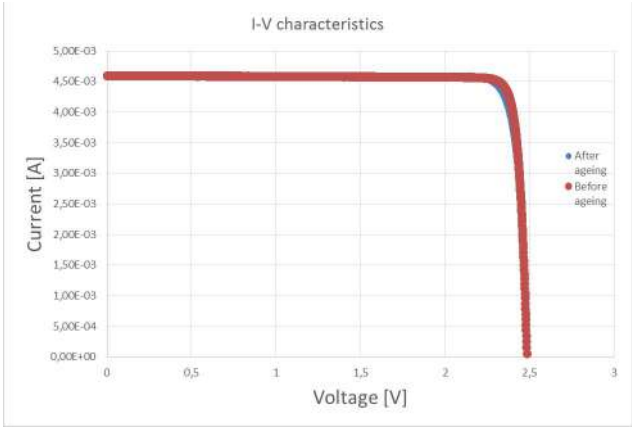

Fig. 7. The I-V characteristic

Also the temperature gradient in ASCMCL is very sensitive and depends on many parameters. For further research, based on these experiments, we performed a new design for cooling vessel more stable on temperature fluctuations.

Acknowlegement

Financial support by the Access to Research Infrastructures activity in the 7th Framework Programme of the EU (SFERA Grant Agreement n. 228296) is gratefully acknowledged.

The authors also kindly acknowledge and appreciate the support of Y. Baeuerle, D. Wuillemin and C. Wieckert as well as further co-workers from the Solar Technology Laboratory of Paul Scherrer Institute, Villigen, Switzerland, where all the measurements were performed.

References

[1] H. Cotal, C. Fetzer, J. Boisvert, G. Kinsey, R. King, P. Hebert, H. Yoon, N. Karam, "III–V multijunction solar cells for concentrating photovoltaics," *Energy & Environmental Science*, vol. 2, pp. 174–192, 2009.

[2] M.A. Green, K. Emery, Y. Hishikawa, W. Warta, E.D. Dunlop, "Solar cell efficiency tables (version 44)," *Progress in Photovoltaics: Research and Applications*, vol. 22, pp. 701–710, 2014.

[3] D. T. Cotfas, P. A. Cotfas and S. Kaplanis, "Methods to determine the dc parameters of solar cells: A critical review," *Renewable and Sustainable Energy Reviews*, vol. 28, pp. 588–596, 2013.

[4] L. A. Escobar, W. Q. Meeker, "A Review of Accelerated Test Models," *Statistical Science*, vol. 21, no. 4, pp. 552–577, 2006.

[5] J.H. Wohlgemuth, D.W. Cunningham, A.M. Nguyen, J. Miller, "Long Term Reliability of PV Modules, " *Proc. 20th European PVSEC*, Barcelona, Spain, pp. 1942, 2005.

[6] C.R. Osterwald, T.J. McMahon, "History of Accelerated and Qualification Testing of Terrestrial Photovoltaic Modules: A Literature Review, " *Progress in Photovoltaics: Research and Applications*, vol. 17, pp. 11–33, 2009.

[7] C. Algora, "Reliability of III–V concentrator solar cells, " *Microelectronics Reliability*, vol. 50, pp. 1193–1198, 2010.

[8] J.R. González, M. Vázquez, N. Núñez, C. Algora, I. Rey-Stolle, B. Galiana, "Reliability analysis of temperature step-stress tests on III–V high concentrator solar cells," Microelectronics Reliability, vol. 49, pp. 673–680, 2009.

[9] J. Petrasch, P. Coray, A. Meier, M. Brack, P. Haberling, D. Wuillemin, A. Steinfeld, "A Novel 50 kW11,000 Suns High-Flux Solar Simulator Based on an Array of Xenon Arc Lamps," *ASME J. Sol. Energy*, vol. 129, no. 4, pp. 405–411, 2007.

[10] P. Kuhn, A. Hunt, "A New Solar Simulator to Study High Temperature Solid-State Reactions With Highly Concentrated Radiation," *Sol. Energy Mater.*, vol. 24, pp. 742–750, 1991.

[11] American Society for Testing and Material, ASTM G173–03, "Standard Tables for Reference Solar Spectral Irradiance: Direct Normal and Hemispherical on 37° Tilted Surface," *ASTM International*, www.astm.org.

[12] I. Alxneit, H. Schmit, "Spectral Characterization of PSI's High-Flux Solar Simulator," *ASME Journal of Solar Energy Engineering*, Vol. 134, 011013, 2012.

[13] D.T. Cotfas, P.A. Cotfas, D. Ursutiu, C. Samoila, "Current-Voltage Characteristic Raising Techniques for Solar Cells. Comparisons and Applications," 12th International Conference on Optimization of Electrical and Electronic Equipment, OPTIM 2010, Brasov, Romania, 2010.

Measurements in Concentrated Sun using a Remote Controlled Robot

http://dx.doi.org/10.3991/ijoe.v9iS3.2544

Dan Floroian[1], Laura Floroian[1], Rachamim Rubin[2], Doron Lieberman[2], Petru Cotfas[1], Daniel Cotfas[1], Doru Ursutiu[1], Cornel Samoila[1]
[1] Transilvania University of Brasov, Romania
[2] Weizmann Institute of Science, Rehovot, Israel

***Abstract*—Nowdays, using the concentrated sunlight is a big issue because the amount of energy is very high and the light is concentrated in a very small area. The main problem in this situation is the heating, and in order to make safe measurements a remote controlled robot is needed. After that, a remote controlled robot will assume the duty of protect the measured sample and to expose it for a precise time to the concentrated sun in order to reduce heating of the sample. For easy operating, and for automatize the process, all the duties, starting with initial conditions, continuing with triggering the measurements, and conditioning the signals and finalizing with data saving must be assured by the robot.**

***Index Terms*—automatic measurements, concentrated sun, remote control, robotic arm.**

I. INTRODUCTION

A very promising renewable source of energy is concentrated solar power (CSP) obtained from solar concentrators. The solar North Africa continent and also Mediterranean countries of the European Union have a big resource of sun. The best known its application is electricity generation through thermodynamic cycles, but other applications have also been demonstrated, such as solar fuels and production of hydrogen, research in advanced materials and water treatment. Unfortunately the less studied process is the subject of solar cells in solar concentrator systems. Because of the boom of photovoltaic cells recorded in last years, we have in present many types of photovoltaic cells with different efficiencies and we don't have enough studies focusing of concentrated sun effects on these cells. The areas of applications is quite large starting with special equipment used on satellites and continuing with powerful power stations placed in suitable places on earth.

The concentrator makes it possible to focus sunlight falling on a large area onto a very small area. This increases the intensity of the solar radiation, leading to greater power falling on the area of focus. The solar intensity (or concentration ratio) is determined by the ratio of the area of incident sunlight to the area that it is focused on. Concentration ratios of the thousands have been achieved [1].

The use of solar concentrators creates the potential for the production of less expensive solar panels using high efficiency multi-junction cells or mono-crystalline cells. In general the materials used to build concentrators are less expensive than photovoltaic cells. The concentrator takes up most of the area of a concentrator system, and only a small amount of photovoltaic material is needed. Concentrator panels could reduce the cost per watt ratio in the point where solar power is an economical alternative.

Photovoltaic technology was developing since 1954 [1], but it is not a widely used source for the production of electricity yet. This is because the amount of produced power compared to the cost of solar panels makes their purchase uneconomical for most buyers. Significant gains have been made in the cost per watt ratio since the 1970's reducing the price from $70 per Watt to under $4 per Watt today [2]. However, this ratio needs to be reduced further before photovoltaic technology becomes a viable resource. Now the market is dominated by two types of photovoltaic cells. The silicon cells are the most widely used; they constitute 86% of the current market [2]. Mono crystalline cell technology is well developed in our days because it uses the same manufacturing techniques that are used in the electronics semiconductor industry. In this process, a mono silicon crystal is grown and then sliced into thin wafers. This produces identical and efficiently cells those are up to 15-17 percent efficient. However, the process is quite time consuming and pretty expensive. A less expensive but not so efficiently technique is the production of polycrystalline silicon cells. In this process molten silicon is poured into molds and allowed to cool, then sliced into wafers similar to those in the single crystal method. This method is very popular in these days. Many small silicon crystals are formed in the mold instead of one large one as in the single crystalline cell. This results in the efficiency of the polycrystalline cell being lower, between 11 and 14 percent [2].

The remaining 14% of the PV market is based on thin film semiconductors make up [2]. For this process, a thin film of semiconductor material (most often amorphous silicon) is deposited on an ordinary substrate such as glass or composite. This process is fast and uses much less material because the silicon layer is about one micron thick. Because thin film has no crystalline structure, it results in efficiencies of only six to eight percent. The low cost of production faces the poor efficiency, and thin films could be relevant in the future of the photovoltaic market.

Now days, efficient cells have been developed, but due to their high price, they are used mainly in research or in space technology. The most promising high-efficiency cell is the multi-junction cell. Multi-junction cells are several layers of photovoltaic cells stacked on top of one another. Each successive layer has lower band gap energy, allowing for the absorption of a wider range of the spectrum.

Figure 1. Solar tower

Figure 2. Heliostats field

Boeing holds the current record for the efficiency of a multi-junction cell at 34.2 percent [1]. This is more than twice the efficiency of cells currently on the market, and efforts are being made to increase the efficiency up to 40 percent.

Is not practical to build a solar panel out of multi-junction cells because they are so expensive in the present time. However, a solar concentrating system utilizing multi-junction cells could be cost effective. At present there are many different types of concentrators that could be used in a photovoltaic system. These concentrators can be divided into two different groups: reflecting concentrators and lenses. In the former group the most common concentrators are flat plate mirrors, spherical and parabolic mirrors, and cylindrical trough collectors. The most prominent lens is the Fresnel lens. It was developed in 1822 for use in lighthouses and can achieve high concentration ratios [1]. Newer lenses such as Aspheric lenses and TIR (Transmission, total Internal reflection, Refraction) lenses can be used together to achieve concentration ratios of over 300 while being only 2 cm thick.

The issue of using concentrators is not a simple problem because most concentrators rely on being directly focused on the sun; any deviation causes a severe drop in the concentration ratio. Some of the collected power must be used to run a tracking system. Also, though it seems that the power converted by a solar cell would increase indefinitely with increasing illumination, is not the case. As the intensity of illumination increases, the solar cell heats up. It is a well-documented fact that the efficiency of solar cells decreases as the temperature of the cell increases. The loss in efficiency is about 10% for every 25 K increase in temperature [3], although the exact loss in efficiency depends on the specific cell [4].

Also a too high temperature that can be achieved in such cases can damage the cell's integrity. This is particularly important in dish and tower systems where a maximum uniform flux may be difficult to achieve. A reliable cooling system is a very crucial issue, since any failure in the cooling system can lead to catastrophic results from cell damage to fire hazards in extreme cases. Coolants should be selected to minimize the health and environmental hazards. A simple design can help to reduce the maintenance costs.

Many cooling techniques have been proposed for cooling of solar PV cells under high concentration. These techniques aim to attain low and uniform cell temperature using simple designs. Royne et al. [5] have studied the cooling of densely packed photovoltaic cells under high concentration using a jet impingement technique. An optimization is performed for selecting the jet diameter to accommodate various cell illumination conditions. The jet cooling technique results in non-uniform heat transfer from the cells surface, although this non-uniformity didn't affect the electrical output strongly. Passive cooling techniques are employed with linear concentrators like the trough system where the concentration ratio is low, around 20 suns. Akbarzadeh et al. [6] used a heat pipe type passive cooling system with R22 refrigerant as a cooling medium to cool down a solar trough concentrated PV system. Using channels attached to the back of the PV cell, Lasich [7] managed to keep the cells at temperatures around 40°C. Recently was checked the validity and applicability for a new cooling technique, the immersion cooling [8].

This paper presents a method for experimental solar cells characterization into high concentrated solar light without using another cooling system than simple classical remove of heat from the back (opposite surface of the incident flux exposed surface) of the cell.

Our method consists of rapid measurement of cell current and voltage in about one second and immediately covering the cell for its protection against powerful solar radiation using a remote controlled automatic device.

The concentrated sun light was supplied by Solar Research Facility Unit from Weizmann Institute of Science, Rehovot, Israel.

The Solar Research Facilities Unit has a very sophisticated solar tower with a north field of 64 heliostats, 56 m^2 each, which on a bright day can collect 3 MW of solar radiation in total. The tower has 4 vertical experimental levels, 3 indoor and one outdoor on the roof for which special safety precautions are required for the tests. In addition, the facility has a unique 0.5 MW beam-down facility, which has no equal in any other solar research facility in the world (Fig. 1).

For our work we used one heliostat (Fig. 2) to obtain concentrated sunlight from 700 to 1000 suns and the whole experiment was made in order to obtain the parameters of different types of solar cells (commercial and manufactured). The determination of solar cells and panels' parameters is important for researchers, manufacturers and users as well as for stand-alone or on grid solar panels designers.

Figure 3. Heliostats field

There are several methods to characterize and determine the parameters of solar cells and panels. Most of these are based on using the current-voltage characteristic I-V. The parameters that can be determined using one or more I-V characteristics are: V_{oc} - open circuit voltage, I_{sc} – short circuit current, P_{max} - maximum power, R_{sh} - shunt resistance, R_s - series resistance, m - ideality factor of diode, FF - fill factor, I_o - reverse saturation current and η-efficiency.

A simple and quick method to characterize the solar cells and panels is the plotting of the I-V characteristic and its non-linear fitting using the one diode model, which mathematically describes the behavior of photovoltaic cells [9]. The approximation used for the fitting is

$$V_{max} \gg I_{max} R_s \tag{1}$$

and thus the equation describing the one diode model becoming explicit (2).

$$I = I_{sc} - I_0\left(e^{\frac{qV}{mkT}} - 1\right) - \frac{V}{R_{sh}} \tag{2}$$

The fitting ensures the determination of the following parameters: I_o, I_{sc}, R_{sh}, m, P_{max} and implicitly η and FF can be determined using the P-V (power- voltage) characteristic [10].

II. ROBOTIC ARM

In order to achieve information at high concentration of solar radiation, is necessary to build a special remote controlled robotic device because the temperature on cell is around 1000 °C and ordinary solar (not specially very high temperature designed) cells or electrical contacts couldn't resist. This remote controlled robotic device is constructed with two parts that work together: an I-V module and a robotic arm.

I-V module is based on high capacitors (minimum 0.4 Farads) which also has very low internal resistance. In this situation, we are able to obtain characteristics in less than 1 second and to expose the cell very shortly in order to reduce cell heating. First, the robot shortcuts the capacitor in order to obtain a fresh measurement; second, it moves the robotic arm to uncover the solar cell and triggers the measurements when the robotic arm is in position; in the third step it covers the solar cell and in the last operation saves the data into a file. The robot works under control of 12 bits National Instruments acquisition board which is also controlled by a program in the graphical programming language Lab VIEW. The Lab View program was created to interface both with the user and the computer.

At beginning the user start program computer and this program send a message to the robot using NI board. At the moment of receiving this message, the robot will close a relay in order to produce a discharge of high capacity capacitor with the purpose of recording only the voltage acquired in measurement period of time. After this process is completed, the computer program will be noticed (again using NI boards) and it will pass to the next step, respectively sending another message to the robot. This second message will instruct robot to move the arm in order to uncover the sample. When the movement is completed, a sensor is activated and the computer program receives a message from controller program thru NI board. At this time, the NI board is activated in acquisition mode and the measurement starts. This measurement is maintained for 1s and after that is stopped. During this period of time 1000 samples are collected. The length of acquisition time (and of course the number of samples) is determined in computer program also.

After measurement, the computer program flow to the next step and sends a stop message to acquisition board and to the robot also. At receiving the message, the robot will move back its arm and will cover back the sample. After this process is completed, the computer program will receive a message for "job done" confirmation. In every step of the described process an error tag is positioned in case of malfunction and the computer program will show an error message in order to clarify the occurred problem.

The controller is based on ATMEGA microcontroller and all parallel ports are used in order to assure all necessary functions. Furthermore it could be said that in the same time communications with computer is provided and also communication with acquisition board, with sensors and I-V module are supplied.

III. I-V DRIVER AND LABVIEW PROGRAM

There are various devices and techniques used by research for raising the solar cells I-V characteristics.

Among the most widely spread is the use of the electronic load.

There are three methods to operate an electronic load: the constant current, the constant voltage, and the constant resistance; from these it is advisable to use the constant voltage, when the voltage is varied with the desired step and the current on the cell is measured.

But the use of the electronic load presents two disadvantages. One of them is the duration of the I-V characteristic raising and the other one is the high cost. The duration is in general of tens of seconds, enough to modify the cells temperature. This fact leads to variations of solar cells parameters during the measurements.

To avoid this temperature variation a thermostat can be used to maintain the temperature constant during measurements.

However an impediment appears because the solar panels as well as the solar cells are encapsulated, this making the use of the thermostat more difficult.

To remove all these drawbacks our I-V characteristic module (Fig.4) is designed using the charging schematics of a large capacitor. The functioning principle that under-

lies this technique is measuring the current and the voltage during the charging of the capacitor. The time duration of raising the I-V characteristic of the solar cell is in hundredths of a second range, fact that ensures that the cell temperature variation during measurement is practically zero. Another advantage is the high number of (V, I) points which can be acquisitioned. The large number of points allows a very good fitting of the I-V characteristic.

In aim of achieve a short charging time and because we need a large capacity, it is mandatory to have a very small internal resistance (≈ 40 mΩ). Also in the same direction it is necessary that the resistance for current measurement to have a very small resistance (20 mΩ).

Furthermore the voltage on the resistance is very small and needs to be amplified before sending the signals to the measurement equipment.

The conditional amplifiers are conducted by microcontroller on robotic arm and could be programed in order to amplify with 10 or 100. After that, the signal could be passed on shielded wires to the acquisition board. For a good insulation digital signals are separated from analogical using different cables, also shielded.

For highly accurate measurements a National Instruments NI 6009 acquisition board was chosen, with 8/4 analog input (AI) channels in the configuration Single-Ended Channels/Differential Channels with a sampling rate of 48kS/s and 14 bits resolution, 12 Digital Input / Output (DIO), two analog input channels AO of a 12 bits resolution and a counter. The connection of the board to a laptop is realized by a USB connection.

The program for data acquisition is made using the visual VIs provided by default and configuring it. The only special issue is that signals are forced in 1 and lowered in 0 only in time of the action in order to prevent the perturbations, especially because of electromagnetics perturbations in this special experiment. The user interface is presented in figure 5.

Software applications were created in the graphical programming language LabVIEW to control the circuit, to automatically raise the I-V characteristic and to determine the parameters. The applications were then compiled into one complex application. The application is created on tabs, see Figure 5. The first tab "Raising of I-V characteristic" permits the control of the acquisition board, the control of the capacitor, the plotting of the I-V characteristic and the saving of the data. The tab "Determination of parameters" permits the import of the processing file and the determination of the interest cells parameters using the method of the nonlinear fitting. The other methods to determine the parameters of the solar cells and panels described in the theoretical considerations were implemented as sub-tabs in the tab "Applications".

IV. RESULTS

Using the method just we studied different types of solar cell behavior in concentrated light:

- at different solar illumination level (700, 900 and 1000 suns)
- at different temperatures (24 and 30 degrees Celsius)
- at different wavelengths in UV-VIS-IR range: 461 nm, 508 nm, 591 nm, 623 nm, 672 nm, 766 nm, 773 nm, 793 nm, 795 nm.

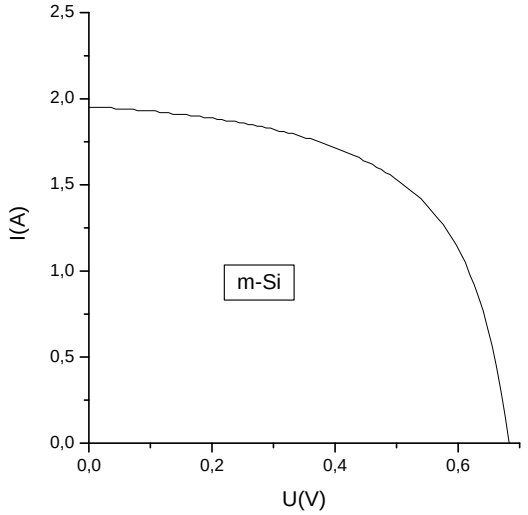

Figure 4. I-V Characteristic

We founded correlation between the laser deposition parameters and the optical and electrical properties of the layers and also we determined properties and parameters of the solar cells under concentrated solar power: short-circuit current, cell efficiency, open circuit potential, fill factor, maximum power, series and shunt resistance. We recorded simultaneously current intensity, voltage, flux and intensity of radiation using 4 channels of data acquisition plaque, for each solar cell.

An example of I-V characteristic of Si monocrystalline cell at 700 suns is presented in figure 6. It shows a different shape from one sun irradiation level, it has a high short circuit current and open circuit potential is V_{oc}=0.659 V. Table I shows the values of the cells parameters obtained at 700 suns using the method before described.

V. CONCLUSIONS

This paper presents a method for experimental solar cells characterization into high concentrated solar light without using another cooling system than simple classical remove of heat from the back (opposite surface of the incident flux exposed surface) of the cell.

Our method consists of rapid measurement of cell current and voltage in about one second and immediately covering the cell for its protection against powerful solar radiation using a remote controlled automatic device.

The remote controlled robot was able to complete its mission in protecting the solar cells and in raising the I-V characteristics of 4 different solar cells and in more than 400 different experiments.

The whole system (which brings together digital electronics, analog electronics, data acquisition board, a laptop and LabView program) worked fine even in strong electromagnetically perturbation.

ACKNOWLEDGMENT

Financial support by the Access to Research Infrastructures activity in the 7th Framework Programme of the EU (SFERA Grant Agreement n. 228296) is gratefully acknowledged.

Also the Romanian authors acknowledge with thanks the support of Solar Research Facility Unit from Weizmann Institute of Science, Rehovot, Israel, where all the measurements were performed.

REFERENCES

[1] B. Parida, S. Iniyan, R. Goic, "A review of solar photovoltaic technologies", *Renewable and Sustainable Energy Reviews*, vol. 15, Issue 3, pp. 1625-1636, 2011. http://dx.doi.org/10.1016/j.rser.2010.11.032

[2] F. Dinçer, "The analysis on photovoltaic electricity generation status, potential and policies of the leading countries in solar energy", *Renewable and Sustainable Energy Reviews*, vol. 15, Issue 1, pp. 713-720, 2011. http://dx.doi.org/10.1016/j.rser.2010.09.026

[3] M.A. Mosalam Shaltout, M.M. El-Nicklawy, A.F. Hassan, U.A. Rahoma, M. Sabry, "The temperature dependence of the spectral and efficiency behavior of Si solar cell under low concentrated solar radiation" *Renewable Energy*, vol.21, pp. 445-458, 2000. http://dx.doi.org/10.1016/S0960-1481(00)00075-6

[4] E. Radziemska, E. Kleugmann, "Thermally Affected Parameters of the Current-Voltage Characteristics of Silicon Photocell" *Energy Conversion and Management* vol.43, pp. 1889-1900, 2002. http://dx.doi.org/10.1016/S0196-8904(01)00132-7

[5] A. Royne, C.J. Dey, "Design of a jet impingement cooling device for densely packed PV cells under high concentration", *Solar energy*, vol. 81, pp. 1014–1024, 2007. http://dx.doi.org/10.1016/j.solener.2006.11.015

[6] A. Akbarzadeh, R. Singh, H. Fan, "Electric power generation by thermoelectric cells and parabolic solar concentrators", Proceedings of the Solar09, the 47th ANZSES Annual Conference, 29 Sept – 2 Oct, 2009, Townsville, Queensland, Australia.

[7] J.B. Lasich, "Cooling circuit for receiver of solar radiation", Patent WO02080286, Australia, 2002

[8] L. Zhu, R.F Boehm, Y. Wang, C. Halford, Y. Sun, "Water immersion cooling of PV cells in a high concentration system", *Solar Energy Materials and Solar Cells*, vol. 95, Issue 2, pp. 538-545, 2011. http://dx.doi.org/10.1016/j.solmat.2010.08.037

[9] D.T. Cotfas, P.A. Cotfas, S. Kaplanis, D. Ursutiu, " Results on series and shunt resistances in a c-Si PV cell", J *optoelectron adv m.,* vol. 10, pp. 3124-3130, 2008.

[10] D.T. Cotfas, P.A. Cotfas, D. Ursutiu, C. Samoila, "Current-Voltage Characteristic Raising Techniques for Solar Cells. Comparisons and Applications", 12th International conference on optimization of electrical and electronic equipaments, Brasov, Romania, IEEE Xplore Digital Library, 2010.

AUTHORS

Dan Floroian, Laura Floroian, Petru Cotfas, Daniel Cotfas, Doru Ursutiu, and **Cornel Samoila** are with Transilvania University of Brasov, Romania.

Rachamim Rubin and **Doron Lieberma**n are with the Weizmann Institute of Science, Rehovot, Israel.

This article is an extended and modified version of a paper presented at the International Conference on Remote Engineering & Virtual Instrumentation (REV2012), held at University of Deusto, Bilbao, Spain, July 4-6, 2012. Received 01 March 2013. Published as resubmitted by the authors 20 March 2013.

General Physics Remote Laboratory based on the NI ELVIS Platform and Moodle

P.A. Cotfas[1], D. T. Cotfas[1], L. Floroian[2], D. Floroian[2]
[1]Transylvania University of Brasov / DEC Department, Brasov, Romania
[2]Transylvania University of Brasov / ATI Department, Brasov, Romania

***Abstract*—The present paper presents a solution to implement remote laboratories for General Physicscourses based on the NI ELVIS hardware platform and the e-learning platform Moodle. The NI ELVIS controlling applications were built in the NI LabVIEW software. At the same time, LabVIEW was used for online publishing of the user interfaces.**

***Index Terms*—Moodle, LabVIEW, remote panels.**

I. Introduction

In the technical learning-teaching process, the laboratory component is an important part. The evolution of the educational process leads to the integration of the distant learning facilities in the system.

The MOOCs-Massive Open Online Courses concept was introduced in 12008, referring to online courses that can allow unlimited participation with open shared curriculum accessed via web [1]. Alongside the theoretical aspect, the educational process must be accompanied by the practical process. The MOOCs concept is now completed with the laboratory part, using remote laboratories. So, the new MOOLS – Massive Open Online Laboratories concept is increasingly used.

One of the issues of the remote laboratories is the implementation proceeding. How to build the user interface, how to publish it on the web and how to integrate it in the learning management system? There are a lot of open or proprietary solutions to solve these issues [2][3][4]. In this paper, we present a solution for remote laboratories implementation based on the:

- Moodle platform – used for learning content management,
- NI ELVIS platform – used as hardware support,
- NI LabVIEW software – used as environment for hardware control applications and also as user interface web publisher.

The implemented remote laboratories are dedicated to the General Physics courses taught to the Electrotechnics, Automation and Applied Informatics, Civil, Industrial and Agricultural Engineering and Installations for Civil Engineering specializations. The number of the students who are currently using the developed remote laboratories is over two hundred. The remote laboratories applications are used both for students, as laboratory works, and also for professors as demonstration support in the teaching process.

II. The Remote Laboratory Implementations

The structure of our remote laboratories is shown in Fig. 1. It consists of a main server that contains the Moodle platform, the MySQL Database server and the LabVIEW software.

We chose to use the Moodle platform due to its widespread acceptance. Moodle is an open source course management system that can be used to create online learning sites.

On the http://moodle.org web site, the ready-to-use installer packages can be downloaded and the whole installation process is straightforward. The installer packages also contain a web server (Apache), a database server (MySQL), and the PHP script software.

There is a large offer for learning management systems on the market. We chose the Moodle platform due to its

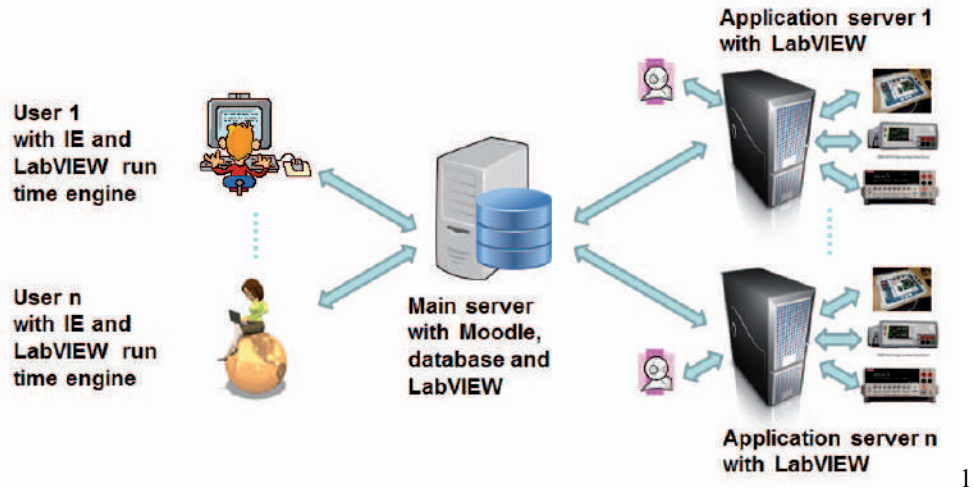

Figure 1. The implemented remote laboratories structure

978-1-4799-2024-2/14/$31.00 ©2014 IEEE Polytechnic of Porto (ISEP) in Porto, Portugal from 26-28 February 2014
2014 11th International Conference on Remote Engineering and Virtual Instrumentation (REV)

relative easy installation, worldwide usage and because it is open source, having in mind the possibility to develop new modules, such as an online booking system for laboratories [5].

The MySQL Database server is used for the Moodle platform but also for communications between the LabVIEW applications on the main server and the applications on the Application servers.

The LabVIEW applications on the main server are used as user interfaces that are published online. Using these interfaces, the client sends commands and receives the results from laboratories. The communication between the two applications is made through the database.

The database contains a table for each laboratory. In this table there are fields that contain the status of each application, if the application is active or not. At the same time, the table contains fields that store the results sent by the hardware controlling applications (HCA) from the Application Server and also store the commands sent by the user through the online user interface application (UIA). Other fields store the status of the application response: if the response is sent or not, or if a new command is sent or not.

If a new command is sent by the user, then, the command and the command status, which is changed to *True*, are stored in the database. HCA follows the command status and when this becomes *True*, it reads and executes the command. After execution, the HCA sends the response to the database and changes the response status to *True*. When the response status becomes *True*, the UIA reads the results and resets both statuses.

The UIA is online published based on the remote panel technique given by LabVIEW through the Web Publishing Tool. For this, it is necessary to have two web servers on the main server. The main web server (Apache), which serves the Moodle platform, is configured on the default web port (80) and the LabVIEW web server, which serves the UIA, is configured on the 8080 port. The LabVIEW published object through the remote panel technique is inserted in the laboratory's Moodle page (Fig.2). In this manner, the laboratory access and security is provided by the Moodle platform.

The actual online publishing technique was chosen because it is user-friendly for non-specialists web programmers, as it is shown in [6]. The communication through the database between HCA and UIA is given to the remote laboratory developer as a LabVIEW add-on developed by the authors, so the implementation is made easier.

The communication technique gives developers the flexibility to use different solutions for the UIA implementation, such as Java Applets or other modern web programming techniques. The developers need to adapt their applications to communicate with the database and not with HCA.

At the same time, the communication technique that is being used allows building a spread structure of the remote laboratory. The Application servers can be placed anywhere. The only condition is to have the possibility to be connected to the database on the main server. The user is connected to the laboratory through UIA, which communicates only with the database server without knowing where the HCA is running.

A video streaming was implemented in order to have a visual contact between the user and the hardware. The video streaming is also based on the remote panel publishing technique. In this case, a LabVIEW application for video capturing from a web camera was developed. The panel of this application is published online using the remote panel technique from LabVIEW, too. But in this case, the publishing is made as a monitor, which means that the panel is published as a snapshot, which is updated at a given time interval (0.3 s - 0.5s). In the Moodle page, the LabVIEW snapshot is inserted (Fig.2). With this technique, 12-3 frame/s are obtained for video streaming, which is enough for four remote labs.

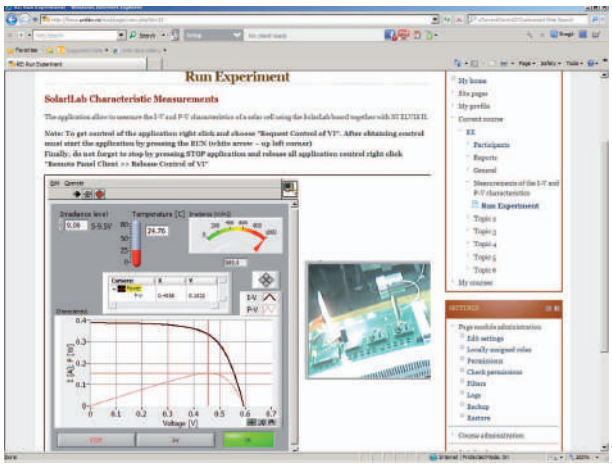

Figure 2. The Moodle page for remote laboratories interfaces

From the hardware perspective, we used the NI ELVIS platform to implement the laboratory works. The NI ELVIS platform offers all needed laboratory apparatuses, such as: the function generator, digital multimeter, oscilloscope, bipolar variable power supply, impedance analyzer and spectral analyzer. A lot of lab experiments can be implemented by using these apparatuses. Another reason for choosing the NI ELVIS is the possibility to control it with applications developed in LabVIEW. In this manner, the online publishing of the applications becomes easy.

III. LABORATORIES WORKS

The authors taught the General Physics courses to the Electrotechnics, Automation and Applied Informatics, Civil, Industrial and Agricultural Engineering and Installations for Civil Engineering specializations. The associated laboratory works for this course have been done face to face up to now, on the basis of classical apparatuses. Now, the laboratory works are done in a mixed manner, in the sense that the students are split in two groups. The first students' group performs the laboratory work hands on, and the second group performs the laboratory work remotely. In this manner, the results of using both hands on and remote approaches can be studied.

In this stage, four laboratory works were developed and integrated in the teaching learning process. These laboratory works are:

- Composition of Two Perpendicular Oscillations - the Lissajous curve;
- The Study of Boltzmann Distribution;

- The Study of Electrical Resistivity Depending on the Temperature;
- I-V Characteristic For Two Terminal Semiconductors – Solar Cell.

A. Composition of Two Perpendicular Oscillations - the Lissajous curve

This laboratory work is dedicated to the study of the composition of two perpendicular oscillations. As the result of composition, the Lissajous curves are obtained. The two oscillations on perpendicular directions are obtained using a transformer connected to the main power network (PNT) and the functions generator offered by the NI ELVIS platform (NI ELVISFG), see Fig.3. Knowing the frequency of one oscillation (the one generated by NI ELVIS FG), the frequency of the other can be calculated based on (1):

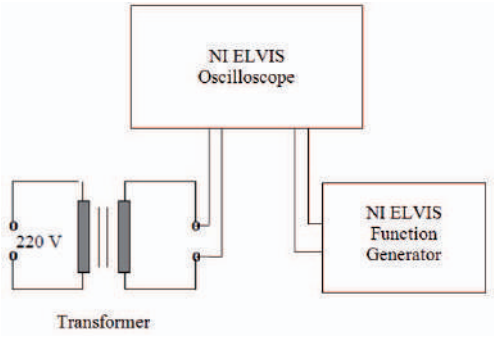

Figure 3. Schemata of the experimental system

$$\upsilon_y = \frac{n_x}{n_y}\upsilon_x . \quad (1)$$

where n_x and n_y represent the number of intersection points between the figure and the coordinates axes Ox and Oy, and ν_x and ν_y represent the frequencies of the two oscillations.

The remote interface of this application is shown in Fig.4.

Figure 4. The Moodle page for Lissajous application

B. The Study of Boltzmann Distribution

This laboratory work is dedicated to the study of the distribution of the gas molecules depending on the potential energy.

The distribution is given by (2):

$$N = N_o e^{-\frac{U}{kT}} . \quad (2)$$

where N_0 represents the total number of molecules, U is the potential energy, k is the Boltzmann constant, and T is the temperature.

For easiness, the studied gas is the electronic gas obtained inside of a vacuum tube diode (VTD). In this case, the Boltzman distribution can be written as follows:

$$N = N_o e^{-\frac{eU_f}{kT}} \quad (3)$$

where U_f represents the braking voltage.

The electronic gas is obtained inside of the VTD as follows: applying a current through the filament of the diode, this warms the cathode and by thermo-electronic emission the electronic gas is created.

As the intensity of the anodic current created by thermo-electronic emission is small, an amplifying circuit based on an instrumental amplifier is used. To study the distribution of the electrons, a braking voltage is applied between the anode and cathode.

The intensity of the anodic current is given by the number of electrons whose potential energy is higher than the braking energy eU_f.

The experimental mounting is made on the prototyping board of the NI ELVIS platform.

The remote interface of this application is shown in Fig.5.

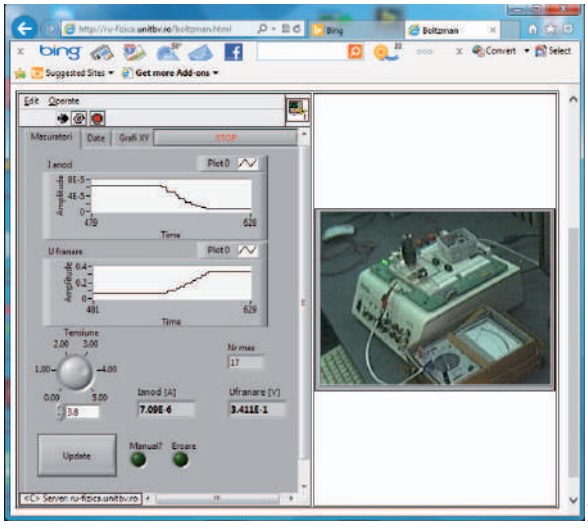

Figure 5. The Boltzman distribution remote interface

C. The Study of Electrical Rezistivity Depending on the Temperature

The application is dedicated to the study the dependency of the electrical resistivity of a copper wire on the wire temperature.

The resistivity depends on the thermal chaotic motion, and also on the spreading of the waves associated with the electrons of impurity atoms. In the domain of the temperatures used to realize the experiment, the resistivity is proportional with the temperature, the proportionality relation being given by equation (4):

$$\rho = \rho_0\left(1+\alpha\cdot t\right). \quad (4)$$

where ρ_0 and ρ represent the wire resistivity at 10^0C and respectively at temperature t, and α represents the thermal coefficient of the material.

The resistivity is determined by measuring the wire resistance R using a digital multimeter and applying (5):

$$\rho = R\frac{A}{l}. \quad (5)$$

where l is the length and A is the area of the section of the studied wire.

The studied resistor is a copper wire that has the following geometrical dimensions: length l=13.51m and diameter l=10.24mm. To increase the temperature of the copper wire, a power resistance is used as a heater. The copper wire is convoluted around the power resistance. This system is encapsulated to get a small temperature gradient.

The adjustment of the temperature with the desired step is made using the PID algorithm.

The temperature is measured with the temperature sensor LM135, which is in contact with the copper wire, contact made with silicon paste.

The experimental mounting is made on the prototyping board of the NI ELVIS platform.

The remote interface of this application is shown in Fig.6.

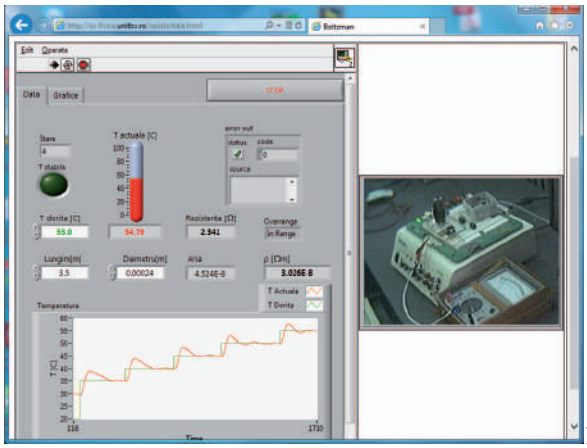

Figure 6. The Resistivity vs Temperature user interface

D. I-V Characteristic for Two Terminal Semiconductors – Solar Cell

The fourth laboratory work is dedicated to study the photoelectric effect based on a photovoltaic cell.

The laboratory is based on the RELab board developed as an add-on for the NI ELVIS platform [7][8].

The mathematic model that describes the I-V characteristic in this case is given by the following equation:

$$I = I_{sc} - I_o\left(e^{\frac{q(V+IR_s)}{mkT}} - 1\right) - \frac{V+IRs}{R_{sh}}. \quad (6)$$

where I_{sc} is the short circuit current, I_o is the reverse saturation current, R_s represents the series resistance, R_{sh} is the shunt resistance, m is the ideality factor of the diode, T is the temperature, k is the Boltzmann constant, and q is the elementary electric charge.

Using the RELab add-on, the I-V characteristcs of the solar cell can be measured and interpreted.

The remote interface of this application is shown in Fig.2.

IV. Conclusions

The present paper presents a solution for implementing the remote laboratory works based on the Moodle software platform and the NI ELVIS hardware platform.

The Moodle platform was used as a content management system. By inserting the laboratory works as pages into the Moodle platform, the access and security of the platform is applied also to the remote laboratory pages.

The online publishing user interface is based on the web publishing tool offered by NI LabVIEW. In this manner, it is not necessary to have web programming knowledge.

The developed laboratory works are dedicated to the General Physics course for engineering. The first three applications were developed on the same NI ELVIS platform reducing the space and cost of the used apparatuses. The fourth application is based on the RELab NI ELVIS add-on.

The adopted solution offers a variant for non-web programming specialists to implement a powerful remote laboratory system.

References

[1] A. McAuley, B. Stewart, G. Siemens and D. Cormier, "The Mooc Model For Digital Practice" http://www.elearnspace.org/Articles/MOOC_Final.pdf, 2010.

[2] Gustavsson, I., Zackrisson, J., Hakansson, L., Claesson, I. & Lagö, T.L., "The VISIR project – an Open Source Software Initiative for Distributed Online Laboratories", *In: Proceedings of REV 2007 Conference*, Porto, Portugal, 2007.

[3] Gustavsson, I., Zackrisson, J., Nilsson, K., Garcia-Zubia, J., Håkansson, L., Claesson, I., Lagö, T. "A Flexible Electronics Laboratory with Local and Remote Workbenches in a Grid", *International Journal of Online Engineering*, 4(2), 2008.

[4] Salzmann, Ch., Gillet, D., "Remote Labs and Social Media. Agile Aggregation and Exploitation in Higher Engineering Education", IEEE Global Engineering Education Conference (EDUCON), Amman, Jordan, 307-311, 2010.

[5] José M. Martins Ferreira, António M. Cardoso, "A Moodle extension to book online labs", International Journal of Online Engineering (iJOE), Vol 1, No 2, 2005

[6] ***, "Remote Panels in LabVIEW -- Distributed Application Development", http://www.ni.com/white-paper/4791/en, 2013

[7] P. A. Cotfas, D. T. Cotfas, D. Ursutiu, C. Samoila, and D. Iordache, "Chapter 3-*New Tools in Hardware and Software Design Applied for Remote Photovoltaic Laboratory*", Abul K. M. Azad, A. K. M., Auer, M., V. Judson Harward, V. J. "*Internet Accessible Remote Laboratories: Scalable E-Learning Tools for Engineering and Science Disciplines*", IGI Global, pp. 40-59, 2012.

[8] P. A. Cotfas, D. T. Cotfas, "Developing a Renewable Energy Laboratory Using NI ELVIS, NI LabVIEW, and NI myDAQ", Case Studies, http://sine.ni.com/cs/app/doc/p/id/cs-15465

The Institute of Electrical and Electronics Engineers Industrial Electronics Society

Proceedings of the 2017 International Conference on Optimization of Electrical and Electronic Equipment (OPTIM) & 2017 Intl Aegean Conference on Electrical Machines and Power Electronics (ACEMP)

Brasov, Romania

TT05 Mechatronics-Automation and Applied Electronics

PDF file Cover

A Compact Robotic Head for Automatic Acquisition of Indoor Panoramic Images

Authors :
Mr. Bogdan Sendrut, Technical University of Cluj-Napoca, Romania
Ms. Aurelia Ciupe, Technical University of Cluj-Napoca, Romania

Fever Detection for Dynamic Human Environment Using Sensor Fusion

Authors :
Mr. Hamidreza Fallah-Haghmohammadi, University of Ottawa, Canada
Prof. Dan-Sorin Necsulescu, University of Ottawa, Canada

***Abstract*—** The objective of this paper is to present an algorithm for processing infrared images and accomplishing automatic detection and path tracking of moving subjects with fever. The detection is based on two main features: the distinction between the geometry of a human face and other objects in the field of view of the camera and the temperature of the radiating object. These features are used for tracking the identified person with fever. The position of camera with respect to direction of motion the walkers appeared to be critical in this process. Infrared thermography is a remote sensing technique used to measure temperatures based on emitted infrared radiation. This application may be used for fever screening in major public places such as airports and hospitals.For this study,we firstlook at human body and objects in a line of view with different temperatures that would be higher than the normal human body temperature (37.8C at morning and 38.3C at evening). As a part of the experimental study, two humans with different body temperatures walking a path were subjected to automatic fever detection applied for tracking the detected human with fever. The algorithm consists of image processing to threshold objects based on the temperature and template matching used for fever detection in a dynamic human environment.


PDF file Full paper

Fractional Adaptive Control for a Fractional - Order Insuline - Glucose Dynamic Model

Authors :
Mrs. Simona Coman, Transilvania University of Brasov, Romania
Mr. Cristian Boldisor, Transilvania University of Brasov, Romania
Mrs. Laura Floroian, Transilvania University of Brasov, Romania

***Abstract*—** A new approach to the blood glucose concentration control problem is investigated in this paper. The solution implies the use of fractional-order calculus both for the plant's model and for the controller. A fractional-order model of the insulinglucose system is derived from the well-known minimal model, by replacing the integer derivatives with fractional ones. Next, fractional-order calculus is used to extend the conventional model reference adaptive control, namely by using a fractional-order adjustment rule for the controller's parameters. The controller's design procedure is detailed. Simulations of the proposed control system show the performance in reducing the blood glucose concentration when meal glucose disturbances are considered.


PDF file Full paper

Further analysis on network-induced time-varying delay modeling methods used in GPC design

Fractional Adaptive Control for a Fractional – Order Insuline – Glucose Dynamic Model

Simona Coman, Cristian Boldisor, Laura Floroian
Automatic Control and Information Technology Department
Transilvania University of Braşov,
Braşov, Romania
simona.coman@unitbv.ro

***Abstract*—A new approach to the blood glucose concentration control problem is investigated in this paper. The solution implies the use of fractional-order calculus both for the plant's model and for the controller. A fractional-order model of the insulin-glucose system is derived from the well-known minimal model, by replacing the integer derivatives with fractional ones. Next, fractional-order calculus is used to extend the conventional model reference adaptive control, namely by using a fractional-order adjustment rule for the controller's parameters. The controller's design procedure is detailed. Simulations of the proposed control system show the performance in reducing the blood glucose concentration when meal glucose disturbances are considered.**

Keywords—Fractional-order systems; insulin-glucose fractional order model; fractional order adaptive control.

I. INTRODUCTION

Although the fractional-order calculus has long history in mathematics, the idea of using it in control engineering is relatively new. The first applications are the CRONE controller presented by Oustaloup in [1] and the $PI^{\lambda}D^{\mu}$ generalization of PID controllers introduced by Podlubny in [2]. The main restriction was the absence of solution methods for fractional differential equations. Also, the complexity of the mathematical subject and low computing power available a few decades ago limit its use in engineering.

However, at present time, many methods to approximate fractional derivative and integral are available, thus the number of applications using fractional-order calculus rapidly grows, including process modelling and control [3-4]. In control systems, the motivation for such an approach would be the fact that most real processes are fractional, so a fractional-order model would describe the real dynamics more accurately than an integer-order model [3]. Examples are presented in [1], [4-7]. When having such model, using a fractional-order controller is reasonable, as design methods for such controllers were also developed and tested in applications. Even more, many authors pointed out that a fractional-order controller can perform better than an integer-order one [7-10]. Other common problems in systems theory, such as stability analysis, controllability, observability, control performance were studied for fractional-order control systems as well (for a review of fractional-order control theory and applications please refer to [3-6]).

When it comes to closed-loop fractional-order control applications, there are four situations [3]: i) integer-order plant with integer-order controller; ii) integer-order plant with fractional-order controller; iii) fractional-order plant with integer-order controller; iv) fractional-order plant with a fractional-order controller. The latter is used in this paper.

An even newer approach is to combine fractional-order calculus with adaptive control concepts or methods, in order to overcome the risks of inexact parameters' value. Common concepts as model reference adaptive control and MIT adjustment rule [11] are modified to fractional-order reference model [8], [10] and fractional adjustment rule [10]. The latter proposes a modification of the conventional MIT rule in which the parameter adjustment is done with a fractional-order differential equation. The method is referred as adaptive control with fractional adjustment rule.

In this paper, the theory related to fractional-order adaptive control is applied in simulating a control system for blood glucose concentration. More specifically, we simulate an adaptive control system in which the parameter adjustment rule is done by fractional-order equations. A fractional-order model of the insulin-glucose system is introduced in Section II and further used in simulations. In Section III, we present a modification of the MIT rule, to be applied to the derived fractional order model. The proposed algorithm is a fractional MIT adjustment rule [8], [10]. The motivation for fractional-order calculus in adaptive control is justified by the very good control performance related to the integer-order [3]. Finally, in Section IV simulation results are detailed to demonstrate the validity of the method.

II. A FRACTIONAL-ORDER INSULIN-GLUCOSE MINIMAL MODEL

Many insulin-to-glucose nonlinear models were proposed over the years, validated by simulations and clinical trials. Different approaches were considered. Some models are focused on the details of the biological phenomena, while others are simplified in order to use them in designing glucose control systems [12]. The most widely used is the *minimal model*, which is based on the model introduced by Bergman et al. [13], and adapted by Cobelli et al. [14] for type-1 diabetes mellitus patients. The minimal model offers the possibility of using control theory (conventional or advanced) to design automatic glycaemia controllers. The model describes the dynamics of the blood glucose concentration under external insulin deliver rate or glucose disturbance input (as a meal).

In this paper, we consider a fractional-order model, based on the minimal model, in which we replace the original integer-order derivatives with fractional-order ones. The modification introduces a new parameter, the derivation order $\alpha \in (0,1]$, which is an alternative way to catch the patient's particular response to insulin injection.

The model is described as [18]:

$$\begin{aligned} D_t^{\alpha} G(t) &= -[p_1 + X(t)]G(t) + p_1 G_b + m(t) \\ D_t^{\alpha} X(t) &= -p_2 X(t) + p_3 I(t) \\ D_t^{\alpha} I(t) &= -nI(t) + \tau u(t) \end{aligned} \quad (1)$$

where D_t^{α} refers to the α-order fractional time derivative. The variables in the model are $G(t)$ [mg/dL] is the blood glucose concentration, with the basal value G_b, $X(t)$ [1/min] is the dynamic insulin response, $I(t)$ [mU/L] is the blood insulin concentration, $m(t)$ [mg/min] is a glucose disturbance input (which can be the result of having a meal). The system input is the exogenous insulin rate $u(t)$ and the output is the blood glucose concentration $G(t)$.

The parameters of the minimal model are described in Table 1, with range values. The "nominal" values, used in the simulations done for this study are taken from [15]. Please note that, different sets of values (patient specific) can be found in literature [16], [18].

TABLE I. PARAMETERS OF THE INSULIN-GLUCOSE MODEL

Parameter	Description	Unit	Range Value	Nominal value
p_1	insulin-independent rate of glucose uptake in muscles	1/min	[0, 0.0375]	0.0337
p_2	rate for decrease in tissue of glucose uptake	1/min	[0.02, 0.025]	0.0209
p_3	insulin-dependent increase of tissue glucose uptake	L/(mU×min^2)	[6×10^{-5}, 13×10^{-6}]	7.51×10^{-6}
n	decay rate for insulin in blood	1/min	-	0.214
τ	insulin input conversion factor	1/L	-	1/12
G_b	basal level of glucose concentration	mg/dL	-	81

III. DESIGNING A FRACTIONAL-ORDER ADAPTIVE CONTROLLER

In type 1 diabetes mellitus, the pancreas does not produce insulin. In order to reduce the blood glucose levels, exogenous insulin has to be delivered through shots several times per day. An automatic insulin delivering device could significantly improve a patient's life.

Closed-loop systems for automatic deliver of insulin are presented in literature. In [15], [17] such system contains three elements: an implantable glucose sensor, a pump, and a control algorithm (see Fig. 1). The first and the second components have been studied and developed [17], [19], and reliable devices are already available. The most important part, still under intense study, remains the improvement the control algorithm. The controller has to compute the insulin deliver rate, such that the blood glucose would remain at the required level when glucose disturbance appears. In the same time, the system must avoid hypoglycemia.

Many control algorithms have been tested on the minimal model or on a linearized version of it: proportional-integrative-derivative, model predictive, fuzzy logic, sliding mode, H-inf and so forth. Good reviews are presented in [20-22].

The second objective in this paper is to design a fractional-order adaptive control system, for the nonlinear fractional-order insulin-glucose model. For that, we considered a modification of the original Model Reference Adaptive System (MRAS) scheme [11] in which the plant (insulin-to-glucose system) and the adjustment mechanism contain fractional derivatives. The scheme is depicted in Fig. 2. The control system contains two loops: an outer loop for adaptation and an inner loop for system stability.

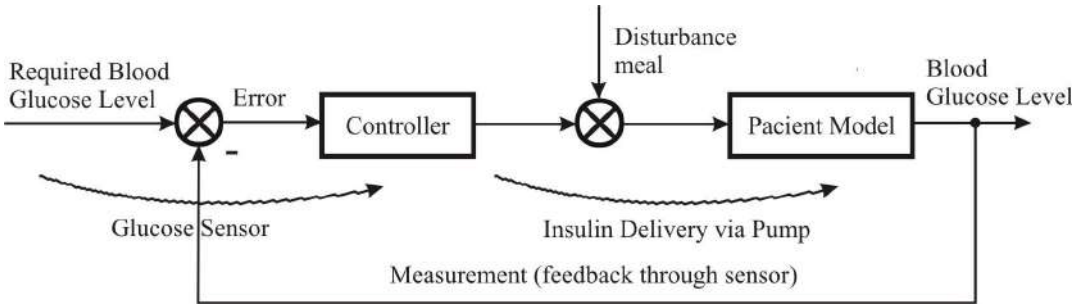

Fig. 1. Block diagram of the usual insulin–glucose closed loop systems.

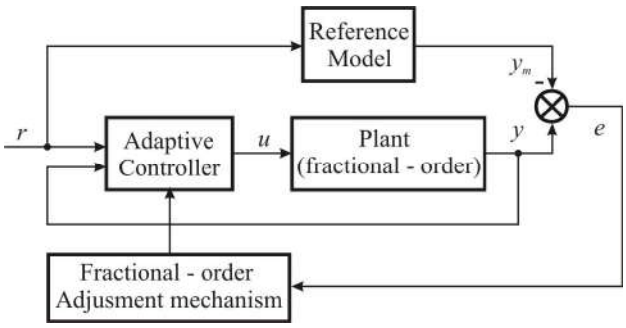

Fig. 2. Model reference adaptive system fractional-order scheme for the insulin-glucose model.

To determine the fractional adaptive control algorithm, we started from the MIT adjustment rule [11], considering the linear fractional-order insulin-glucose model. The conventional linearization about an operating point is applied on the first equation in (1), as in [15] or [23], which leads to:

$$D_t^{\alpha} G(t) = -p_1 G(t) - \overline{X} G(t) - \overline{G} X(t) + \\ + \overline{X}\,\overline{G} + p_1 G_b + m(t) \tag{2}$$

with $\overline{G}$ and $\overline{X}$ defining the operating point. Further, the constant term $\overline{X}\,\overline{G} + p_1 G_b$ is neglected based on the reasoning presented in [23].

The linearized model can be expressed in the form of a fractional-order transfer function $G_p(s) = G(s)/U(s)$, which is further used to determine the controller's parameters adaptation rule in adaptive control. Please note that the Laplace transform of a fractional-order derivative of a time variable is $\mathscr{L}\{D_t^{\alpha} y(t)\} = s^{\alpha} Y(s)$.

When applying fractional calculus (more precisely the fractional derivatives) the new MIT adjustment rule is [10]:

$$\frac{\mathrm{d}^{\alpha}\theta}{\mathrm{d}t^{\alpha}} = -\gamma \frac{\partial J}{\partial \theta} = -\gamma e \frac{\partial e}{\partial \theta}, \tag{3}$$

where θ is an adjustable parameter of the adaptive controller, e is the difference between the actual output of the system and the output of the reference model, $e(t) = y(t) - y_m(t)$, γ is the adaptation gain, $\partial e/\partial\theta$ is the sensitivity derivative of the system, and α is the order of the fractional derivative.

The desired time response of the fractional-order control system is given by choosing a reference model. In this case, a simple first order reference model can be set, with 30 minutes constant time, which means that, when starting with a high value for the blood glucose concentration, the system should reduce it to basal value within two to four hours. So, the reference model is:

$$G_m(s) = \frac{Y_m(s)}{R(s)} = \frac{1}{1800s+1} = \frac{1}{Ts+1} \tag{4}$$

To closely follow the output of the reference model, when variations of model parameters are possible (see Table 1 for their ranges), the model of the adaptive controller may be as follows [11]:

$$u(t) = k_1 r(t) - k_2 y(t) - k_3 \dot{y}(t). \tag{5}$$

where k_1, k_2, k_3 are adjustable parameters. Having the control model, the new MIT rule is going to be applied on plant's transfer function $G_p(s)$:

$$\begin{aligned} Y(s) &= G_p(s)U(s) = \\ &= G_p(s)[k_1 R(s) - k_2 Y(s) - k_3 s Y(s)] \\ Y(s) &= \frac{G_p(s)k_1}{1 + G_p(s)k_2 + G_p(s)k_3 s} R(s) \\ y(t) &= \frac{G_p(t)k_1}{1 + G_p(t)k_2 + G_p(t)k_3 p} r(t), \end{aligned} \tag{6}$$

where p is the differential operator.

A very important component in the MIT mechanism is the error:

$$e(t) = \left(\frac{G_p(t)k_1}{1 + G_p(t)k_2 + G_p(t)k_3 p} - G_m(t) \right) r(t). \tag{7}$$

Next, we derive the sensitivity derivatives by taking the partial derivatives of the error taking into account the controller parameters:

$$\begin{aligned} \frac{\partial e(t)}{\partial k_1} &= \frac{G_p(t)}{1 + G_p(t)k_2 + G_p(t)k_3 p} r(t), \\ \frac{\partial e(t)}{\partial k_2} &= -\frac{G_p(t)}{1 + G_p(t)k_2 + G_p(t)k_3 p} y(t), \\ \frac{\partial e(t)}{\partial k_3} &= -\frac{G_p(t)}{1 + G_p(t)k_2 + G_p(t)k_3 p} \dot{y}(t). \end{aligned} \tag{8}$$

The sensitivity derivatives cannot be used in the form presented before, because the parameters in the plant's model are unknown (or at least uncertain in most cases). To avoid this issue, the next approximation is required:

$$1 + G_p(t)k_2 + G_p(t)k_3 p = Tp + 1. \tag{9}$$

Then, the controller's parameters adjustment rules will be:

$$\frac{\mathrm{d}^{\alpha 1}k_1(t)}{\mathrm{d}t} = -\gamma\left(\frac{1}{Tp+1}r(t)\right)e(t),$$

$$\frac{\mathrm{d}^{\alpha 1}k_2(t)}{\mathrm{d}t} = \gamma\left(\frac{1}{Tp+1}y(t)\right)e(t), \qquad (10)$$

$$\frac{\mathrm{d}^{\alpha 1}k_3(\mathrm{t})}{\mathrm{dt}} = \gamma\left(\frac{1}{Tp+1}py(t)\right)e(t).$$

where $G_p(t)$ from the denominator in (8) is introduced in the adaptation gain γ [11]. Applying the Laplace transform on the equations (10) results in:

$$k_1(s) = -\gamma\frac{1}{s^{\alpha 1}}\left(\frac{1}{Ts+1}R(s)\right)E(s),$$

$$k_2(s) = \gamma\frac{1}{s^{\alpha 1}}\left(\frac{1}{Ts+1}Y(s)\right)E(s), \qquad (11)$$

$$k_3(s) = \gamma\frac{1}{s^{\alpha 1}}\left(\frac{1}{Ts+1}sY(s)\right)E(s).$$

IV. Simulations and Results

To simulate and evaluate the control performance of the closed loop system, a Matlab-Simulink scheme and FOMCON toolbox were used.

For simulations, the nonlinear fractional-order insulin-glucose model in (1) is considered. (The linear one is used only to design the fractional-order adaptive controller.) The goal is to keep the glucose concentration level at safe values after having a meal. The disturbance input in this case is the time varying glucose absorption rate. We considered the model of the glucose absorption from [24]:

$$m(t) = \frac{D_g A_g t e^{(-t/t_{\max})}}{t_{\max}^2}, \qquad (12)$$

where D_g [g] is the quantity of carbohydrates in the meal (an uncertain value, but in many simulations this is 50-60 grams), $A_g = 0.8$ is a constant that refers to the fraction of absorbed glucose from a meal, and $t_{\max}$ is the time moment when the absorption is at its peak value, which usually is around 40 minutes from the meal start.

We supposed that the patient's initial blood glucose concentration is $G_b = 80$[mg/dL] and after a meal with $D_g = 60$g carbohydrates, this value will increase. (Note that the meal is taken at 60 min.) The solution proposed for the closed loop nonlinear fractional-order system reduces the glucose concentration to the initial value, G_b (see Fig. 3).

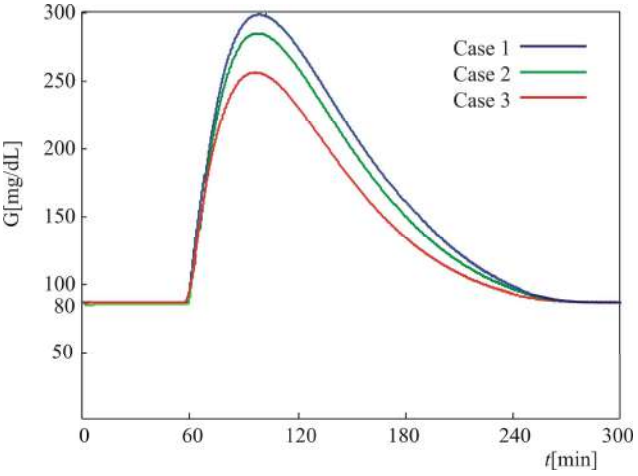

Fig. 3. Glucose concentration response

We considered three simulation scenarios, with different values of fractional derivative order α [18] (patient specific responses entail simulations with various values for α):

- case 1: $\alpha = 1$ and $\alpha 1 = 0.5$;
- case 2: $\alpha = 0.9$ and $\alpha 1 = 0.5$;
- case 3: $\alpha = 0.7$ and $\alpha 1 = 0.5$.

(Please note that α is the order of the fractional derivative in plant's model and $\alpha 1$ is the order of the fractional derivative in the adaptation rule for the controller parameters.)

As a remark, the simulations were done for the nominal values of the parameters using the same control low in all cases, with the adaptation gain $\gamma = 0.1$.

The system's response using the fractional-order adaptive controller applied on the nonlinear fractional-order insulin-glucose model, shows that the glucose value is reduced at the basal value within two to four hours and the blood glucose concentration will increase differently, even if the same quantity of carbohydrates are taken by all patients. Also, the benefits of the method proposed can be seen by analyzing the error signal (has to be reduced to zero, as seen in Fig. 4).

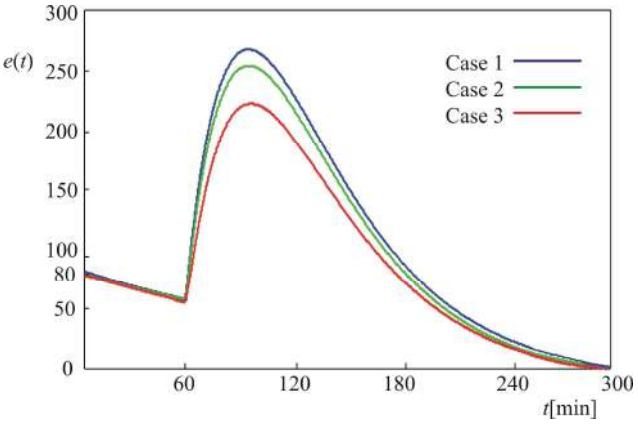

Fig. 4. The error variation

Next, using the same control low and keeping $\alpha = 0.7$, the insulin-glucose model parameters are changed as follows:

- $p_1 = 0.01$, $p_2 = 0.02$, $p_3 = 6 \times 10^{-5}$ (yellow);
- $p_1 = 0.03$, $p_2 = 0.021$, $p_3 = 2.5 \times 10^{-6}$ (magenta);
- $p_1 = 0.031$, $p_2 = 0.022$, $p_3 = 4.51 \times 10^{-6}$ (cyan);
- $p_1 = 0.032$, $p_2 = 0.023$, $p_3 = 6.51 \times 10^{-6}$ (red);
- $p_1 = 0.034$, $p_2 = 0.023$, $p_3 = 8.5 \times 10^{-6}$ (green);
- $p_1 = 0.0375$, $p_2 = 0.025$, $p_3 = 13.5 \times 10^{-6}$ (blue);

The time responses of the glucose concentration for each case are presented in Fig. 5, and the error variations in Fig. 6.

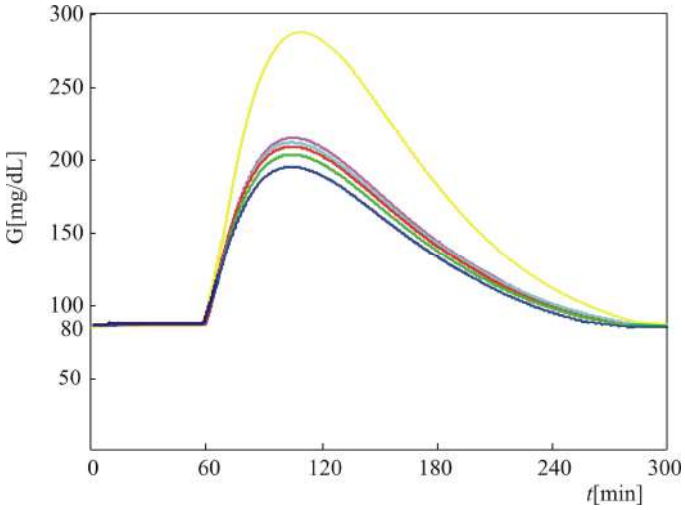

Fig. 5. Glucose concentration responses for different sets of values for the parameters p_1, p_2, p_3.

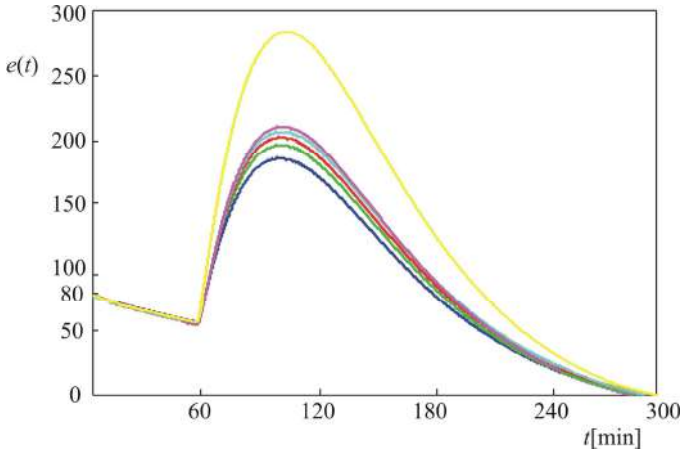

Fig. 6. The error time variation for different sets of values for the parameters p_1, p_2, p_3.

Comparing the glucose concentration responses to the nominal case, it can be concluded that using the same control low, in all cases, the glucose concentration achieve the basal level within the desired time range and the error is reduced to zero as expected.

V. Conclusions

For type 1 diabetes mellitus patients, a device that is able to automatically deliver insulin based on measured values of glucose concentration is significantly improving life. However, such device should work efficiently for different patients or situations. Besides acting in a reasonable time frame to reduce glucose concentration from high values (when already reached) to safety, such an automatic device should always avoid hypoglycemia states. In control engineering, these two basic requirements translate into settling time and no overshoot.

To obtain such operating mode for different parameters of the insulin-glucose dynamics, an adaptive control algorithm could be implemented. In this context, a new approach on how to control the insulin-glucose system using closed loop control is presented in this paper. We proposed a fractional-order adaptive controller which adjusts its parameters in relation to a fractional-order model of the insulin-glucose dynamics. The new model is derived from the well-known minimal model, by replacing the integer derivatives with fractional ones. The new model additionally catches patient specific response by adding a new parameter: the order of the fractional-derivatives.

Simulations prove that the desired time frame to reduce glucose concentration is reached for different virtual patients (different sets of parameters), without getting hypoglycemia.

A future work on the subject could be the design of a fractional-order adaptive controller based on Lyapunov stability.

Acknowledgment

We hereby acknowledge the structural founds project PRO-DD (POS-CCE, 0.2.2.1., ID 123, SMIS 2637, ctr. No. 11/2009) for providing the infrastructure used in this work.

References

[1] A. Oustaloup, La Dérivation non Entière: Theorie, Synthèse, et Applications, Hermes, Paris, 1995.

[2] I. Podlubny, Fractional-Order Systems and Fractional-Order Controllers, Inst. Exp. Phys., Slovak Acad. Sci., UEF-03-94, Kosice, 1994.

[3] Y. Chen, I. Petras, and D. Xue, "Fractional Order Control. A tutorial," American Control Conference, Hyatt Regency Riverfront, St. Louis, MO, USA, June 10-12, 2009, pp.1397-1411.

[4] S. Das, I. Pan, Fractional Order Signal Processing. Introductory Concepts and Applications, Springer, 2012.

[5] I. Podlubny, "Fractional-order systems and PIλDμ-controllers," IEEE Transactions on Automatic Control, Vol. 44, No. 1, 1999, pp. 208–214.

[6] C.A. Monje, Y.Q. Chen, B.M. Vinagre, D. Xue, and V. Feliu-Batlle, "Fractional-order Systems and Controls. Fundamentals and Applications," Advances in Industrial Control series, Springer-Verlag London, 2010.

[7] I. Petras, Fractional-Order Nonlinear Systems. Modeling, Analysis and Simulation, Ed. Springer, 2011.

[8] Y. Bensafia, and S. Ladaci, "Adaptive Control with Fractional Order Reference Model," International Journal of Science and Techniques of Automatic Control and Computer Engineering IJ-STA, Vol. 5, No.2, 2011, pp. 1614-1623.

[9] Z. Li, Fractional order modeling and control of multi–input–multi–output processes, Disertation Paper, University of California, 2015.

[10] B.M. Vinagre, I. Petras, and Y. Chen, "Using Fractional Order Adjustment Rules and Fractional Order Reference Models in Model-Reference Adaptive Control," Nonlinear Dynamics, 2002, pp. 269-279.

[11] K. Astrom, and B. Wittenmark, Adaptive Control, USA, Courier-Dover, 2008.

[12] P. Palumbo, S. Ditlevsen, A. Bertuzzi, and A. DeGaetano, "Mathematical modeling of the glucose–insulin system: A review," Mathematical Biosciences, Vol. 244, Issue 2, Aug. 2013, p. 69–81.

[13] R.N. Bergman, L.S. Phillips, and C. Cobelli, "Physiologic evaluation of factors controlling glucose tolerance in man. Measurement of insulin sensitivity and β-cell glucose sensitivity from the response to intravenous glucose," Journal of Clinical Investigations, Vol. 68, Dec. 1981, pp. 1456–1467.

[14] C. Cobelli, G. Toffolo, and E. Ferrannini, "A model of glucose kinetics and their control by insulin, compartmental and noncompartmental approaches," Mathematical Biosciences, Vol. 72, Dec. 1984, pp. 291-315.

[15] J. Chen, K. Cao, Y. Sun, Y. Xiao, and X.K. Su, "Continuous Drug Infusion for Diabetes Therapy: A Closed Loop Control System Design," EURASIP Journal on Wireless Communications and Networking, Vol. 2008, Article ID 495185, 2008, pp. 1-10.

[16] P. Kaveh and Y. Shtessel, "High Order Sliding Mode Control for Blood Control Regulation," Proc. of the 2006 Int. Workshop on Variable Structure Systems, Italy, 2006, pp.11-16.

[17] R. Nimri, and M. Phillip, "Artificial pancreas: fuzzy logic and control of glycemia," Current Opinion in Endocrinology, Diabetes, and Obesity, Vol. 21 (4), Aug. 2014, p. 251-256.

[18] I. N'Doye, H. Voos, M. Darouach, J. Schneider, "Static Output Feedback H-inf Control for a Fractional-Order Glucose-Insuline System," International Journal of Control, Automation and Systems, 2015, pp. 798-807.

[19] M. Owren, Automatic Blood Glucose Control in Diabetes, Master Thesis at Norwegian University of Science and Technology, 2009.

[20] J. Youssef, J. Castle, and W. Ward, "A Review of Closed-Loop Algorithms for Glycemic Control in the Treatment of Type 1 Diabetes," Algorithms, 2009, pp. 518-532.

[21] K. Lunze, T. Singh, M. Waltera, M.D. Brendelc, and S. Leonhardt, "Blood glucose control algorithms for type-1 diabetic patients: a methodological review, " Biomedical Signal Processing and Control, Vol. 8 (2), Mar. 2013, pp. 107-119.

[22] F.J. Doyle, L.M. Huyett, J.B. Lee, H.C. Zisser, and E. Dassau, "Closed-Loop Artificial Pancreas Systems: Engineering the Algorithms," Diabetes Care. Vol. 37, May 2014, pp. 1191-1197.

[23] F. Chee, A.V. Savkin, T.L. Fernando, and S. Nahavandi, "Optimal H-inf Insulin Injection Control for Blood Glucose Regulation in Diabetic Patients," IEEE Trans. on Biomed. Eng., vol. 52, no. 10, Oct. 2005, pp. 1625-1631.

[24] R. Hovorka, et al, "Nonlinear model predictive control of glucose concentration in subjects with type 1 diabetes," In Physiological Measure-ment, Vol. 25, 2004, pp. 905-920.

Documents

Export Date: 19 Jan 2018

Search: TITLE-ABS-KEY(Fractional Adaptive Control for a Fractional -...

1) Coman, S., Boldisor, C., Floroian, L.

Fractional adaptive control for a fractional - Order insuline - Glucose dynamic model

(2017) Proceedings - 2017 International Conference on Optimization of Electrical and Electronic Equipment, OPTIM 2017 and 2017 Intl Aegean Conference on Electrical Machines and Power Electronics, ACEMP 2017, art. no. 7975082, pp. 887-892.

DOI: 10.1109/OPTIM.2017.7975082

Document Type: Conference Paper

Source: Scopus

Search: TITLE-ABS-KEY(Fractional Adaptive Control for a Fractional - Order Insulin - Glucose Dynamic Model)

Copyright © 2018 Elsevier B.V. All rights reserved. Scopus® is a registered trademark of Elsevier B.V. RELX Group™

Applied Surface Science 417 (2017) 224–233

Contents lists available at ScienceDirect

Applied Surface Science

journal homepage: www.elsevier.com/locate/apsusc

Antimicrobial thin films based on ayurvedic plants extracts embedded in a bioactive glass matrix

L. Floroian[a], C. Ristoscu[b,*], G. Candiani[c], N. Pastori[c], M. Moscatelli[c], N. Mihailescu[b], I. Negut[b,d], M. Badea[e], M. Gilca[f], R. Chiesa[c], I.N. Mihailescu[b]

[a] Automation Department, Faculty of Electrical Engineering and Computer Science, Transilvania University of Brasov, 29 Eroilor Blvd, 500036, Brasov, Romania
[b] National Institute for Lasers, Plasma and Radiation Physics, 409 Atomistilor street, Măgurele, Ilfov, 077125, Romania
[c] Department of Chemistry, Materials and Chemical Engineering "Giulio Natta", Politecnico di Milano, Via Mancinelli 7, 20131, Milano, Italy
[d] Faculty of Physics, University of Bucharest, 077125 Magurele-Ilfov, Romania
[e] Fundamental, Prophylactic and Clinical Specialties Department, Faculty of Medicine, Transilvania University of Brasov, 29 Eroilor Blvd, 500036, Brasov, Romania
[f] Biochemistry Department, Faculty of General Medicine, "Carol Davila" University of Medicine and Pharmaceutics, 8 Eroilor Sanitari Blvd, 50471, Bucharest, Romania

ARTICLE INFO

Article history:
Received 14 November 2016
Received in revised form 3 February 2017
Accepted 21 February 2017
Available online 27 February 2017

Keywords:
Ayurvedic plants extracts
Matrix-assisted pulsed laser evaporation
Antimicrobial layers
Bioactive glass

ABSTRACT

Ayurvedic medicine is one of the oldest medical systems. It is an example of a coherent traditional system which has a time-tested and precise algorithm for medicinal plant selection, based on several ethnopharmacophore descriptors which knowledge endows the user to adequately choose the optimal plant for the treatment of certain pathology.

This work aims for linking traditional knowledge with biomedical science by using traditional ayurvedic plants extracts with antimicrobial effect in form of thin films for implant protection. We report on the transfer of novel composites from bioactive glass mixed with antimicrobial plants extracts and polymer by matrix-assisted pulsed laser evaporation into uniform thin layers onto stainless steel implant-like surfaces. The comprehensive characterization of the deposited films was performed by complementary analyses: Fourier transformed infrared spectroscopy, glow discharge optical emission spectroscopy, scanning electron microscopy, atomic force microscopy, electrochemical impedance spectroscopy, UV–VIS absorption spectroscopy and antimicrobial tests. The results emphasize upon the multifunctionality of these coatings which allow to halt the leakage of metal and metal oxides into the biological fluids and eventually to inner organs (by polymer use), to speed up the osseointegration (due to the bioactive glass use), to exert antimicrobial effects (by ayurvedic plants extracts use) and to decrease the implant price (by cheaper stainless steel use).

© 2017 Elsevier B.V. All rights reserved.

1. Introduction

Planktonic bacteria have the inherent ability to adhere to surfaces and stick on them, protected within an extracellular matrix or slime, to give rise to a structure called biofilm. Thus, the biofilm formation represents an adaptive process that enables microorganisms to survive in severely harsh conditions.

A significant step in the implant-related infections prophylaxis is represented by antibiotic therapy, but the choice of antibiotic, the application form and the time points for their administration still remain frequently debated issues in orthopedic surgery [1–4]. The need for bone efficient antibiotics, such as aminoglycosides, is in contrast to their severe toxicity when applied systemically. In view of these toxic side effects, effective local drug levels can hardly be achieved at the target site.

Plant products, with the least side effects, are more and more explored for their capacity to prevent biofilm formation and/or eradicate it [5]. The incorporation of bio-friendly phytochemicals or medicinal plant extracts into thin films represents a new treatment paradigm for the dental or bone implant protection. The potential clinical benefits would be significant, including reduced risk for revision surgery, preventing surgical site infection, accelerated implant osseointegration and decreased healthcare costs.

Curcuma longa (fam. Zingiberaceae), popularly called turmeric, is an Indian yellow-colored spice that has been used for millennia

* Corresponding author.

http://dx.doi.org/10.1016/j.apsusc.2017.02.197
0169-4332/© 2017 Elsevier B.V. All rights reserved.

to treat a variety of skin, pulmonary, gastrointestinal, or hepatic disorders and wounds. Studies show that turmeric may help fight cancer, infections and reduce inflammation [6–8]. Turmeric extracts showed antibacterial activity and produced significant inhibition of biofilm formation in case of bacteria isolated from dental plaques exhibiting resistance against antibiotics, with minimum inhibitory concentrations (MIC) of 2.5–10 mg/mL [9]. Another report showed that *C. longa* is effective against most of the isolated anaerobic bacteria from infected primary teeth [10].

Curcumin is the main bioactive phytochemical extracted from turmeric and belongs to the polyphenol class. It has a significant antibacterial and antifungal action [11,12]. Studies on the effects of curcumin on periodontopathic bacteria are promising. Curcumin suppressed almost completely the growth of *Porphyromonas gingivalis, Prevotella intermedia, Fusobacterium nucleatum* and *Treponema denticola*, although it was ineffective against of *Aggregatibacter actinomycetemcomitans* [13]. The compound was able to alter architecture of mature multi-species biofilms, as well as to significantly reduce the biofilm metabolic activity [14]. Besides, curcumin can promote osteogenic differentiation of mesenchimal stem cells [15], potentially contributing to implant osseointegration. It also displays a potent anti-inflammatory activity [16].

In the same time, organic compounds with heteroatoms such as oxygen, nitrogen, sulfur and phosphorus are the most reported inhibitors for the metal corrosion. Organic inhibitors act by the adsorption on the metal surface to form a protective layer that decreases the corrosion rate [17–19]. In this regard, curcumin (1,7- bis(4-Hydroxy-3-metoxyphenl)-1,6-heptadiene-3,5-dione) is an environmentally friendly corrosion inhibitors [20,21].

Ocimum sanctum (fam. Lamiaceae), known as "tulsi" in Hindi and "holy basil" in English, is as an important medicinal plant in ayurveda traditionally used for treatment of various ailments, including infections. Different parts of the plant have shown antimicrobial, anti-inflammatory, analgesic, antipyretic, immunomodulatory, adaptogen, antidiabetic, antioxidant and anticancer activities/properties [22,23]. The essential oil extracted from tulsi is rich in eugenol, a phenolic compound to which is attributed its antimicrobial activity [24]. Extracts from the leaves of *O. sanctum* have been found to inhibit the growth of several pathogens involved in common infections, such as *Mycobacterium tuberculosis, Staphylococcus aureus, Pseudomonas aeruginosa, Escherichia coli, Salmonella typhi* and *typhimurium, Bacillus cereus, Bacillus subtilis* and *Streptococcus pyogenes* [25–27].

The plant therapeutic potential in dental infections is already explored [28–31]. *O. sanctum* leaf extract displayed antimicrobial activity against microorganisms responsible for dental caries, pulpal and periapical diseases (*Streptococcus mutans, Streptococcus mitis, Streptococcus sanguis, Lactobacillus acidophilus, Actinobacillus actinomycetemcomitans*) [28–30]. Moreover, in Ref. [31] it was demonstrated that a similar extract was efficient at a very low concentration (5 mg/mL) in destroying the *Enterococcus faecalis* biofilm. Beyond its antimicrobial activity, *O. sanctum* has also wound and mandibular fracture healing properties [32,33], that are potentially useful for dental implant surgery.

Herewith, we propose an advanced nanostructure with synergetic properties, which combines several materials: bioactive glass (with osseointegrating properties), ayurvedic plants extracts of turmeric or tulsi (nontoxic, antibacterial agent and corrosion inhibitor) and poly(methyl methacrylate) (PMMA) (for anticorrosive protection), all deposited onto stainless steel implant type substrates. This structure was obtained by matrix-assisted pulsed laser evaporation (MAPLE), based on previous experience with achieving anticorrosive or antimicrobial composite thin films based on bioglass (BG) and PMMA [34–39].

2. Materials and methods

2.1. Materials and experiment

316L medical grade stainless steel (SS) Plates $1 \times 1\,cm^2$ were covered with protective nanostructures which contain bioactive glass (BG), ayurvedic extract and polymer (PMMA). SS substrates composition is: 64.26 wt% Fe, 18.51 wt% Cr, 12 wt% Ni, 2.13 wt% Mo, 1.44 wt% Mn, 0.58 wt% Cu, 0.56 wt% Si, 0.0265 wt% C, 0.0036 wt% S and smaller concentration of other elements. The SS plates were prepared prior to deposition, by mechanical processing (polishing to a roughness within μm range (Rq = 2–4 μm)), cleaning with acetone, ethanol and deionized water in an X-Tra 30 H ultrasonic bath.

A thin layer of PMMA on SS substrates was first deposited by MAPLE. PMMA $(C_5H_8O_2)_n$ is a linear thermoplastic biopolymer with a melting point of 160 °C and a glass transition temperature of 85 °C. PMMA has been widely used as a biomaterial both in medical applications and in some optical systems (contact lens as transmit light up to 93%) [40,41]. It also can be used as denture base material due to its proper properties, including well stability in the physiological environment, as ease of handling and repair [42]. Secondly, a thin layer consisting in BG + ayurvedic extract - turmeric (T) or holy basil (B) was deposited on PMMA/SS samples. The final samples were denoted BGT/PMMA/SS (with turmeric) and BGB/PMMA/SS (with basil).

The chosen BG has the best bioactivity and biocompatibility and contains 56.5% SiO_2, 15% CaO, 11% Na_2O, 8.5% MgO, 6% P_2O_5, 3% K_2O (in wt%). It is fabricated following the protocol described in Refs. [43,44]. ***Turmeric*** used in the experiments is commercially available in form of capsule which contains 1100 mg *C. longa* extract (standardized to 95% curcuminoids) and 5 mg *Piper Nigrum* (standardized to 95% piperine). Alike, the ***holy basil*** for the experiments is commercially available and a capsule contains 800 mg of leaves extract, standardized to 2% ursolic acid.

A matrix consisting in a solution of 0.6 g PMMA dissolved into 19.3 mL chloroform was used as a frozen target in MAPLE deposition of the first layer, according to a protocol described in Ref. [37]. MAPLE method is used in case of polymers and delicate substances because it faithfully replicates the properties and functionality of the starting materials, with no photochemical decomposition and damage under direct action of intense UV laser pulses [45–49]. 0.12 g BG and 800 mg T or B were dissolved then into 15 mL of deionized water and frozen in liquid nitrogen temperature in aim to deposit the second, top, layer.

All experiments were conducted using a KrF* ($\lambda = 248$ nm, $\tau_{FWHM} \leq 5$ ns) excimer laser source which was operated with 5 Hz repetition rate at fluence of $0.55\,J/cm^2$. For the growth of each thin film, 5000 subsequent laser pulses were applied. In order to obtain a uniform layer and to avoid drilling, the target and substrate were continuously rotated at 50 rpm, while the background pressure inside the deposition chamber was set at 2×10^{-2} mbar. Throughout the depositions, the target was kept at liquid nitrogen temperature using a cryogenic setting.

2.2. Methods for films characterization

Glow discharge optical emission spectroscopy (GDOES) analyses can provide information about chemical composition of the material, not only related to the surface but also in the depth. Relative intensity represented on *y*-axis is proportional with atomic concentration, so this is a quantitative method for composition's determination. GDOES studies were performed on all specimens using a Spectruma Analytik GMBH Hof, Germany) operated at 20 kV The investigations were performed in triplicate, on relatively large areas of $(250 \times 250)\,\mu m^2$.

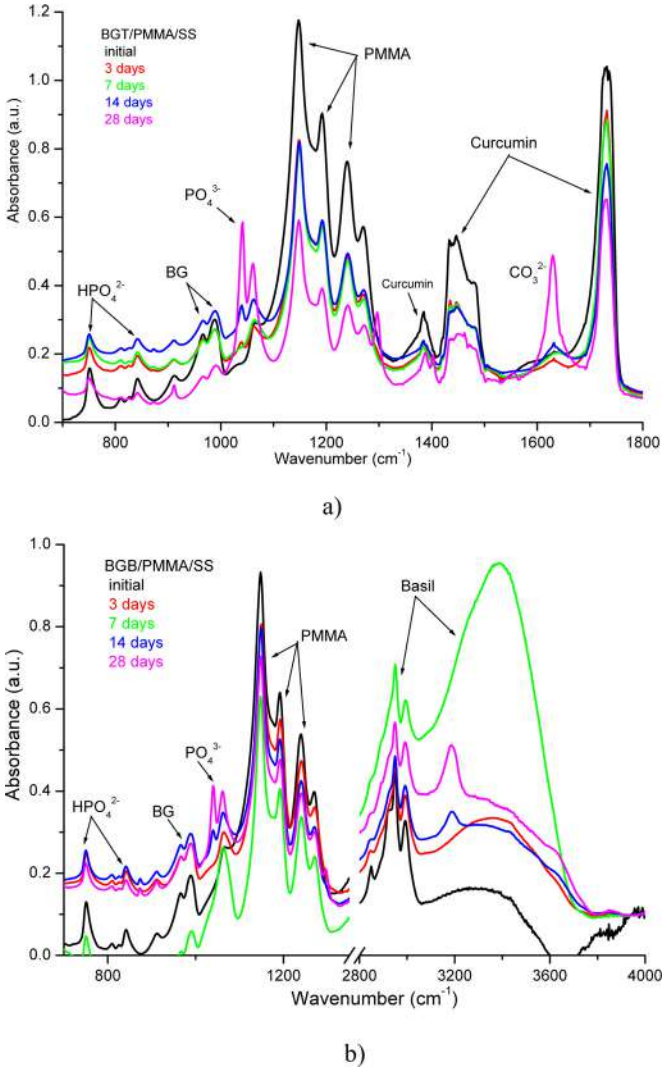

Fig. 1. FTIR spectra of BGT/PMMA/SS (a) and BGB/PMMA/SS (b) samples after different immersion time into SBF.

Molecular structure of the coatings was investigated by Fourier transformed infrared spectroscopy (FTIR). FTIR spectra were acquired in absorbance mode with a FTIR-8400S (Shimadzu Corp, Kyoto, Japan) which has operating range of 7800–350 cm^{-1}, spectral resolution of 0.4 cm^{-1} and S/N ratio of 20000:1. Uncovered control SS and covered SS with BGT/PMMA or BGB/PMMA thin films were immersed into 25 mL of simulated body fluid (SBF) [50] in polyethylene sterile containers and kept at 37 °C in a MMM Incucell microbiological incubator. After different immersion times their surface was investigated by FTIR. In the same time, SBF containing the products released of the samples was analyzed by UV–VIS absorption spectroscopy with a GBC Cintra10e UV–VIS–NIR spectrophotometer in 190–1200 nm range. All measurements were performed in triplicate, in accordance with the ISO/FDIS 23317:2007(E) Standard.

The morphological examination was carried out by scanning electron microscopy (SEM) using a Cambridge Stereoscan S360 electron microscope, operating at 15 kV acceleration voltages, in high vacuum, under secondary electron mode. The samples were scanned using a Workshop TT atomic force microscope (AFM) equipped with a 15 μm scanner. All images we recorded on a 15 μm by 15 μm area.

Electrochemical investigations were conducted using Palmsens potentiostat, controlled by PSTrace software, in a three electrodes configuration with Ag/AgCl reference electrode and platinum wire as counter electrode. Corrosion resistance in SBF of samples used as coatings for implants or prosthesis was assessed using high sensibility electrochemical methods: linear sweep voltammetry (LSV) and electrochemical impedance spectroscopy (EIS).

2.3. Evaluation of the antibacterial activity

The BGT/PMMA/SS (with turmeric) and BGB/PMMA/SS (with basil) samples were placed in 24-well polystyrene cell culture plates and sterilized for 30 min in pure ethanol prior to experiments. The antimicrobial activity of samples was tested according to Time Kill method by adapting and integrating the protocols described in ASTM E 2315 (Assessment of Antimicrobial Activity Using a Time-Kill Procedure) and ISO 22196 (Measurement of antibacterial activity on plastics and other non-porous surfaces) standards. Briefly, a small amount of stock bacteria (*E. coli* JM109, ATCC 25922 and *S. aureus*, ATCC 29213, LTA S.R.L. Milano, Italy) was transferred from glycerol stock to a sterile Luria broth (LB) Agar plate (20 g/L of LB base – Invitrogen, Thermo Fisher Scientific, Monza, Italy – and 15 g/L of Agar (Invitrogen) in distilled water – dH_2O) using a sterile plastic loop and incubated at 37 °C for 20 h.

The day before experimentation, one single colony of bacteria was picked from the LBA plate and suspended in 5 mL of LB in a sterile 50 mL polypropylene test tube and incubated overnight (ON) at 37 °C under shaking at 140 rpm. The day of the experiment, the inoculum was prepared diluting the bacteria to a starting OD_{600} = 0.02 in LB and bacteria were let grow until reaching OD_{600} ≈ 0.25–0.35 that corresponds to ≈ 1×10^8 CFU/mL. Next, 500 μL of bacteria suspension was diluted 1:50 in sterile dH_2O to a final concentration ≈ $1–2 \times 10^6$/mL and inoculated on the surface of each sample. Samples were then incubated in the darkness at 37 °C in a humidified incubator for 24 h. After 24 h, an aliquot from each sample was taken and serially diluted in sterile dH_2O. 50 μL were next plated on P60 LB Agar plates by means of the glass beads method. Colony forming units (CFU) were finally counted after ON incubation at 37 °C.

3. Results and discussion

To simulate prosthesis introduction in human body and to study the phenomena appearing at the implant–tissue interface and behavior of implant as result of interaction with physiological fluids, the samples of BGT/PMMA/SS and BGB/PMMA/SS were immersed into 25 mL SBF at 37° C and investigated after 1, 2, 3, 7, 14, 21 days soaking.

3.1. Physical–chemical characterization of deposited thin films

3.1.1. Chemical composition

To get information from samples surface modifications as a consequence of mutual interaction between samples and SBF, spectroscopic (FTIR and GDOES) and microscopic (SEM, AFM) analyses were conducted both on BGT/PMMA/SS and BGB/PMMA/SS initial samples and after different immersion time.

FTIR spectrum of as deposited BGT/PMMA/SS (Fig. 1a) reveals characteristic peaks of BG (966 and 988 cm^{-1}), curcumin (1384, 1440, 1490 and 1730 cm^{-1}) and PMMA (1114–1280 cm^{-1}). For turmeric, the strong peak at 1730 cm^{-1} was due to C=O adsorption, the one at 1384 cm^{-1} to aromatic C–O stretching, while the 1420 cm^{-1} peak was assigned to the characteristic CH_3 bending and 1490 cm^{-1} one to C=C vibrations [51,52]. The peaks of the PMMA can be also seen, though it is the under-layer, because BGT top-layer has an irregular structure. This kind of porous structure is especially designed for increasing the active surface and proportionally, the

sample biocompatibility. For implants, the surface's active morphology must be proper for cells adhesion and bone in-growth; moreover, the roughness must be suitable for a long term increased bone–implant interaction. Having control over these parameters (with mechanical and chemical etching over implant surface and/or by adding special morphological layers) one can guarantee a grown in biocompatibility up to 10 times [53,54].

When the samples are soaked into simulated body fluid, modifications in their FTIR spectra are expected. In the first days, the peaks associated to BG and curcumin are diminished. It means that their concentration is decreased because of BG dissolution accompanied by turmeric release. This is in complete agreement with our anterior studies on pure and nanocomposites containing BG, and also with literature [34–38,55].

On the second hand, as time of immersion went on, FTIR spectra exhibit new peaks, at 752 and 842 cm^{-1}, belonging HPO_4^{2-}, at 1040 and 1062 cm^{-1} belonging PO_4^{3-} and at 1630 cm^{-1} belonging CO_3^{2-}. Their presence proves the appearance of the hydroxyapatite (HA – $Ca_{10}(PO_4)_3(CO_3)_3(OH)_2$), the predominant mineral component of vertebrate bones, on the samples surface. This manifestation is expected knowing the BG behavior and it demonstrates the ability of the material to firmly bind to tissue via a bioactive fixation by a chemical bond at the bone–implant interface.

PMMA peaks decrease after several days of immersion, not because the self-decomposition, knowing that PMMA is a bioinert polymer, but because of the new HA layer that forms and starts to cover the entire surface and default PMMA, as demonstrated by EIS investigation.

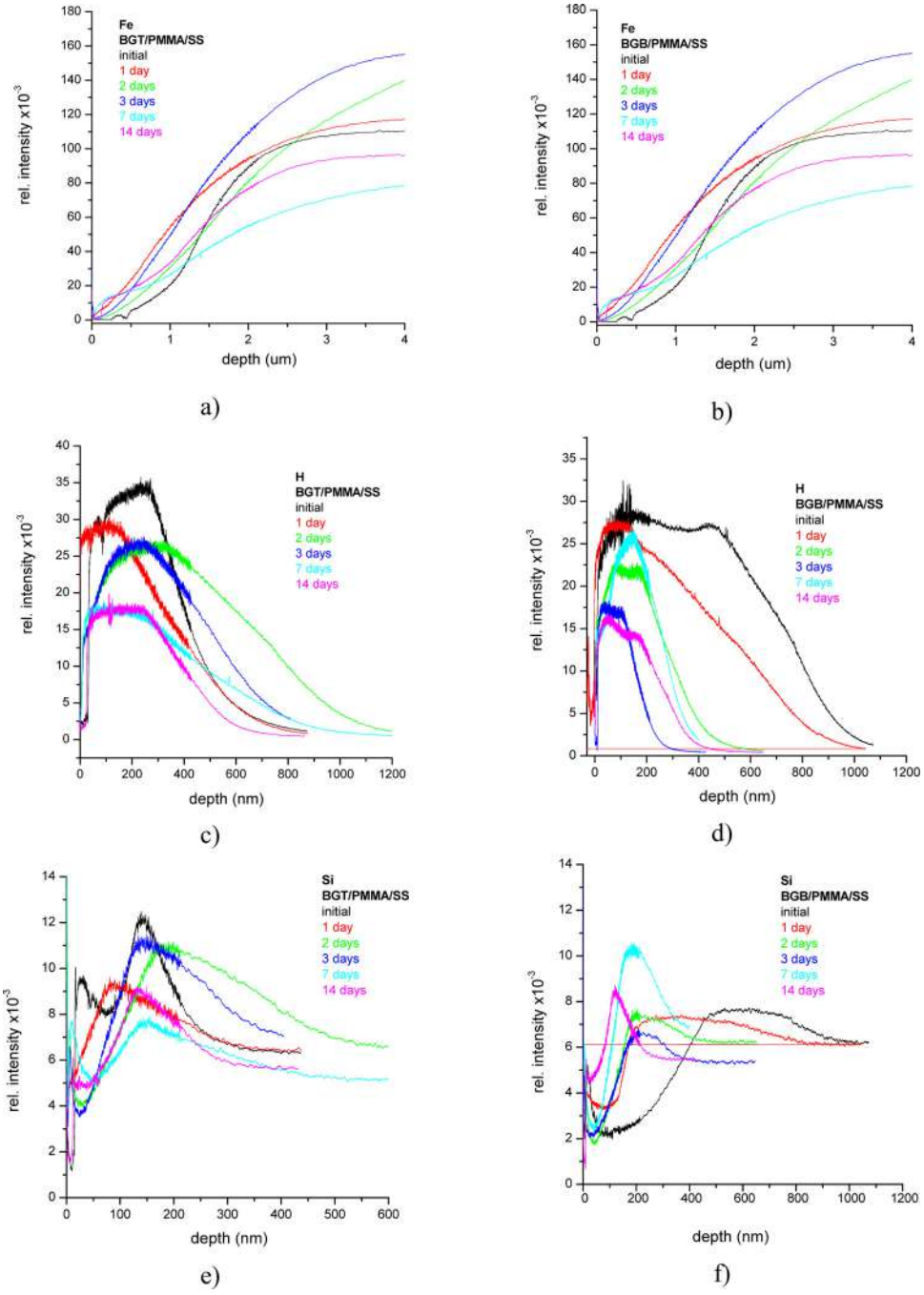

Fig. 2. Time evolution of the chemical elements from sample surface.

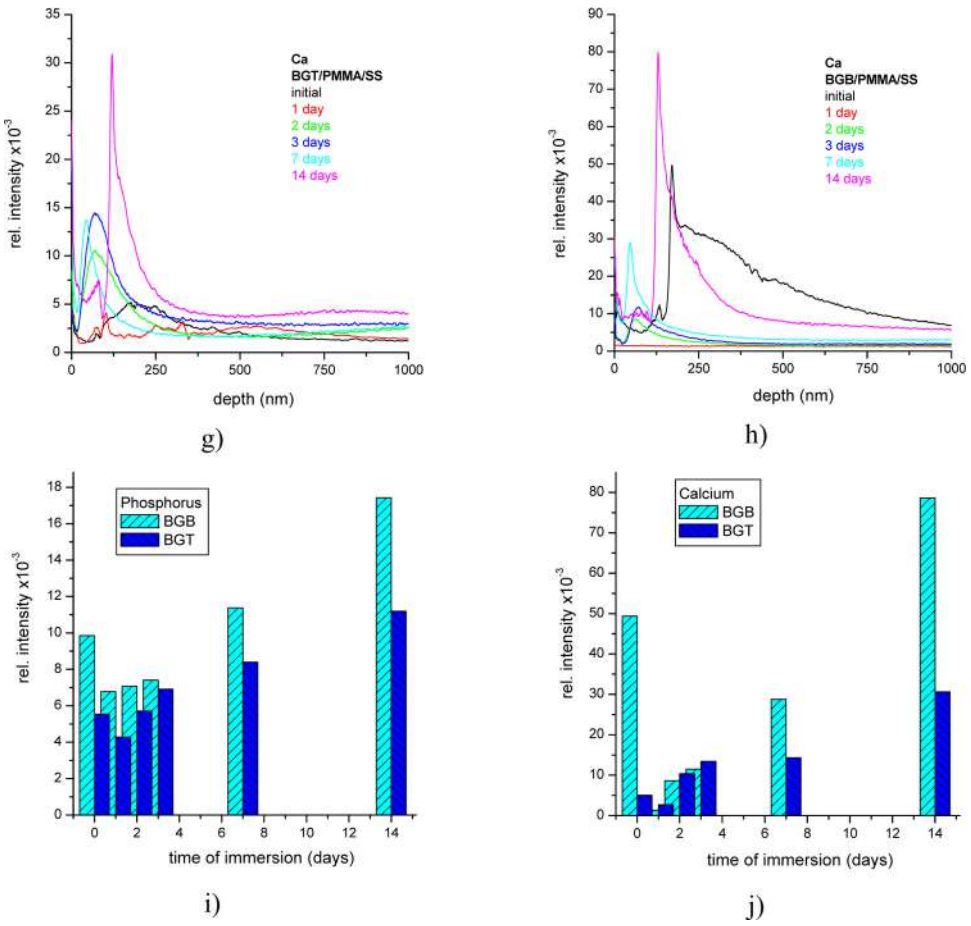

Fig. 2. (*Continued*)

In case of BGB/PMMA/SS samples, FTIR spectrum (Fig. 1b) of the initial surface (black) has peaks at 966 and 988 cm^{-1} belonging of BG, at 1114–1280 cm^{-1} that belong to PMMA and at 2946, 2989 and 3336 cm^{-1} belonging to basil. The FTIR spectrum of holy basil exhibited an absorption band at 3400–3620 cm^{-1}, which is attributed to the phenolic O–H stretching vibration [56]. From the inspection of the data in Fig. 1, a few observations are in order:

1) **PMMA**: PMMA content is decreasing from the first to the last day in all cases.
2) **BG**: BG signals slightly increase after 3 days of immersion in SBF in case of BGB/PMMA/SS but decrease for BGT/PMMA/SS samples. The BG suddenly decreases for BGB after 7 days but also visibly for BGT/PMMA/SS. The decreasing tendency is continued with some fluctuation for longer periods, up to 28 days.
3) **Ayurvedic extracts**: The curcumin concentration is continuously decreasing for BGT/PMMA/SS while basil content slightly increases after 3 days but faster after 7 days and fluctuating after this duration.
4) **Bioapatite (BHA):** A continuous increase is noticed for PO_4^{3-} peaks with slightly higher values for BGT/PMMA/SS. We mention that these lines correspond to the growth on films surface of a BHA layer containing carbonated calcium phosphate, with the very close composition to the human bone. The same process is active in both cases: BG is gradually released in SBF where is converted by ion exchange into BHA, which is then redeposited on samples surface [34–39]. This makes more difficult the observation of the signals originating from the undisolved components of the deposited mixture (ayurvedic extracts and PMMA). BG seems to be better bonded to basil than to curcumin, the most probably due to chemical reasons. That is why BG is more difficultly and slowly released from layers containing basil than from the ones with curcumin.

Fig. 2 shows the distribution of main elements into the depth of the investigated samples, one makes the following observations:

1. **Fe and others metallic atoms:** They can be traced deeper than 400–500 nm only. This means that these ions were not allowed to go to surface, but are efficiently shielded by the PMMA interlayer. One can estimate a thickness of ~400 nm for the double layer deposited onto stainless steel substrates. To our opinion, this is a convincing proof that the PMMA layer covering SS substrates prohibit the release of metallic ions into body fluids provoking inflammatory response, or even worse, accumulated in inner organs (liver, kidneys, spleen) with an increased risk of health problems [57–59].
2. **H, C, O, N**: They are present in all coatings, both before and after immersion (Figs. 2c–h). It is difficult to discriminate on their origin, from either surface (BGB or BGT) or intermediate (PMMA) layers. After immersion, H, C and O concentration drops and all peaks are shifted to left because the coating thickness decreases. One can suggest these changes are related to BG and probably small amount of turmeric and basil release and gradual interaction with SBF ions.
3. **Ca and Pa atoms**: The concentration of Ca (Fig. 2g, h, j) and P (Fig. 2i) on the surface significantly decreases in the first days of immersion due to BG dissolution One notices a small fluctuation in case of BGB after 7 days of immersion. Then, the concentration of the two elements increases, with

some differences for BGB and BGT, while its maximum moves deeper (~150 nm). This, the most probably means that the thickness of the BHA layer containing the two elements rapidly grows, and the samples get covered by a coating very similar to

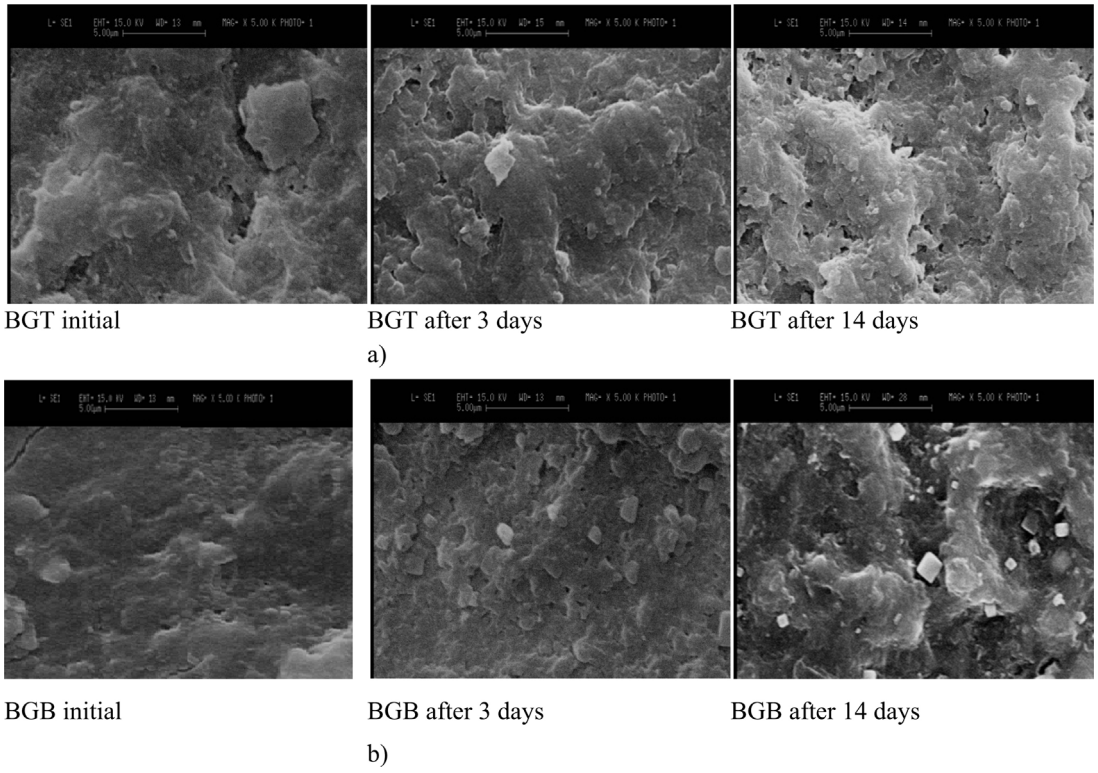

Fig. 3. SEM images of BGT/PMMA/SS (a) and BGB/PMMA/SS (b) surface before and after 3 and 14 days of immersion in SBF, 5000×.

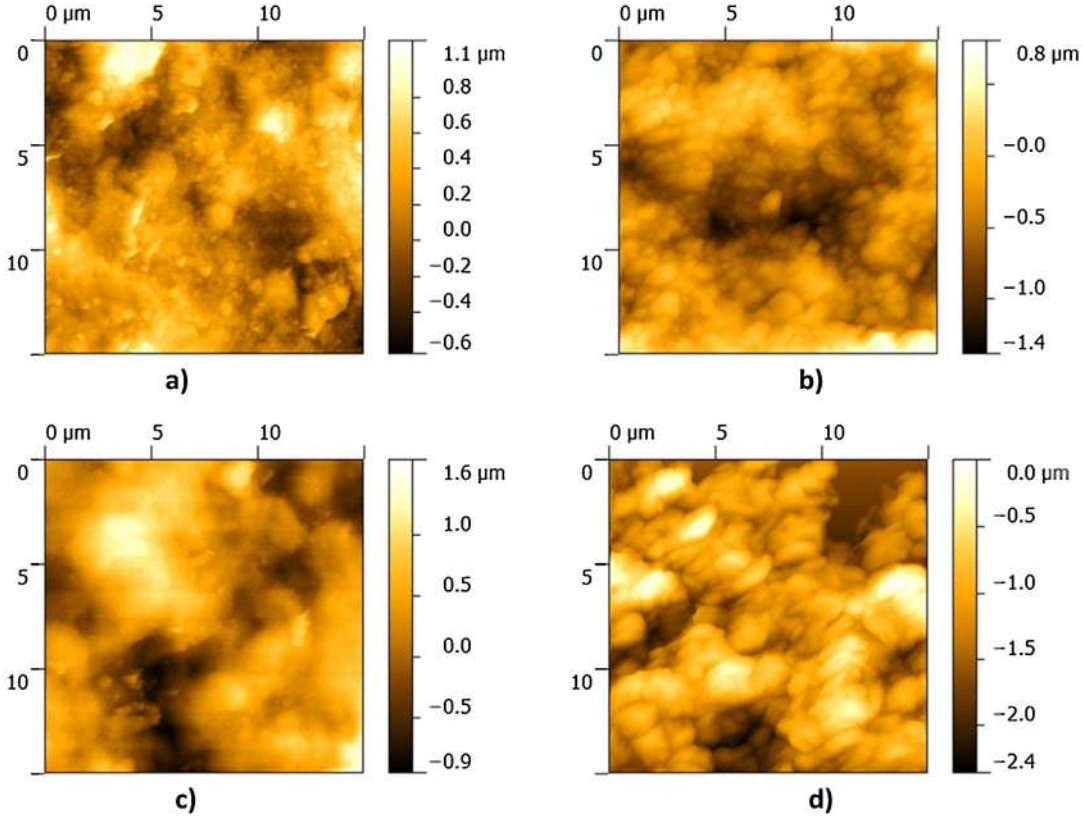

Fig. 4. AFM images of BGT/PMMA/SS and BGB/PMMA/SS samples before (a and c) and after 14 days of immersion in SBF (b and d).

Table 1
Roughness parameters for BGT/PMMA/SS and BGB/PMMA/SS samples before and after 14 days of immersion in SBF.

Sample	Time	Rrms (μm)	Ra (μm)
BGT/PMMA/SS	Initial	0.263	0.206
BGT/PMMA/SS	After 14 days	0.321	0.254
BGB/PMMA/SS	Initial	0.444	0.356
BGB/PMMA/SS	After 14 days	0.395	0.315

bone tissue having a thickness of (250–350) nm. This observation is congruent with FTIR study results (Fig. 1).

From Figs. 1 and 2 one may conclude that the synthesis of BHA is efficient for both combinations (BGB and BGT), while PMMA is strongly bonded and efficiently isolates the SS substrate, with predictable advantages for the development of a new generation of implants [60].

3.1.2. Surface morphology

The surface morphology of the BGT/PMMA/SS and BGB/PMMA/SS coatings before and at 3 or 14 days after immersion in SBF is illustrated in Fig. 3. Initial films consist of a dense and homogenous matrix with a lot of irregularities and pores which favors a good bone cells adherence, more accentuated for BGT/PMMA/SS. The film surface morphology is changing with soaking time in SBF. At 3 days, surfaces irregularities become more pronounced because of BG dissolution and release of ayurvedic drugs, in good accordance with FTIR and GDOES analyses. In the 14th day, the presence of BHA can be noticed, as uniform layer in case of BGT/PMMA/SS or as arbitrary scattered cubic particulates in micrometric range for BGB/PMMA/SS.

AFM study revealed an increase of BGT/PMMA/SS surface roughness after 14 days of immersion in SBF (compare Fig. 4a and b), and the relative roughness stability for BGB/PMMA/SS samples (see Fig. 4c) after the same time interval. The corresponding values (Rrms and Ra) are collected in Table 1.

3.2. Drug release evaluation

Another way to evaluate the release of the drugs is the UV–VIS spectroscopy of the SBF in which samples are submerged. The following protocol was applied: 2 mL of SBF was analyzed at every 2 h in the first two days, then once a day at the same hour in first week and next, once a week. The obtained spectra are shown in Fig. 5 where a prolonged release of the drug is evident. This can contribute to the inhibition of the bacterial attachment to the implant surface and prevention of the biofilm formation of which stays at the origin of microbial infection. The drug release several days after implantation can act upon the inflammatory reaction induced by crystallites which can be spread in surrounding tissue as a friction effect [61,62]. Inhibiting bacterial adhesion is a critical step toward preventing implant-associated infection, because bio-films are extremely resistant to both antibiotics and the immune system [63,64].

Fig. 5a shows us that turmeric release is maxim at 8 h after immersion, and then it is almost constant, while Fig. 5b evidences that for holy basil the maximum is reached after 23 days. At 30 days after immersion, releasing of the medicine still take place in both cases, with a consistent concentration comparable with the one of the first day.

3.3. Electrochemical study

LSV provides information on the influence of physiological fluids on SS bare substrates and both BGT/PMMA/SS and BGB/PMMA/SS,

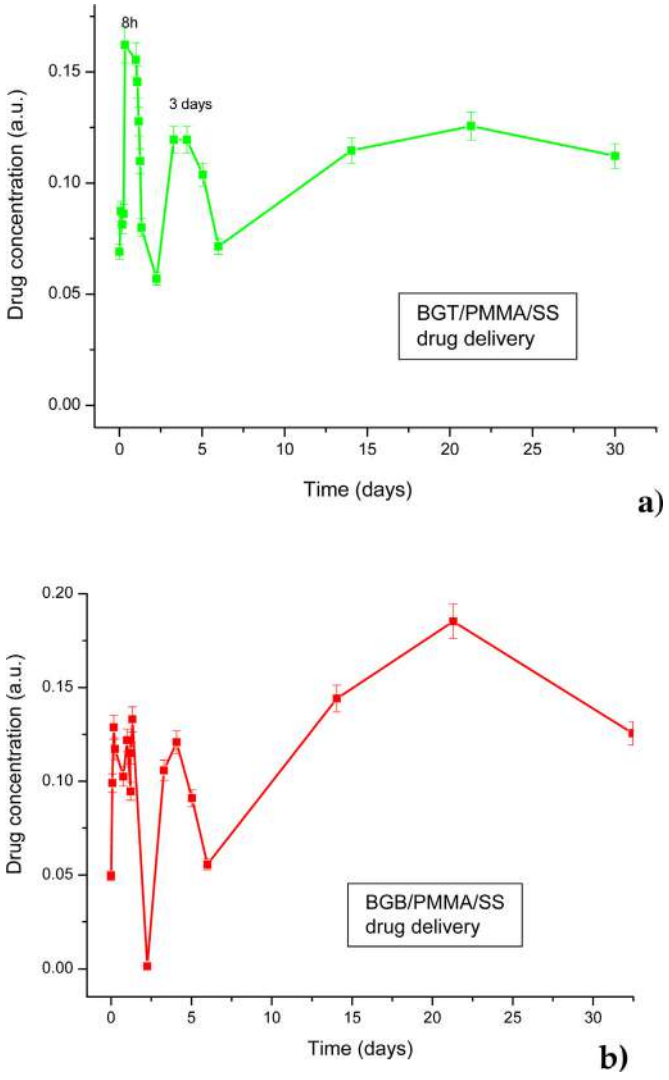

Fig. 5. Drug release from BGT/PMMA/SS (a) and BGB/PMMA/SS samples (b).

and also on corrosion mechanisms and rates. There is a linear relationship between the metal dissolution or corrosion rates, and the corrosion current (i_{corr}), and LSV can determine these important parameters. The measurements were performed in triplicate for each sample type, between −1.50 and −0.25 V, with a 0.1 V/s scan rate. The working electrodes have a square shape and 1 cm^2 active surface area. The mean values of corrosion parameters (corrosion potential (E_{corr}) and corrosion current (i_{corr})) were inferred.

BGB/PMMA/SS exhibits the best corrosion parameters (Table 2), the largest corrosion potential and the smallest corrosion current, which means these samples have a very good corrosion resistance. Conversely, stainless steel control undergoes a significant degradation process that worsens with time of immersion. Both BGT/PMMA/SS and BGB/PMMA/SS prove a good protection against corrosion in unfriendly environment, like physiological fluids. Corrosion currents and consequently the corrosion rates are very small due to inner layer of PMMA and to new apatite one that is formed through exchange of bioactive glass ions with SBF-ions during immersion.

In the same time, the processes which take place at film-electrolyte interface were characterized by EIS. A 0.01 V amplitude sinusoidal voltage perturbations was applied, scanned from 10000 to 0.1 Hz with 10 points per frequency decade and an auto-integration time 5 s, while the samples were immersed in SBF used

Table 2
Corrosion parameters of the samples and SS control.

Time of immersion in SBF	Corrosion potential E_{corr} (mV)			Corrosion current i_{corr} (μA/cm^2)		
	SS	BGT/PMMA/SS	BGB/PMMA/SS	SS	BGT/PMMA/SS	BGB/PMMA/SS
0 days	−849	−849	−549	8.11	2.14	0.89
1 day	−798	−948	−688	7.02	3.29	1.43
3 days	−848	−1048	−748	7.45	3.78	1.87
7 days	−848	−898	−721	8.84	1.65	2.04
14 days	−898	−824	−1004	6.48	1.23	3.45
21 days	−948	−703	−989	9.56	1.07	2.97

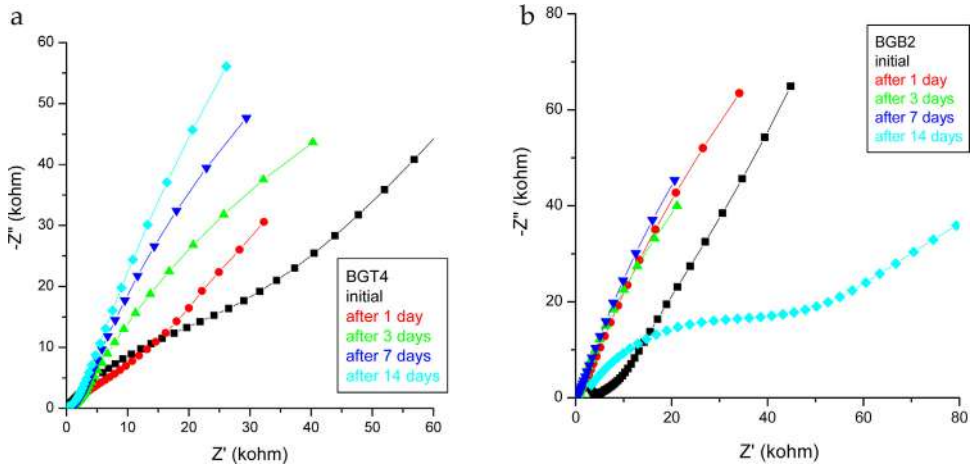

Fig. 6. Nyquist plots for BGT/PMMA/SS (a) and BGB/PMMA/SS (b).

Table 3
Antibacterial activity of BGT/PMMA/SS and BGB/PMMA/SS against *S. aureus* and *E. coli*.

Bacteria (CTRL)	Studied samples	Bacteria vs CTRL (% mean ± st. dev.)	Antibacterial efficiency (% vs CTRL)
S. aureus	BGT/PMMA/SS	5.3 ± 3.7	94.7
	BGB/PMMA/SS	9.7 ± 8.9	90.3
E. coli	BGT/PMMA/SS	44.2 ± 4.6	55.8
	BGB/PMMA/SS	49.5 ± 4.4	50.5

as electrolyte. Initial spectrum of BGT/PMMA/SS (Fig. 6a black) reveals two time constants and the maximum phase angles of 51° and 25° suggest that two processes take place simultaneously at sample–electrolyte interface: the BG dissolution in SBF and the adsorption of some electrolyte ions on surface, such as P, O, Ca. The same behavior is evident after 1 day of immersion in SBF, but the circle radius at high frequency is increasing, which means an amplification of polarization resistance of the superficial layer. These processes are ongoing after 3 days of immersion. After 7 days of immersion or more, single time constant process takes place due to complete dissolution of glass and suggests the capacitive behavior of PMMA layer. All the resistances are high, more than 40 kΩ, because of the presence of polymeric protective layer. It acts not only by isolating the metal from corrosive liquid, but also by introducing a very high electrical resistance between anodic and cathodic centers on the metal surface that are really isolated from each other. Accordingly, the corrosion current density is negligible. The radius of Nyquist circle increases in next days of immersion due to HA layer formed on the sample surface. The electrical resistance is larger, this layer being also an electrical insulator.

The same observations are valid for BGB/PMMA/SS electrochemical analyses, the sole difference being in timing. An important degradation of surface is visible in the 14th days after samples immersion into SBF, because of rapid release of holy basil around this day.

3.4. Biological assays

The antibacterial activity of BGT/PMMA/SS and BGB/PMMA/SS was evaluated over 24 h after incubation with *S. aureus* and *E. coli*. The antimicrobial activity of both samples was roughly the same, although much higher against Gram positive (*S. aureus*) than Gram negative (*E. coli*) bacteria. BGT/PMMA/SS and BGB/PMMA/SS displayed an antibacterial efficiency higher than 90% against *S. aureus* and higher than 50% against *E. coli*, as presented in Table 3. It is also worthy to note that BGT/PMMA/SS displayed a generally higher antibacterial activity as compared to BGB/PMMA/SS.

4. Conclusions

This study explored an innovative concept for thin films for implant covering with multiple advantages, based upon double layers of bioactive glass and antimicrobial plants extract/polymer deposited by matrix-assisted pulsed laser evaporation onto stainless steel substrate (implant like). One observes the bioactive glass dissolution resulting in the growth of a bioapatite layer (FTIR, GDOES and EIS analyses) on top of the polymeric interlayer with anticorrosive protection of the metallic substrate (LSV and GDOES investigations). SEM and AFM analyses evidenced a rogh morphology, proper for good cells adhesion, The most important achievement of our new concept is the antimicrobial effect due to

the inclusion of natural plant extract from ayurvedic medicine, with prolonged release and without adverse effects (UV–VIS, biological assay).

Even the behavior of BGB/PMMA/SS and BGT/PMMA/SS samples is different, both of them can be useful in implantology: if one needs a fast release of the drug, BGT/PMMA/SS coating of implant is recommended, when the dissolution of the bioactive glass is simultaneous with turmeric release, and if a slow release of the drug is the option, BGB/PMMA/SS coating of implant is recommended, when drug release is subsequent to bioglass dissolution.

One may conclude that the synthesized layers are multifunctional with a demonstrated bioactive action, antimicrobial effect and strongly shield against metal ions release from the stainless steel substrates to the body fluids.

Acknowledgments

LF and MB acknowledge the structural founds project PRO-DD (POS-CCE, O.2.2.1., ID 123, SMIS 2637, ctr. No 11/2009) and "Bursa universitatii 2016" and PN-III-P2-2.1-PED-2016-0621. NM, CR and IN acknowledge with thanks the support of UEFISCDI under the contract TE140/2015. LF and CR acknowledge UEFISCDI under the contract 146 PED/2017.

References

[1] M. Krasny, K. Krasny, M. Zadurska, P. Fiedor, Evaluation of treatment outcomes and clinical indications for antibiotic prophylaxis in patients undergoing implantation procedures, Adv. Med. Sci. 61 (2016) 113–116.
[2] J.A. Lindeboom, J.W. Frenken, J.G. Tuk, F.H. Kroon, A randomized prospective controlled trial of antibiotic prophylaxis in intraoral bone-grafting procedures: preoperative single-dose penicillin versus preoperative single-dose clindamycin, Int. J. Oral. Max. Surg. 35 (2006) 433–436.
[3] M. Jaeger, D. Maier, W. Kern, N.P. Sudkamp, Antibiotics in trauma and orthopaedic surgery – a primer of evidence-based recommendations, Injury 37 (2006) 74–80.
[4] M. Kuper, A. Rosenstein, Infection prevention in total knee and total hip arthroplasties, Am. J. Orthop. 37 (2008) 2–5.
[5] N. Venkateshbabu, S.A. Abarajithan, M.S.O. Sheriff, P.S. Jacob, N. Sonia, Natural therapeutic options in endodontics – a review, Open. Dent. J. 10 (2016) 214–226.
[6] B.B. Aggarwal, C. Sundaram, N. Malani, H. Ichikawa, Curcumin: the Indian solid gold, Adv. Exp. Med. Biol. 595 (2007) 1–75.
[7] S.C. Gupta, S. Patchva, B.B. Aggarwal, Therapeutic roles of curcumin: lessons learned from clinical trials, AAPS J. 15 (2013) 195–218.
[8] B.B. Aggarwal, W. Yuan, S. Li, S.C. Gupta, Curcumin-free turmeric exhibits anti-inflammatory and anticancer activities: identification of novel components of turmeric, Mol. Nutr. Food Res. 57 (2013) 1529–1542.
[9] S. Hayat, A.N. Sabri, Screening for antibiofilm and antioxidant potential of turmeric (*Curcuma longa*) extracts, Pak. J. Pharm. Sci. 29 (2016) 1163–1170.
[10] C. Martina, I. Corazzari, E. Prenesti, E. Bertone, E. Vernè, S. Ferraris, Bioactive glass coupling with natural polyphenols: Surface modification, bioactivity and anti-oxidant ability, Appl. Surf. Sci. 367 (2016) 237–248.
[11] A. Kali, D. Bhuvaneshwar, P.M.V. Charles, K.S. Seetha, Antibacterial synergy of curcumin with antibiotics against biofilm producing clinical bacterial isolates, J. basic Clin. Pharm. 7 (2016) 93–96.
[12] M. Shahzad, L. Sherry, R. Rajendran, C.A. Edwards, E. Combet, G. Ramage, Utilising polyphenols for the clinical management of Candida albicans biofilms, Int. J. Antimicrob. Agents. 44 (2014) 269–273.
[13] S. Izui, S. Sekine, K. Maeda, et al., Antibacterial activity of curcumin against periodontopathic bacteria, J. Periodontol. 87 (1) (2016) 83–90, 10.1902/jop.2015.150260.
[14] M. Shahzad, E. Millhouse, S. Culshaw, C.A. Edwards, G. Ramage, E. Combet, Selected dietary (poly)phenols inhibit periodontal pathogen growth and biofilm formation, Food Funct. 6 (2015) 719–729.
[15] Q. Gu, Y. Cai, C. Huang, Q. Shi, H. Yang, Curcumin increases rat mesenchymal stem cell osteoblast differentiation but inhibits adipocyte differentiation, Pharmacogn. Mag. 8 (2012) 202–208.
[16] J.S. Jurenka, Anti-inflammatory properties of curcumin, a major constituent of *Curcuma longa*: a review of preclinical and clinical research, Altern. Med. Rev. 14 (2009) 141–153.
[17] T. Ibrahim, H. Alayan, Y. Al Mowaqet, The effect of Thyme leaves extract on corrosion of mild steel in HCl, Prog. Org. Coat 75 (2012) 456–462.
[18] M. Behpour, S.M. Ghoreishi, M. Khayatkashani, N. Soltani, Green approach to corrosion inhibition of mild steel in two acidic solutions by the extract of Punica granatum peel and main constituents, Mater. Chem. Phys. 131 (2012) 621–633.
[19] M. Tourabi, K. Nohair, A. Nyassi, B. Hammouti, C. Jama, F. Bentiss, Thermodynamic characterization of metal dissolution and inhibitor adsorption processes in mild steel/3,5-bis(3,4-dimethoxyphenyl)-4-amino-1,2,4-triazole/hydrochloric acid system, J. Mater. Environ. Sci 5 (2014) 1133–1143.
[20] A.M. Al-Fakih, M. Aziz, H.M. Sirat, Turmeric and ginger as green inhibitors of mild steel corrosion in acidic medium, J. Mater. Environ. Sci. 6 (2015) 1480–1487.
[21] N.I. Kairi, J. Kassim, The effect of temperature on the corrosion inhibition of mild Steel in 1 M HCl Solution by *Curcuma longa* extract, Int. J. Electrochem. Sci. 8 (2013) 7138–7155.
[22] M.M. Cohen, Tulsi – *Ocimum sanctum*: a herb for all reasons, J. Ayurveda Integr. Med. 5 (2014) 251–259.
[23] N. Singh, M. Gilca, Tulsi – a potential protector against air travel health problems, Indian J. Nat. Prod. Resour. 7 (2008) 54–57.
[24] M.J. Saharkhiz, A.A. Kamyab, N.K. Kazerani, K. Zomorodian, K. Pakshir, M.J. Rahimi, Chemical compositions and antimicrobial activities of *Ocimum sanctum* L. Essential Oils at Different Harvest Stages, Jundishapur J. Microbiol. 8 (2015) e13720.
[25] B. Joshi, S. Lekhak, A. Sharma, Antibacterial property of different medicinal plants: *Ocimum sanctum*, Cinnamomum zeylanicum, Xanthoxylum armatum and Origanum majorana, Kathmandu University, J. Sci. Eng. Tech. 5 (2009) 143–150.
[26] S. Mishra, P. Mishra, Study of antibacterial activity of *Ocimum sanctum* extract against gram-positive and gram-negative bacteria, Am. J. Food. Technol. 6 (2011), 336–334.
[27] P. Goyal, P. Kaushik, In vitro evaluation of antibacterial activity of various crude leaf extracts of indian sacred plant, *Ocimum sanctum* L, Br. Microbiol. Res. J. 1 (2011) 70–78.
[28] P.R. Kochikar, S.S. Bhat, A. Salman, J. Chandra, Use of an extract of indian sacred plant ocimum sanctum as an anticariogenic agent: an in vitro study, Int. J. Clin. Pediatr. Dent. 8 (2015) 99–101.
[29] K.S. Mistry, Z. Sanghvi, G. Parmar, S. Shah, The antimicrobial activity of Azadirachta indica, Mimusops elengi, Tinospora cardifolia, *Ocimum sanctum* and 2% chlorhexidine gluconate on common endodontic pathogens: an in vitro study, Eur. J. Dent. 8 (2014) 172–177.
[30] P. Eswar, C.G. Devaraj, P. Agarwal, Anti-microbial activity of tulsi {*Ocimum sanctum* (Linn.)} extract on a periodontal pathogen in human dental plaque: an in vitro study, J. Clin. Diagn. Res. 10 (2016) ZC53–ZC56.
[31] A. Subbiya, K. Mahalakshmi, S. Pushpangadan, K. Padmavathy, P. Vivekanandan, V.G. Sukumaran, Antibacterial efficacy of Mangifera indica L. kernel and *Ocimum sanctum* L. leaves against Enterococcus faecalis dentinal biofilm, J. Conserv. Dent. 16 (2013) 454–457.
[32] A. Goel, S. Kumar, D.K. Singh, A.K. Bhatia, Wound healing potential of *Ocimum sanctum* Linn. with induction of tumor necrosis factor-alpha, Indian J. Exp. Biol. 48 (2010) 402–406.
[33] S. Mohammad, U.S. Pal, R. Pradhan, N. Singh, Herbal remedies for mandibular fracture healing, Natl. J. Maxillofac. Surg. 5 (2014) 35–38.
[34] L. Floroian, M. Florescu, G. Popescu-Pelin, C. Ristoscu, I.N. Mihailescu, Synthesis of biomaterial thin films by pulsed laser technologies: electrochemical evaluation of bioactive glass-based nanocomposites coatings for biomedical applications, Mater. Sci. Eng. C 32 (2012) 1152–1157.
[35] L. Floroian, F. Sima, M. Florescu, M. Badea, A.C. Popescu, N. Serban, I.N. Mihailescu, Double layered nanostructured composite coatings with bioactive silicate glass and polymethylmetacrylate for biomimetic implant applications, J. Electroanal. Chem. 64 (2010) 111–118.
[36] L. Floroian, I.N. Mihailescu, F. Sima, G. Stanciu, B. Savu, Evaluation of biocompatibility and bioactivity for polymethyl methacrylate – bioactive glass nanocomposite films obtained bymatrix assisted pulsed laser evaporation, U.P.B. Sci. Bull. A 72 (2010) 134–148.
[37] L. Floroian, C. Samoila, M. Badea, D. Munteanu, C. Ristoscu, F. Sima, I. Negut, M.C. Chifiriuc, I.N. Mihailescu, Stainless steel surface biofunctionalization with PMMA-bioglass coatings: compositional, electrochemical corrosion studies and microbiological assay, J, Mater. Sci.: Mater. Med. 26 (2015) 195–209.
[38] L. Floroian, B. Savu, G. Stanciu, A.C. Popescu, F. Sima, I.N. Mihailescu, R. Mustata, L.E. Sima, S.M. Petrescu, D. Tanaskovic, D. Janackovic, Nanostructured bioglass thin films synthetized by pulsed laser deposition: CLSM, Ftir investigations and in vitro biotests, Appl. Surf. Sci. 255 (2008) 3056–3065.
[39] L. Floroian, C. Ristoscu, N. Mihailescu, I. Negut, M. Badea, D. Ursutiu, M.C. Chifiriuc, I. Urzica, H.M. Dyia, C. Bleotu, N. Ion, Mihailescu, Functionalized antimicrobial composite thin films printing for stainless steel implant coatings, Molecules 21 (6) (2016) 740–758.
[40] D. Baxter, J. Yeh, The use of polymethyl methacrylate (PMMA) in neurosurgery, in: L. Ambrosio, E. Tanner (Eds.), Biomaterials for Spinal Surgery, Woodhead Publishing Limited, Cambridge, UK, 2012, pp. 365–384.
[41] L. Zhang, D. Wu, Y. Chen, X. Wang, G. Zhao, H. Wan, C. Huang, Surface modification of polymethyl methacrylate intraocular lenses by plasma for improvement of antithrombogenicity and transmittance, Appl. Surf. Sci. 255 (2009) 6840–6845.
[42] G.J. Owens, R.K. Singh, F.F. Alqaysi, Sol–gel based materials for biomedical applications, Prog. Mater. Sci. 77 (2016) 1–79.
[43] D. Tanaskovic, B. Jokic, G. Socol, A. Popescu, I.N. Mihailescu, R. Petrovic, Dj. Janackovic, Synthesis of functionally graded bioactive glass-apatite multistructures on Ti substrates by pulsed laser deposition, Appl. Surf. Sci. 254 (2007) 1279–1282.

[44] E. Gyorgy, S. Grigorescu, G. Socol, I.N. Mihailescu, D. Janackovic, A. Dindune, Z. Kanepe, E. Palcevskis, E.L. Zdrentu, S.M. Petrescu, Bioactive glass and hydroxyapatite thin films obtained by pulsed laser deposition, Appl. Surf. Sci. 253 (2007) 7981–7986.
[45] R.A. McGill, D.B. Chrisey, Method of producing a film coating by matrix assisted pulsed laser deposition. US Patent No. US 6025036 A, 2000.
[46] R. Cristescu, C. Popescu, G. Socol, A. Visan, I.N. Mihailescu, S.D. Gittard, P.R. Millerb, T.N. Martin, R.J. Narayan, A. Andronie, I. Stamatin, D.B. Chrisey, Deposition of antibacterial of poly(1,3-bis-(p-carboxyphenoxy propane)-co-(sebacic anhydride)) 20:80/gentamicin sulfate composite coatings by MAPLE, Appl. Surf. Sci. 257 (2011) 5287–5292.
[47] J. Schou, Fundamentals of laser-assisted fabrication of inorganic and organic films, in: I.N. Mihailescu, A. Vaseashta (Eds.), NATO Science for Peace and Security Series B: Physics and Biophysics, Functionalized Nanoscale Materials, Devices and Systems, Springer Science & Business Media, Dordrecht, Germany, 2008, pp. 241–256.
[48] A. Visan, D. Grossin, N. Stefan, L. Duta, F.M. Miroiu, G.E. Stan, M. Soprony, C. Luculescu, M. Freche, O. Marsan, C. Charvillat, S. Ciuca, I.N. Mihailescu, Biomimetic nanocrystalline apatitecoatings synthesized by Matrix Assisted Pulsed Laser Evaporation for medical applications, Mater. Sci. Eng., B 181 (2014) 56–63.
[49] R. Cristescu, C. Cojanu, A. Popescu, S. Grigorescu, L. Duta, G. Caraene, A. Ionescu, D. Mihaiescu, R. Albulescu, T. Buruiana, A. Andronie, I. Stamatin, I.N. Mihailescu, D.B. Chrisey, Functionalized polyvinyl alcohol derivatives thin films for controlled drug release and targeting systems: MAPLE deposition and morphological, chemical and in vitro characterization, Appl. Surf. Sci. 255 (2009) 5600–5604.
[50] T. Kokubo, H. Kushitani, S. Sakka, T. Kitsugi, T. Yamamuro, Solutions able to reproduce in vivo surface-structure changes in bioactive glass-ceramic A-W3J, J. Biomed. Mat. Res. A 24 (1990) 721–734.
[51] R. Feng, Z. Song, G. Zhai, Preparation and in vivo pharmacokinetics of curcumin-loaded PCL-PEG-PCL triblock copolymeric nanoparticles, Int. J. Nanomedicine 7 (2012) 4089–4098.
[52] A. Rohman, H.P. Lestari, R. Wulandari, M. Khairiskam, Use of thin layer chromatography and FTIR spectroscopy along with multivariate calibration for analysis of individual curcuminoid in turmeric (*Curcuma longa* Linn) powder, Int. Pharm. Clin. Res. 8 (2016) 419–424.
[53] R. Walter, M.B. Kannan, Y. He, A. Sandham, Effect of surface roughness on the in vitro degradation behaviour of a biodegradable magnesium-based alloy, Appl. Surf. Sci. 279 (2013) 343–348.
[54] A. Han, X. Li, B. Huang, J.K.-H. Tsoi, J.P. Matinlinna, Z. Chen, D.M. Deng, The effect of titanium implant surface modification on the dynamic process of initial microbial adhesion and biofilm formation, Int. J. Adhes. Adhes. 69 (2016) 125–132.
[55] L.L. Hench, J.R. Jones, P. Sepulveda, Bioactive materials for tissue engineering scaffolds, in: J.M. Polak, L.L. Hench, P. Kemp (Eds.), Future Strategies for Tissue and Organ Replacement, Imperial College Press, London, UK, 2002.
[56] M.M. Yallapu, M. Jaggi, S.C. Chauhan, Beta-cyclodextrin-curcumin selfassembly enhances curcumin delivery in prostate cancer cells, Colloids Surf. B Biointerfaces 79 (2010) 113–125.
[57] H. Matusiewicz, Potential release of in vivo trace metals from metallic medical implants in the human body: from ions to nanoparticles – a systematic analytical review, Acta Biomater. 10 (2014) 2379–2403.
[58] M. Cieślik, W. Reczyński, A.M. Janus, K. Engvall, R.P. Socha, A. Kotarba, Metal release and formation of surface precipitate at stainless steel grade 316 and Hanks solution interface – inflammatory response and surface finishing effects, Corros Sci. 51 (2009) 1157–1162.
[59] Y. Okazakia, E. Gotoh, Metal release from stainless steel, Co–Cr–Mo–Ni–Fe and Ni–Ti alloys in vascular implants, Corrosion Sci. 50 (2008) 3429–3438.
[60] L.L. Hench, J.M. Polak, Third-generation biomedical materials, Science 295 (2002) 1014–1021.
[61] N. Sanpo, M.L. Tan, P. Cheang, K.A. Khor, Antibacterial property of cold-sprayed HAAg/PEEK coating, J. Therm. Spray. Techn. 18 (2009) 10–15.
[62] W.H. Song, H.S. Ryu, S.H. Hong, Antibacterial properties of Ag (or Pt)-containing calcium phosphate coatings formed by micro-arc oxidation, J. Biomed. Mater. Res. A 88 (2008) 246–254.
[63] M. Ribeiro, F.J. Monteiro, M.P. Ferraz, Infection of orthopedic implants with emphasis on bacterial adhesion process and techniques used in studying bacterial-material interactions, Biomatter 2 (2012) 176–194.
[64] A.M. Grumezescu, Essential oils and nanotechnology for combating microbial biofilms, Curr. Org. Chem. 17 (2013) 90–96.

The study of the photovoltaic cells parameters in concentrated sunlight

Daniel T. Cotfas[1], Laura Floroian[1], Petru A. Cotfas[1], Dan Floroian[1], Rachamim Rubin[2], Doron Lieberman[2]
[1] *Transilvania University of Brasov, Brasov, Romania*
E-mail: dtcotfas@unitbv.ro, lauraf@unitbv.ro, pcotfas@unitbv.ro, dan.floroian@unitbv.ro
[2] *Weizmann Institute of Science, Israel*
E-mail: Rachamim.Rubin@weizmann.ac.il, Doron.Lieberman@weizmann.ac.il

***Abstract*-The photovoltaic cell parameters are very important for researchers and manufacturers to improve the efficiency of these devices. There are many studies for these parameters in sunlight at one sun or at some suns, but few studies at hundreds or thousands suns. In this paper is presented the study of all important parameters of three types of photovoltaic cells under concentrated sunlight.**

I. INTRODUCTION

Nowadays there are many types of photovoltaic cells, which appeared due to the need to increase the efficiency of photovoltaic cells, to reduce the quantity of materials used and the cost per Watt and to increase the number of applications.

The theoretical efficiency of monocrystalline silicon photovoltaic cell, one of the most used photovoltaic cell, is about 31% [1,2]. The best monocrystalline photovoltaic cell has the efficiency of 25% measured in standard test conditions, STC - under the global AM 1.5 spectrum, the irradiance 1000W/m^2 and the temperature 25 °C, see Table I [3]. This value is very close to the theoretical limit.

A relative new method to increase the efficiency of photovoltaic cell is to use it in concentrated sunlight, the efficiency rising with some percentages in this case, see Table II [3].

Using the concentrated sunlight leads to the reduction of the area of photovoltaic cell and of the materials quantity.

TABLE I
EFFICIENCY OF THE BEST PHOTOVOLTAIC CELL IN ITS GROUP MEASURED IN STC

Photovoltaic cell	Area [cm^2]	Efficiency [%]	Test center
Si monocrystalline	4	25	Sandia
GaAs thin-film	≈1	28.8	NREL
CIGS, CdTe	≈1	19.6	NREL, Newport
Si nanocrystalline	≈1	10.7	FhG-ISE
Dye sensitised	≈1	11.9	AIST
Organic thin-film	≈1	10.7	AIST
InGaP/GaAs/InGaAs Multijunction cell	≈1	37.9	AIST

TABLE II
EFFICIENCY OF THE PHOTOVOLTAIC CELL MEASURED IN CONCENTRATED LIGHT

Photovoltaic cell	Area [cm^2]	Efficiency [%]	Illumination [suns]	Test center
Si monocrystalline	1	27.6	92	FhG-ISE
GaAs thin-film	0.05	29.1	117	FhG-ISE
InGaP/GaAs/InGaAs Multijunction cell	0.162	44.4	302	FhG-ISE

The cost of photovoltaic cell is reduced proportionally with the concentrated ration at a first approximation [4].

The materials and the technologies used to obtain the concentrated sunlight are less expensive than those for photovoltaic cells.

The efficiency was studied for few types of photovoltaic cells in concentrated sunlight, see Table II [3].

The organic photovoltaic cells have recently been studied in concentrated sunlight, especially in order to investigate their stability and degradation [5].

The short circuit current I_{sc}, the open circuit voltage V_{oc}, the fill factor FF and the efficiency η are the photovoltaic cells parameters most widely studied in the concentrated sunlight [4,6,7]. In the studies conducted by Kurtz and Geisz, Slade and Garboushian, Jørgensen et al., it was observed that the short circuit current has a linear dependency in function of the irradiance levels and the open circuit voltage has a logarithmic dependency.

Using the linear dependency of the short circuit current in function of the irradiance makes the photovoltaic cell a good sensor for the intensity of sunlight even in concentrated sunlight.

Taking into account both dependences, the efficiency increases logarithmically with the irradiance levels until the term $I*R_s$ becomes dominant and then slowly decreases.

The goal of this paper is to study the behavior of the other important parameters of the photovoltaic cells: the series resistance R_s, the shunt resistance R_{sh}, the ideality factor of diode m, the reverse saturation current I_o and the photogenerated current I_{ph} in function of different concentrated sunlight levels.

Fig. 1. The land of heliostats at Weizmann Institute of Science Rehovot, Israel.

II. EXPERIMENT SET-UP

The study of the photovoltaic parameters was done in concentrated sunlight at the Solar Research Facility Unit of the Weizmann Institute of Science, Rehovot, Israel, Fig.1.

The experimental system has the following components: solar concentrator system, the robot system, the acquisition system and the I-V characteristic device, Fig. 2, which will be briefly described below.

1. Solar concentrator system

There are many possibilities to produce concentrated sunlight; one of these is to use a system of heliostats, as in Fig. 1.

The solar concentrators can be classified in three classes:

- low concentrator (LCPV) – the concentrated sunlight is between 1 and 40 suns.
- medium concentrator (MCPV) – the concentrated sunlight is between 40 and 300 suns.
- high concentrator (HCPV) – the concentrated sunlight is between 300 and 2000 suns [7,8].

The measurements were taken using the MCPV solar concentrators.

A heliostat with an area of 56 m^2 was used to make the measurements. The photovoltaic cells under test were mounted initially in the outbreak of a second mirror. This mirror is spherical and has an area of 2 m^2.

The variation of the intensity illumination levels can be made by moving the photovoltaic cell on the optical axis of the spherical mirror.

2. Robotic system

During the measurements the temperature of the photovoltaic cells can be increased above 1000^oC due to the concentrated sunlight. At these temperatures the photovoltaic cells and the measuring system can be damaged very quickly.

The robotic and acquisition systems are protected using a piece of alumina. The time when the heliostat is in active position has to be minimized and after measurements the heliostat must quickly be moved in passive position.

The arm of the robotic system assures the protection of the photovoltaic cell under test and of the temperature sensor.

The control of the robotic system is realized with an ATMEGA microcontroller and a National instruments acquisition board.

The arm of robotic system is endowed with an alumina piece to cover the photovoltaic cell. This arm is in closed position until the heliostat arrives in active position, then it passes in open position and gives the triggers for the measurements. After the measurements are taken, the arm of the robotic system passes in closed position to protect the photovoltaic cell.

The robotic system has a display where the status can be seen, the temperature and the alarm, see Fig.3. This system can work in automated mode or in manual mode. One simple switch assures this.

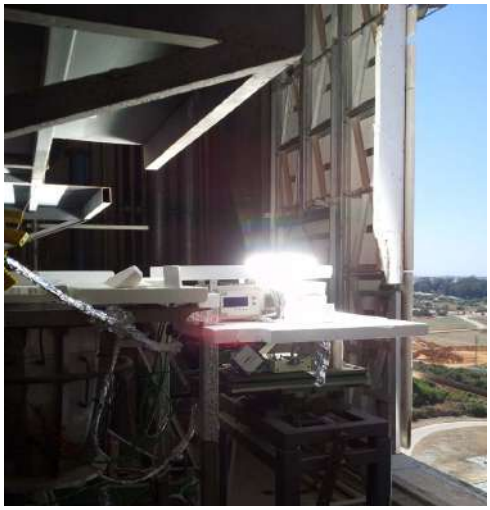

Fig. 2. The experimental set-up.

Fig. 3. The robotic system.

3. *The acquisition system and the I-V characteristic device*

The measurements have to be taken very quickly in order not to damage the photovoltaic cell and to keep the temperature quasi constant.

The acquisition system uses a NI 6009 board. This board has 8 analog input (AI) channels in the configuration Single-Ended Channels. The channels with a sampling rate of 48kS/s and 14 bits resolution are used in the differential measurement mode to increase the accuracy of the measurements. The connection of the board to a laptop is realized by a USB connection.

The current-voltage characteristic of photovoltaic cells can be measured using some techniques [12]:

- the electronic load technique
- the MOSFET technique
- the potentiometer technique
- the capacitor technique

The capacitor technique was chosen due to the fact that the I-V characteristic is measured very quickly. The time required to do this is less than one second. In this case the photovoltaic cell temperature remains almost constant also due to a cell cooling system during measurements. The number of the I-V characteristic points is very high, over 1000. The high number of data enables a good processing after the measurements, thus any method of determining of the photovoltaic parameters can be used.

The design of the electrical circuit allows the selection of the internal capacitor with 0.4F capacitance or of the external capacitor with 2200 μF capacitance in function of the photovoltaic cell generated power. The capacitors used have a very small internal resistance.

4. *Software*

The software was created in the graphical programming language LabVIEW.

The software allows the control of the robotic system, of the acquisition board and of the electronic circuit to automatically measure the I-V characteristic, see Fig. 4.

The software has three steps:

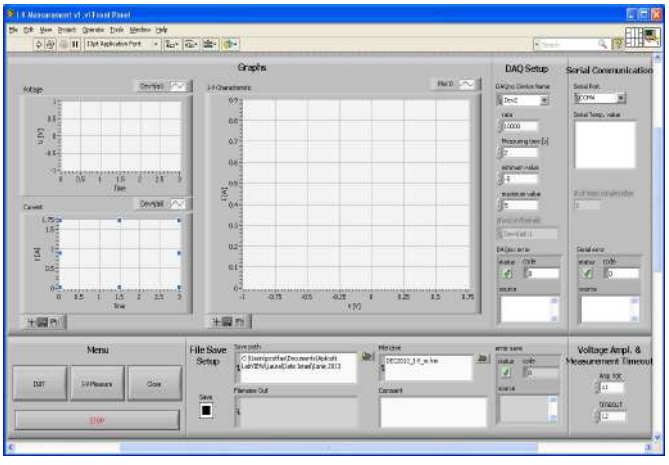

Fig. 3. The panel interface of the software.

- the initializing of the system (INT)– in this step the robotic system and the acquisition system are initialized and verified
- the I-V measurement (I-V Measure) – in this step the I-V characteristic of photovoltaic cell is measured. Using the control "Measuring time" the measurement time of the I-V characteristic can be set in function of the photovoltaic cell and the capacitor used. The amplification for the voltage and current can be set in this step.
- stop the measurement (Close) – is used to stop the measurement, but the system remains initialized. In this step the data is saved.

The graphical indicators "Voltage" and "Current" show the voltage and current during the capacitor charge. The "Serial Temp. value" indicator shows the temperature of the photovoltaic cell during measurements. The temperature is measured using a thermocouple mounted on the back of the photovoltaic cell.

III. RESULTS AND DISCUSSIONS

1. *Methods*

There are many methods to determine the important parameters of photovoltaic cells. These methods can be classified in two categories: the methods which determine all parameters of photovoltaic cells and methods which determine one or more parameters of solar cells.

The parameters in this work were determined using the measured I-V characteristic and the analytical five point method [10,11]**.** This method allows determining all important parameters of photovoltaic cell using the one diode model (1) and one of the I-V characteristic for each level of illumination.

$$I = I_{sc} - I_0\left(\exp\left(\frac{q(V+IR_s)}{mkT}\right)-1\right)-\frac{V+IR_s}{R_{sh}} \quad (1)$$

where k is the Boltzmann constant and q is the elementary electric charge.

The following parameters can be determined using the I-V characteristic: the short circuit current, the open circuit voltage, the maximum power and the coordinates of this point the maximum voltage V_m and the maximum current I_m.

The shunt resistance and the uncorrected series resistance are the first parameters which can be obtained using the linear fitting procedure around the short circuit point and the open circuit point, see (2) and (3).

$$R_{sh} = R_{sho} = -\left(\frac{dV}{dI}\right)_{I=I_{sc}} \quad (2)$$

$$R_{so} = -\left(\frac{dV}{dI}\right)_{V=V_{oc}} \quad (3)$$

The corrected series resistance R_s, the ideality factor of diode m, the reverse saturation current I_o and the photogenerated current I_{ph} are determined using the parameters calculated above and some approximations for the equation (1) [10].

$$m = \frac{A}{V_t(B+C)} \tag{4}$$

where V_t is the thermal voltage, A, B and C are calculated as follows:

$$V_t = \frac{kT}{q} \tag{5}$$

$$A = V_m + R_{so} I_m - V_{oc} \tag{6}$$

$$B = \ln\left(I_{sc} - \frac{V_m}{R_{sh}} - I_m\right) - \ln\left(I_{sc} - \frac{V_{oc}}{R_{sh}}\right) \tag{7}$$

$$C = \frac{I_m}{I_{sc} - \frac{V_{oc}}{R_{sh}}} \tag{8}$$

The other parameters I_o, R_s and I_{ph} are determined using the following equations:

$$I_o = \left(I_{sc} - \frac{V_{oc}}{R_{sh}}\right)\exp\left(-\frac{V_{oc}}{mV_T}\right) \tag{9}$$

$$R_s = R_{so} - \frac{nV_t}{I_o} exp\left(-\frac{V_{oc}}{mV_T}\right) \tag{10}$$

$$I_{ph} = I_{sc}\left(1 + \frac{R_s}{R_{sh}}\right) + I_o\left(\exp\left(\frac{I_{sc}R_s}{mV_T}\right) - 1\right) \tag{11}$$

2. The photovoltaic cells

The photovoltaic cells under test are the following:

- the commercial monocrystalline silicon photovoltaic cell (mc-SI) with an area of 0.5cm^2
- the commercial polycrystalline silicon photovoltaic cell (pc-SI) with an area of 0.5cm^2
- the thin films CdTe photovoltaic cell developed in the lab with an area of 0.5cm^2.

3. The variation of the photovoltaic cell parameters in function of the illumination levels

The parameters of photovoltaic cells were determined at different levels of illumination, at 1000W/m^2 that means one sun, 50 suns, 100 suns and 150 suns at 25°C temperature. The I-V characteristics for the monocrystalline silicon photovoltaic cell are presented in Fig. 4.

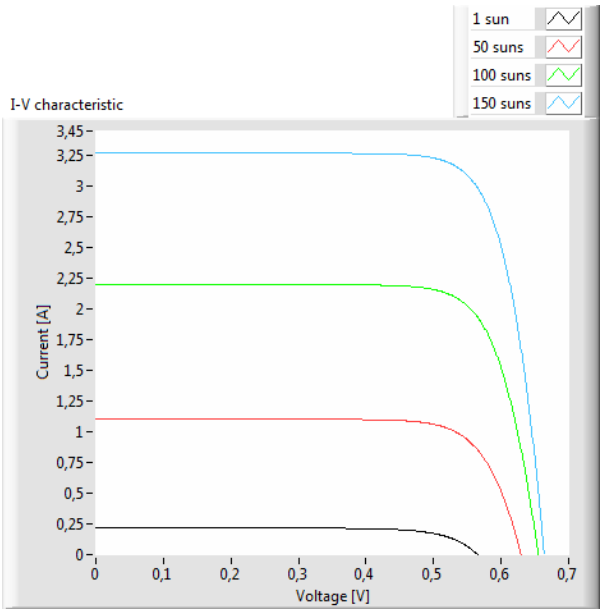

Fig. 4. The I-V characteristics for mc-Si. The current of the characteristic for one sun is multiplied ten times.

The software called SolarLab was used to calculate the parameters of photovoltaic cells. This soft allows importing the saved data and then using (2-11) to determine the parameters of the photovoltaic cells.

The values of the parameters of the three photovoltaic cells calculated for four levels of illuminations are presented in Table III.

The dependency obtained for the photogenerated current of the photovoltaic cells in function of the concentrated sunlight is presented in Fig. 5. It can be observed that the linearity of

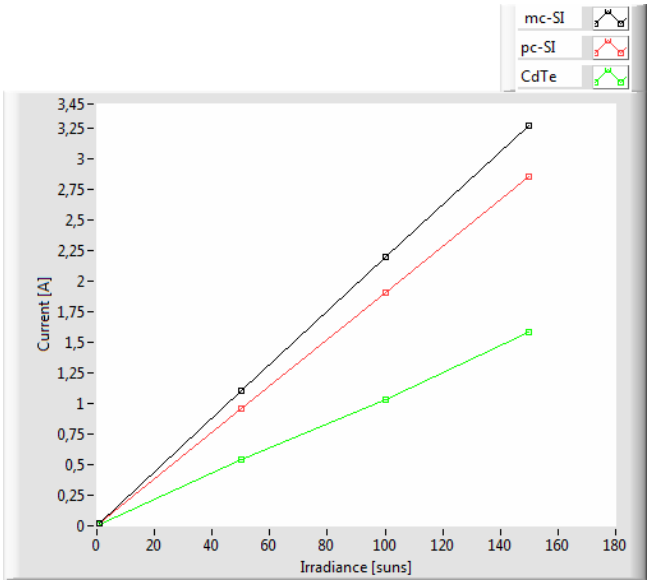

Fig. 5. The linearity of the photogenerated current

the dependency is verified for all three photovoltaic cells under test.

The series resistance decreases when the intensity of sunlight increases. This happens due to the increase of the active layer conductivity when the irradiance grows [13,14]. The dependency of the series resistance on the concentrated sunlight is presented in Fig. 6. The decrease of the series resistance is more accentuated for the CdTe cell.

The values of the ideality factor of diode and the reverse saturation current depend on the recombination mechanisms.

For low sunlight intensity the space recombination is important and at high sunlight intensity the space recombination decreases, leading to drop of the values of m and I_o with the increase of the illumination.

By the analysis of the data obtained, it is observed that the shunt resistance has a more significant growth for 1sun- 50 suns, afterward the growth being saturated.

IV. CONCLUSIONS

Three types of photovoltaic cells were characterized under medium concentrated sunlight: mono and polycrystalline silicon and CdTe.

All important parameters of the photovoltaic cells were determined and analyzed.

TABLE III
THE PHOTOVOLTAIC CELL PARAMETERS

Photovoltaic cell / Parameters	Irradiance	mc-Si	pc-Si	CdTe
I_{ph} [A]	10^3 W/m^2	0.0221	0.0191	0.0109
I_o [A]		1.003E-8	1.68E-8	4.2E-7
R_s [Ω]		0.067	0.0811	0.313
R_{sh} [Ω]		627	691	342
m		1.51	1.56	2.98
I_{ph} [A]	$5x10^4$ W/m^2	1.102	0.954	0.541
I_o [A]		8.78E-9	1.01E-8	1.35E-7
R_s [Ω]		0.017	0.029	0.1
R_{sh} [Ω]		687	769	394
m		1.315	1.31	2.19
I_{ph} [A]	10^5 W/m^2	2.198	1.907	1.032
I_o [A]		3.58E-9	3.57E-9	4.06E-8
R_s [Ω]		0.011	0.014	0.045
R_{sh} [Ω]		722	795	432
m		1.26	1.23	1.97
I_{ph} [A]	$15x10^4$ W/m^2	3.269	2.86	1.589
I_o [A]		2.88E-8	2.56E-9	2.6E-8
R_s [Ω]		0.007	0.0103	0.0297
R_{sh} [Ω]		741	811	448
m		1.24	1.2	1.89

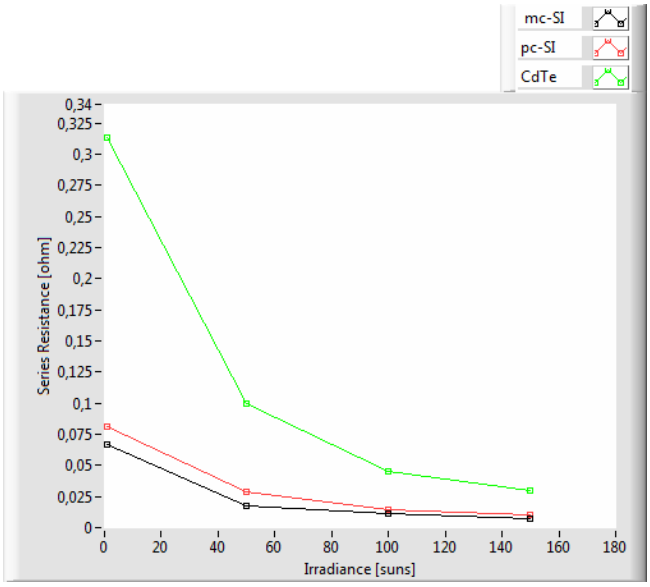

Fig. 6. The dependence of series resistance vs. irradiance

The measurement system and the necessary software to determine the parameters of photovoltaic cells were realized.

Three parameters of photovoltaic cells, I_o, R_s and m decrease with the illumination. The dependency of the shunt resistance has two parts: there is a growth in the first part, and then, in the second part, the growth is saturated.

The short circuit and the photogenerated currents present a growth which is proportional with the illumination, while the open circuit voltage has a logarithmic dependence.

In the future research works the Emcore multijunction photovoltaic cell- InGaP/InGaAs/Ge will be characterized in the same conditions.

ACKNOWLEDGMENT

Financial support by the Access to Research Infrastructures activity in the 7th Framework Programme of the EU (SFERA Grant Agreement n. 228296) is gratefully acknowledged.

The Romanian authors also kindly acknowledge and appreciate the support of the Solar research facility unit from Weizmann Institute of Science, Rehovot, Israel, where all the measurements were performed.

REFERENCES

[1] Y. Zhao, M.Y. Sheng, W. X. Zhou, Y. Shen, E. T. Hu, J. B. Chen, M. Xu, Y. X. Zheng, Y. P. Lee, D. W. Lynch and L. Y. Chen, "A solar photovoltaic system with ideal efficiency close to the theoretical limit," *Optics Express,* vol. 20, Issue S1, pp. A28-A38, 2012.

[2] C. H. Henry, "Limiting efficiencies of ideal single and multiple energy gap terrestrial solar cells," *J. Appl. Phys.,* vol. 51, pp. 4494-4500, 1980.

[3] M.A. Green1, K. Emery, Y. Hishikawa, W. Warta and E. D. Dunlop, "Solar cell efficiency tables (version 42)," *Prog. Photovolt: Res. Appl.,* vol. 21, pp. 827-837, 2013.

[4] S. Kurtz and J. Geisz, "Multijunction solar cells for conversion of concentrated sunlight to electricity," *Optics Express,* vol. 18, no. S1, pp. A73-A78, 2010.

[5] M. Jørgensen, K. Norrman and F. C. Krebs, "Stability/degradation of polymer solar cells," *Sol. Energy Mater. Sol. Cells*, vol. 92, pp. 686-714, 2008.

[6] A. Slade and V. Garboushian, "27.6% Efficient Silicon Concentrator Solar Cells for Mass Production," Amonix Inc., 2006.

[7] P. Yadav, B. Tripathi, M. Lokhande and M. Kumar, "Effect of Temperature and Concentration on Commercial Silicon Module based Low-concentration Photovoltaic (LCPV) System," *Journal of Renewable and Sustainable Energy*, vol. 5, pp. 013113-1-10, 2013.

[8] P. Pérez-Higueras, E. Muñoz, G. Almonacid and P. G. Vidal, "High concentrator photovoltaics efficiencies: present status and forecast," Renewable and Sustainable Energy Reviews, vol. 15, no. 4, pp. 1810–1815, 2011.

[9] D. Floroian, L. Floroian, R. Rubin, D. Lieberman, P. A. Cotfas, D. T. Cotfas, D. Ursutiu and C. Samoila, "Measurements in Concentrated Sun using a Remote Controlled Robot," *International Journal of Online Engineering*, vol. 9, pp. 50-54, 2013.

[10] D. Chan and J. Phang, "Analytical methods for the extraction of solar cell single and double diode model parameters from I-V characteristics," *IEEE Transactions on Electron Devices*, vol. 34, no. 2, pp. 286– 293, 1987.

[11] D. T. Cotfas, P. A. Cotfas and S. Kaplanis, "Methods to determine the dc parameters of solar cells: A critical review," *Renewable and Sustainable Energy Reviews*, vol. 28, pp. 588–596, 2013.

[12] D. T. Cotfas, P. A. Cotfas, D Ursutiu and C. Samoila, "Current-Voltage Characteristic Raising Techniques for Solar Cells. Comparisons and Applications," *Optimization of Electrical and Electronic Equipment (OPTIM), 2010 12th International Conference on Brasov*, pp. 1115 - 1120, 2010, IEEE Xplore, 10.1109/OPTIM.2010.5510373.

[13] M. Paire, L. Lombez, N. Péré-Laperne, S. Collin, Jean-Luc Pelouard, D. Lincot and Jean-François Guillemoles, "Microscale solar cells for high concentration on polycrystalline Cu(In,Ga)Se_2 thin films," *Applied Physics Letters*, vol. 98, pp. 264102, 2011.

[14] M. D. Lammert, R. J.Schwarts, "The integrated back contact solar cell: A silicon solar cell for use in concentrated sunlight," *IEEE Transactionson Electron Devices*, ED-24, pp. 337–342, 1977.

PLOS ONE

RESEARCH ARTICLE

Ochratoxin A Detection on Antibody-Immobilized on BSA-Functionalized Gold Electrodes

Mihaela Badea[1☯], Laura Floroian[2☯*], Patrizia Restani[3☯*], Simona Codruta Aurora Cobzac[4☯], Marius Moga[5☯]

1 Fundamental, Prophylactic and Clinical Specialties Department, Transilvania University of Brasov, Brasov, Romania, **2** Automation and Information Technology Department, Transilvania University of Brasov, Romania, **3** Dipartimento di Scienze Farmacologiche e Biomolecolari, Università degli Studi di Milano, Milano, Italy, **4** Faculty of Chemistry and Chemical Engineering, Babes-Bolyai University, Cluj-Napoca, Romania, **5** Department of Medical And Surgical Specialties, Transilvania University of Brasov, Brasov, Romania

☯ These authors contributed equally to this work.
* lauraf@unitbv.ro; patrizia.restani@unimi.it

CrossMark
click for updates

OPEN ACCESS

Citation: Badea M, Floroian L, Restani P, Cobzac SCA, Moga M (2016) *Ochratoxin A* Detection on Antibody- Immobilized on BSA-Functionalized Gold Electrodes. PLoS ONE 11(7): e0160021. doi:10.1371/journal.pone.0160021

Editor: Kausar Ansari, CSIR-Indian Institute of Toxicology Research, INDIA

Received: April 19, 2016

Accepted: July 12, 2016

Published: July 28, 2016

Copyright: © 2016 Badea et al. This is an open access article distributed under the terms of the Creative Commons Attribution License, which permits unrestricted use, distribution, and reproduction in any medium, provided the original author and source are credited.

Data Availability Statement: All relevant data are within the paper.

Funding: MB, LF, PR, and MM received funding from the European Community's Seventh Framework Programme (FP7/2007-2013) under grant agreement n245199. It has been carried out within the PlantLIBRA project (website: www.plantlibra.eu). The funders had no role in study design, data collection and analysis, decision to publish, or preparation of the manuscript.

Competing Interests: The authors have declared that no competing interests exist.

Abstract

Ochratoxin A (OTA)—a toxin produced by *Aspergillus carbonarius*, *Aspergillus ochraceus*, and *Penicillium verrucosum*—is one of the most-abundant food-contaminating mycotoxins. To avoid the risk of OTA consumption for humans and animals, the rapid detection and quantitation of OTA level in different commodities are of great importance. In this work, an impedimetric immunosensor for ochratoxin A (OTA) detection, a common toxic botanical contaminant, was developed via the immobilization of anti-OTA antibody on bovine serum albumin modified gold electrodes. A four-step reaction protocol was tested to modify the gold electrode and obtain the sensing substrate. All the steps of the immunosensor elaboration and also the immunochemical reaction between surface-bound antibody and ochratoxin A were analyzed using cyclic voltammetry and electrochemical impedance spectroscopy. Modification of the impedance due to the specific antigen-antibody reaction at immunosensor surface, was used in order to detect ochratoxin A. Linear proportionality of the charge transfer resistance to the concentration of OTA allows ochratoxin A detection in the range of 2.5–100 ng/mL.

Introduction

Ochratoxin A (OTA) is a mycotoxin produced by *Aspergillus ochraceus*, *Aspergilius niger* and *Penicillium verrucosum*, found as contaminants of a variety of food, such as cereals, coffee beans, beans, grapes and dried fruit. OTA is one of the most toxic and widespread compound from the ochratoxins group [1,2].

Studies have shown that OTA can have specific toxicological effects such as nephrotoxic, teratogenic, neurotoxic, hepatotoxic and immunotoxic, and it is believed to cause increased oxidative stress at a cellular level [3,4]. The concerns about OTA contamination determined different research groups to develop high-performance detection techniques for quality assessment.

Fourty years ago, OTA was identified as a corn contaminant in USA, being produced by *Penicillium viridicatum* wrestling. Ever since, OTA has been found through the whole world: in regions with cold and temperate climate it is produced by *Penicillium verrucosum* and by *Aspergillus carbonarius* and also in regions with hot and tropical climate, where it is produced by *Aspergillus ochraceus*. *Penicillium verrucosum* is the specific fungi of stocked cereals, while *Aspergillus ochraceus* is the most common champignon of the green coffee, spices, cocoa, soya, peanuts, rice and *Aspergillus carbonarius* is contaminant of grapes [5]. Even though crop fungi contamination can take place pre and post-harvest, OTA synthesis is believed to be performed during the storage period. The mechanism of the OTA biosynthesis by different fungi and the coding genes are not well known. It is clear that OTA production depends on the toxicogenic power of the strains but also on the common practices during the food processing. For example, prevention of OTA production in the cereals is achieved by controlling the humidity conditions during the filling of the grain elevator and during storage, knowing that a water activity higher than 0.8 (aw) is favorable to the development of *Penicillium verrucosum*. OTA contamination of grapes in the wine yards is explained only by the fruit damages made by insects or by the harvest devices, because, by default, *Aspergillus* strains are not pathogenic for the wine yard itself.

Analytical methods for OTA quantification follow the same steps as the ones for the quantification of mycotoxins: sampling and sample preparation, extraction, purification (clean-up), separation and detection. European Commission regulation No. 401/2006 from 23 February 2006 lays down the methods of sampling and analysis used for the official control of the amount of mycotoxins in foodstuffs. The separation methods are coupled with the detection technique that is sensitive enough to fulfill the legally imposed limits, but they require sample extraction and clean-up and they are rather expensive and demand specially trained personnel. Specific clean-up methods includes immunoaffinity columns [6,7]. After this step, HPLC was recommended in order to detect the occurence of ochratoxin in food commodities: coffee, pepper, chili, prickly ash, cinnamon, aniseed, fennel, curry powder and cumin [7–9].

Chemical and enzymatic assays were used with success in small-molecule detection [10], but nowadays the immunoassays are considered novel screening methods which provide sensitive detection and can be used by non-specialists under field conditions. Although there is a great emphasis on their selectivity, the main drawback is still their cross-reactivity. Scientific literature indicated that false-negative results are rarely reported, but false-positive results are more frequent and depend on several factors like temperature, pH, sample viscosity or ionic strength [11]. Without sample clean-up or extraction before the testing, matrix effects might be expected leading to significant overestimation of mycotoxin concentration, especially in colorimetric detection when color samples are tested. Therefore, positive results should be confirmed with the conventional analytical methods to avoid misinterpretations.

Electrochemical sensors and biosensors are an alternative solution due to their design and method of detection. For example, OTA was detected using square wave voltammetry at a glassy carbon electrode (GeE) [12]. Limit of detection of this assay was of 0.02 μg/kg and the sensor was used for the detection of OTA extracted from wine sample using antibody modified magnetic nanoparticles.

A biosensor for the detection of OTA was designed via the immobilization of HRP on screen printed carbon electrode (SPCE) using a polypyrrole matrix [13].

Immunosensors have also been developed for effective and fast screening of OTA in foodstuffs. These are based on a variety of detection techniques such as electrochemical [14,15], optical (e.g surface plasmon resonance [16], optical waveguide light-mode spectroscopy technique [17], fluorescence [18,19] etc) and acoustic methods (quartz crystal microbalance immunosensors [20]).

Kinetics and mechanisms of electron-transfer processes that correspond to the biocatalytic reaction occurring at modified electrodes and also interfacial properties changes of modified electrodes [21,22], such as those linked to biorecognition events involving antibody–antigen binding, at modified surfaces [23] can be analyzed with the powerful tool of electrochemical impedance spectroscopy (EIS).

Electrochemical detection systems seem most promising thanks to their high sensitivity, feasibility of low cost, low endogenous background, compatibility with portability and miniaturization.

Several reviews have been published on the use of EIS in biosensors [24,25]. Using EIS method, there were monitored the changes in the electrical properties at the (bio)sensors interface.These changes can be associated with specific binding events due to the recognition between an analyte and a ligand. Antibodies and more recently, aptamers [26,27], have been used as biorecognition elements in biosensors with EIS detection. Literature data indicated EIS methods for ochratoxin detection from different matrices (Table 1).

In this work, an impedimetric immunosensor for the detection of ochratoxin A was developed via the immobilization of the anti-OTA antibody gold electrodes previously modified with a cross-linked film of bovine serum albumin. A four-step reaction protocol was tested in order to modify the gold electrode and obtain the sensing substrate. All the steps of the immunosensor elaboration and also immunochemical reaction between surface-bound antibody and ochratoxin A were analyzed using cyclic voltammetry and electrochemical impedance spectroscopy. Modification of the impedance appeared at immunosensor surface due to the specific antigen-antibody reaction was used in order to detect ochratoxin A. Specifically, the increase of the electron-transfer resistance (R_{ct}) at the interface was correlated with OTA concentration in the range of interest.

Materials and Methods

Materials and reagents

Gold printed electrode DRP-250AT was purchased from DS Dropsens (Spain). The electrodes (SPCEs) incorporate a conventional three-electrode configuration, which comprises a disk-

Table 1. Sensors used for ochratoxin A detection.

Type of biosensor	Methods used to characterize the electrodes	Linear range	Detection limit (and other parameters)	References
Highly sensitive and reusable electrochemical impedimetric aptasensor	CV, EIS	1.25 ng/L—500 ng/L	0.25 ng/L	[28]
Direct competitive immunosensor	the substrate the p-benzoquinone generated enzymatically was detected by differential-pulse voltammetry		in wines was of 0.11 ± 0.01 ng/L	[29]
A Langmuir-Blodgett (polyaniline (PANI)-stearic acid (SA)) film based highly sensitive and robust impedimetric aptasensor	SEM, FTIR, CV, EIS, contact angle measurements	0.1 ng/mL -10 ng/mL, and 1 μg/mL-25 μg/mL	0.1 ng/ml in 15 min can be reused ~13 times	[30]
A self-assembled monolayer (SAM) of 11-amino-1-undecanethiol (AUT) has been fabricated onto a gold (Au) substrate to co-immobilize anti-ochratoxin-A antibodies (AO-IgGs) and bovine serum albumin (BSA)	SEM, CV, DPV, EIS	over 0.5–6.0 ng/dL	0.08 ng/dL using 3σb/m criteria, response time of 30 s, regression coefficient of 0.999	[31]
Nanostructured zinc oxide (Nano-ZnO) film has been deposited onto indium-tin-oxide (ITO) glass plate for co-immobilization of rabbit-immunoglobulin antibodies (r-IgGs) and bovine serum albumin (BSA)	XRD, FTIR, SEM, EIS	0.006–0.01nM/dm^3	0.006 nM/dm^3, response time as 25s, regression coefficient of 0.997	[32]

doi:10.1371/journal.pone.0160021.t001

shaped Au working electrode (1.6 mm diameter, 0.0196 cm^2 geometrical area), Au counter electrode and silver pseudo-reference electrode.

N-Hydroxysuccinimide (NHS—PubChem CID: 80170), N-(3-dimethylaminopropyl)-N'-ethylcarbodiimide (EDC—PubChem CID: 15908), potassium ferrocyanide ($K_4Fe(CN)_6$—PubChem CID: 71309461), potassium ferricyanide ($K_3Fe(CN)_6$—PubChem CID: 26250), Ochratoxin A (PubChem CID: 442530) were purchased from Sigma–Aldrich, St. Louis (USA). Bovine serum albumin (BSA) Crystalized 100% was purchased from Mann Research Laboratories Division of Becton Dickinson & Co NY (USA) and monoclonal antibody anti-Ochratoxin A from Novus Biologicals (Canada). Acetic acid (PubChem CID: 176), sodium acetate trihydrate (PubChem CID: 23665404), acetonitrile (PubChem CID: 6342), sulphuric acid (PubChem CID: 1118) and ethanolamine (PubChem CID: 700) were purchased from Chemical Company, Iasi (Romania).

Buffers and solutions

Acetate buffer pH 5.6, comprising of 0.1 M acetic acid and 0.1 M sodium acetate was prepared using distilled deionized water. BSA 5 mg/mL in acetate buffer and antibody solution 5 μg/mL in acetate buffer were prepared.

A solution containing 0.1 M KCl, 5 mM $K_3[Fe(CN)_6]$ and 5 mM $K_4[Fe(CN)_6]$ was used in cyclic voltammetry and electrochemical impedance spectroscopy measurements. Blocking buffer solution consisted of ethanolamine 0.1 M in water and NHS and EDC solution were also prepared in deionized water.

OTA 5 mg/mL was diluted in different concentration in acetate buffer.

Apparatus

An Autolab PGSTAT100 Eco Chemie (Netherlands) potentiostat was used to carry out the impedance spectra at 10 mV sinusoidal ac potential perturbation in the frequency range from 10^4 to 10^{-1} Hz, superimposed on +0.178 V dc potential, that is the potential of the ferrocyanide/ferricyanide couple $[Fe(CN)6]^{4-}/^{3-}$. The spectra were taken in 1mM ferrocyanide/ferricyanide solution (1:1 mixture) in 0.1M KCl as background electrolyte at room temperature. All the measurements were performed in a solution of The FRA 4.9 software calculates and records the real and imaginary parts of electrochemical impedance (Z' and Z") together with the phase and represents them in Nyquist and Bode diagrams.

EIS using the classic ferricyanide/ferrocyanide redox probe was frequently used for quantitation of various molecules with biosensors, including with real samples. A few recent examples for ochratoxin A were included in Table 1. The ionic strength of the solution was always the same and controlled by the composition of the electrolyte. All measurements were done in 5 mM potassium ferri/ferrocyanide in 0.1M KCl, before and after incubation with the standard or sample solution, as indicated in Experimental-Solutions and Buffers section.

Based upon the principles of electrochemical spectroscopy, the equivalent electric circuit that best fits the experimental data was found and optimum electrical parameters were obtained: electrical resistance of the solution, charge transfer resistance, constant phase element and Warburg impedance. For each modified electrode, the impedance spectra were recorded before and after incubation with the standard or sample solution. The variation in the R_{ct} following incubation with standard/sample was calculated as $\Delta R_{ct} = R_{ct}(after)-R_{ct}(before)$ and was correlated with the concentration of aflatoxin in the sample.

Electrode modification and immobilization of the antibodies

Before modification, Dropsens gold electrode have been subjected to electrochemical pretreatment by applying 10 potential cycles between -0.3 and +1.5 V / pseudo silver reference

electrode with 100 mV/s scan rate in 0.5 M H_2SO_4 solution until the voltammogram characteristic for a clean Au surface was obtained.

The clean gold electrode was first modified using BSA/EDC/NHS, creating a cross-linked film that prevents the non-specific binding of OTA on gold, and allows further covalent attachment of antibody. Electrode modification was performed as described by Polonschii et al. [33], 5 mg/ mL BSA (50 μL), 20 μL of 0.4M EDC and 20 μL of 0.1 M NHS were mixed and allowed to stand 5 minutes at room temperature. Afterwards, 10 μL of this mixture were evenly spread on the working electrode and allowed to stand at room temperature for 30 minutes in a humid atmosphere. The electrode was rinsed with a lot of water and dried in air.

Next, the terminal carboxylic groups on BSA film were activated by dropping 10 μL of a 1:1 mixture of EDC/NHS onto the sensor surface, allowing the reaction to proceed, allowing it to react for 40 min at room temperature in a humid dark room. The electrode surface was rinsed after each step thoroughly with copious amounts of water for removing the unbound material. After this, the antibody anti-OTA immobilization was done by covering the modified electrode surface with a 10 μL droplet of the 5 μg/mL antibody solution in acetate buffer, allowing it to react in a water-saturated atmosphere for 1 h at room temperature. After incubation the electrode was rinsed in water to remove unbound antibodies and 75 μL ethanolamine 1M solution was drop cast onto the modified surface and incubated 15 min with the aim to deactivate the remaining succinimide groups and also to block unreacted active sites. These modified electrodes can then be stored dry several days at 4°C without a decrease in the sensitivity, or they can be subjected to immunochemical reaction.

A schematic representation of the analytical principle of this electrochemical immunoassay is shown in Fig 1.

For the OTA measurement, 10 μL of either sample or OTA standard solutions of different concentrations in acetate buffer pH 5.6 were pipetted onto the working electrode area and allowed to stand at room temperature for 45 min in a humid atmosphere (to prevent evaporation). The immunosensor was rinsed with a large amount of water before the electrochemical measurements.

Parameters such as the incubation time and the amount of antibody/electrode were optimized to obtain good analytical characteristics, appropriate for Ochratoxin A detection in real samples.

Results and Discussion

Electrochemical measurements

We have performed Faradic electrochemical impedance spectroscopy measurements using the classic redox probe ferricyanide/ferrocyanide, at the formal potential of this reversible redox

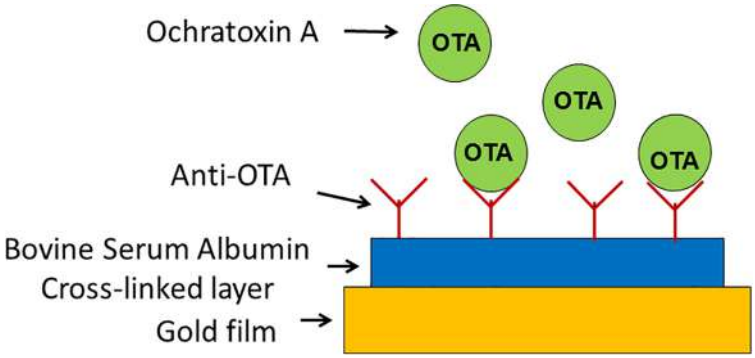

Fig 1. Schematic outline of the electrochemical immunosensor for OTA determination.

doi:10.1371/journal.pone.0160021.g001

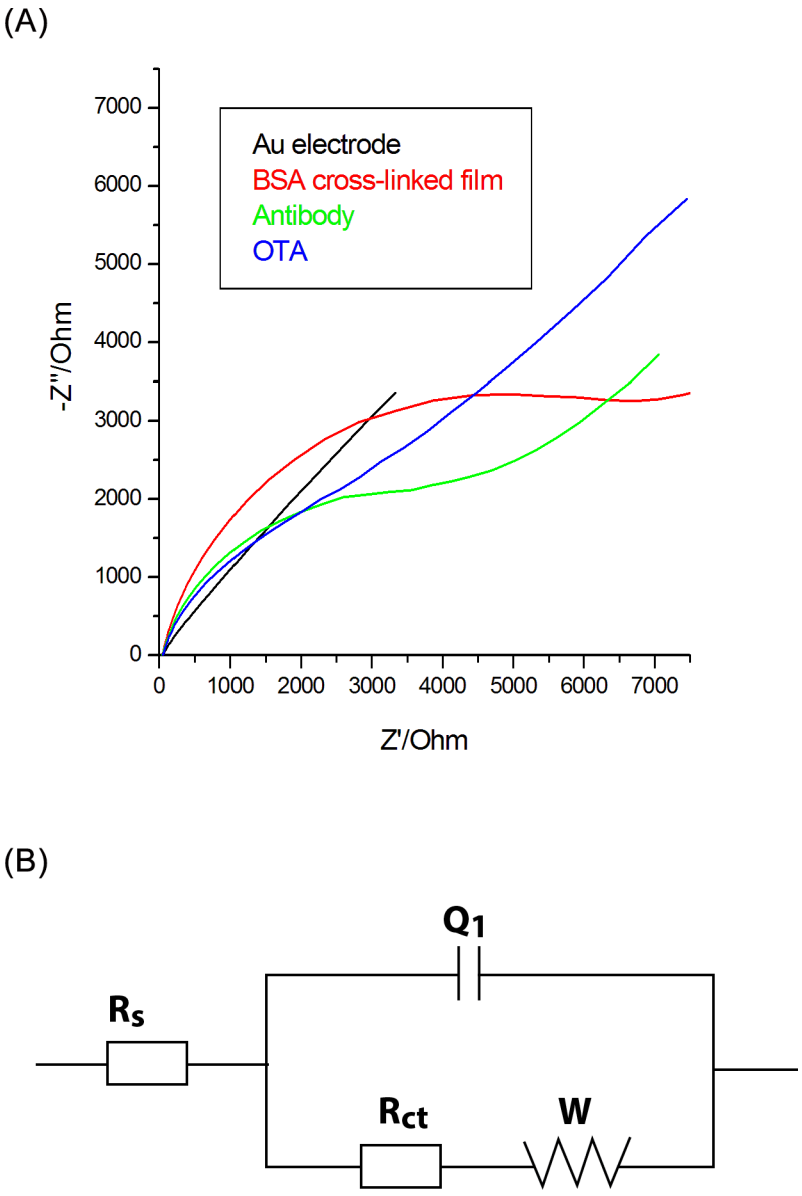

Fig 2. A) EIS Nyquist spectra of each modification electrode step, at 10 mV sinusoidal ac potential perturbation, 10^{4} to 10^{-1} Hz frequency, ferricyanide/ferrocyanide redox couple and B) Equivalent electric circuit.

doi:10.1371/journal.pone.0160021.g002

couple, in order to induce the slightest possible perturbation in the system, as was recommended by Bard and Faulkner [34].

Fig 2A displays the Nyquist impedance spectra recorded upon the stepwise process of electrode modification, providing specific information on the barrier properties and the changes at the interface sensor-solution throughout the biosensor building process. The bare gold electrode showed an extremely small semicircle domain (black curves), implying a very low electron-transfer resistance of the redox probe.

After the grafting of the BSA film on the electrode, R_{ct} increased significantly (red curves), due to the deposition on the electrode surface of an organic layer with negatively charged terminal carboxylic groups COO^{-} (the isoelectric point of BSA being 4.7).

The protein layer acts as a physical and an electrostatic barrier for the $[Fe(CN)_6]^{4-/3-}$ anions, preventing redox probe to reach the electrode surface and slowing down the electron transfer kinetic between the probe and the electrode. Similar approaches were also used by Radi and colab. [26]. Next, antibodies were covalently immobilized onto the BSA modified electrode and a remarkable drop in the R_{ct} was observed (blue curves) because the negative charge of BSA- modified electrode is partly neutralized by the covalent attachment of the antibody. Afterwards, the R_{ct} increased when the sensor was used for OTA detection (magenta curves), as the OTA binding to surface-bound antibody created an additional barrier to the electron transfer at the interface.

Variants of equivalent electrical circuits were tested before choosing the most appropriate circuit for our experimental curves from Fig 2A. For this circuit, by using the facilities of FRA 4.9 software, we analysed each individual response for each experimental step and we considered the data where we obtained the low Chi-square values. The impedance data were fitted to equivalent circuit shown in the Fig 2B that includes the solution resistance (R_s), the charge transfer resistance (R_{ct}), the constant phase element (Q) and the Warburg impedance element (W).

Ideally, W and Rs represent the properties of the electrolyte and diffusion features of the redox probe in this solution and they are not affected by modifications at the electrode surface. Q value depends very much on the dielectric properties of the layer that separates the electrode surface and the ionic charges, the thickness of the separation layer and surface area of the electrode. A large increase in the Q value was noted when bare Au electrode was covered with BSA-EDC-NHS layer, whereas a Q decrease was observed upon further attachment of the antibody or of OTA to the sensor interface.

R_{ct} value depends on the insulating properties at the electrolyte/electrode interface. R_{ct} changes were much larger than those in other impedance components, and thus R_{ct} can be considered an adequate signal for the determination of the interfacial properties for the prepared immunosensor.

The experiments were run in triplicated and statistical analysis was used. Table 2 shows the average values of equivalent circuit parameters for all the steps of the immunosensor elaboration and also for the immunochemical reaction between ochratoxin A and its antibody.

EIS is a sensitive tool for monitoring affinity interactions at surfaces, but particularly due to this high sensitivity it is highly recommended to confront the impedance results with other electrochemical techniques (cyclic voltammetry, linear swept voltammetry or differential pulse voltammetry), and to record a good parallel control of the samples [35].

It was observed that our results are consistent with the cyclic voltammetry curves shown in Fig 3A.

The cyclic voltammograms of soluble electroactive species provide a convenient tool for monitor the various stages of the immunosensor building on gold electrode. The CV-s were performed after all the step of electrode modification and also after toxin adding on electrode surface. Fig 3A shows the CV-s in solution of 5 mM ferricyanide in 0.1 M KCl, 100 mV/s scan rate, for initial gold electrode, BSA/EDC/NHS modified electrode, antibody anti-OTA/BSA/

Table 2. Averages values of the equivalent circuit parameters for various steps of the immunosensor.

Modification	Rs (Ω cm^2)	Q (10^{-6}μF)	n	Rct (Ω cm^2)	W (10^{-6} Ω cm^2)
Bare electrode	4.10	142	0.92	1.267	806
BSA-cross linked film	4.52	513	0.85	413	635
Anti-OTA Antibody	4.29	238	0.88	157	683
OTA 10 ng/mL	3.97	122	0.86	307	724

doi:10.1371/journal.pone.0160021.t002

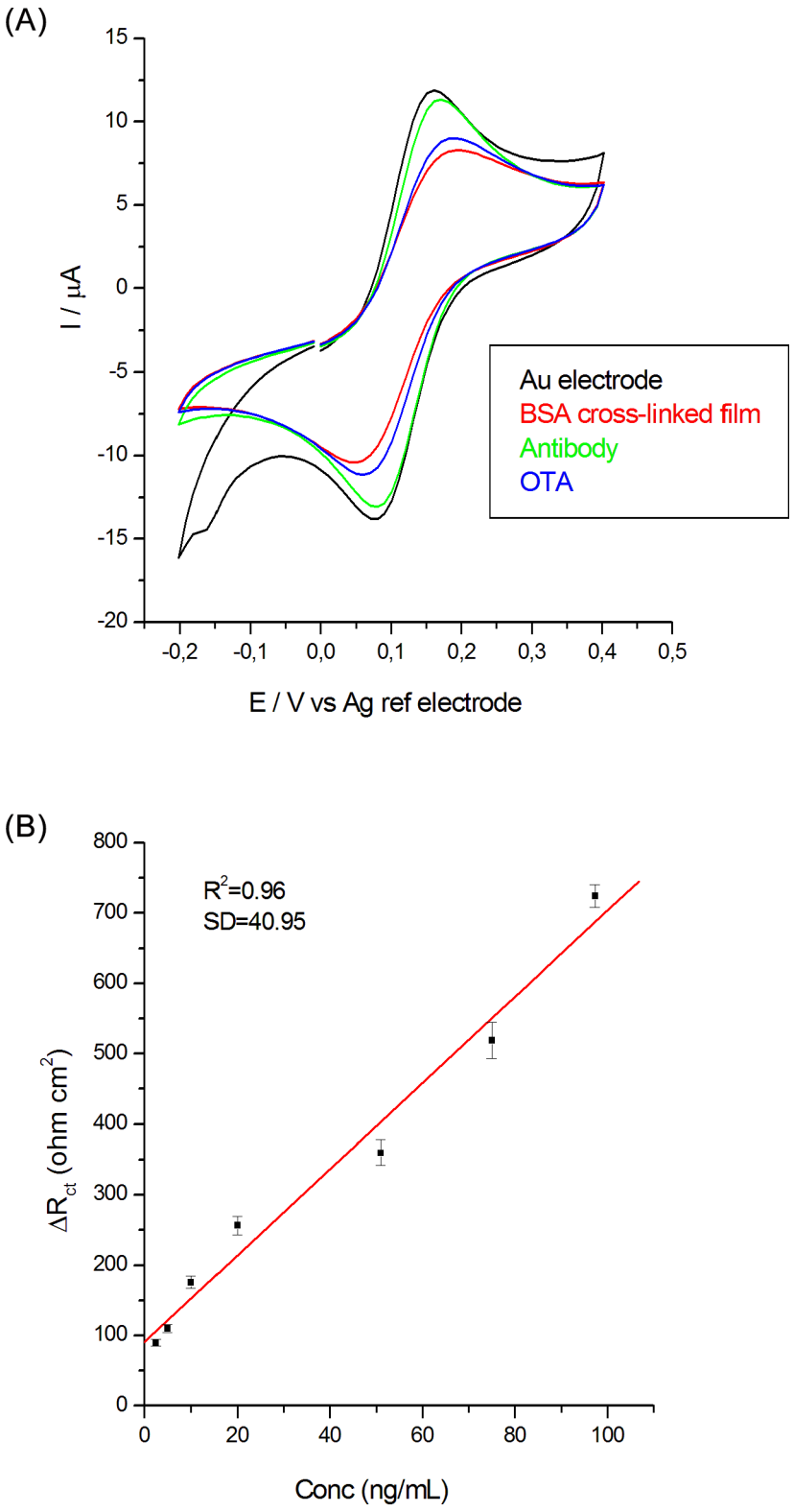

Fig 3. A) CVs of the sample at 0.1 V/s scan rate in ferricyanide/ferrocyanide redox couple, after each step of the immunosensor build-up and B) OTA calibration curve.

doi:10.1371/journal.pone.0160021.g003

Table 3. Average values of the equivalent circuit parameters for various OTA concentrations.

Conc. OTA (ng/mL)	Rs (Ω cm^2)	Q (10^{-6}μF)	n	Rct (Ω cm^2)	W (10^{-6} Ω cm^2)	ΔRct (Ω cm^2)
100	4.16	172	0.85	1451	712	724
75	4.22	128	0.86	884	744	519
50	3.98	120	0.90	759	866	370
20	4.06	120	0.90	431	804	256
10	3.97	122	0.86	307	724	176
5	4.27	137	0.83	641	820	110
2.5	4.01	92	0.84	934	887	90

doi:10.1371/journal.pone.0160021.t003

EDC/NHS modified electrode and after formation of immunochemical complex on the surface of the anti-OTA/BSA/EDC/NHS modified electrode after 15 ng/mL OTA solution addition.

The cyclic voltammograms are strongly affected by the deposited layers, the difference between the anodic and cathodic peak potentials does not remained constant, whereas the peak current modifies significantly. It can be seen initial the characteristic quasireversible redox cycle for a bare Au electrode and after its functionalization with BSA/EDC/NHS, the electron transfer between the redox probe and electrode surface was severely affected and an obvious decreasing of the anodic and cathodic peaks was observed. After the Ab immobilization on the functionalized electrode surface, the peak currents of the redox couple of ferricyanide/ferrocyanide increases again. Immunochemical reaction of OTA molecules with the antibody film determined a decrease in the Faradaic response. It was observed also an increase in the peak-to-peak separation between the cathodic and anodic waves of the redox probe, indicating that the electron-transfer kinetics of ferricyanide/ferrocyanide is obstructed. All the observations are in accordance with results of EIS analyses about studied electrodes and these two techniques allow a good parallel control of the samples [35].

To evaluate the immunochemical reaction between antibody anti-OTA and OTA, we exposed the anti-OTA/BSA-EDC-NHS/Au electrode to various OTA concentrations. It was found an increase for R_{ct} parameter with the adding of OTA (Table 3).

The difference between R_{ct} values before and after incubation with OTA is considered the analytical signal $\Delta R_{ct} = R_{ct}(after)-R_{ct}$ (before). As it can be seen in Fig 3B, there is a steady linear increase in ΔR_{ct} with the OTA concentration. The calibration curve in Fig 4 was further used for determining the OTA concentration in plant extracts samples.

Immunosensor specificity

In this work, we immobilized monoclonal antibody anti-Ochratoxin A from Novus Biologicals (Canada) in order to propose a rapid method for ochratoxin A detection using antibody-immobilized on BSA-functionalized gold electrodes. We chose to do as this because, even that the cost of biosensor could increase, this choosing minimized the cross-reactivity (previous tests were done to check cross reactivity using aflatoxin B1—data not shown in this paper–and no cross-reactivity was observed).

Some control experiments were performed with a sensor fabricated without antibody, aiming to confirm that the impedance changes were indeed due to specific interaction between OTA and its antibody, and were not caused by nonspecific adsorption. This second sensor was prepared using an identical protocol with identical conditions, buffers, concentrations, etc. as used for the specific antibody electrodes.

Fig 4A shows the impedance spectra recorded for a sensor before and after the incubation of 10 ng/mL OTA and Fig 4B for supplemental control experiment that uses antibody-free device. In this last case, no obvious impedance changes were detected upon the incubation with OTA,

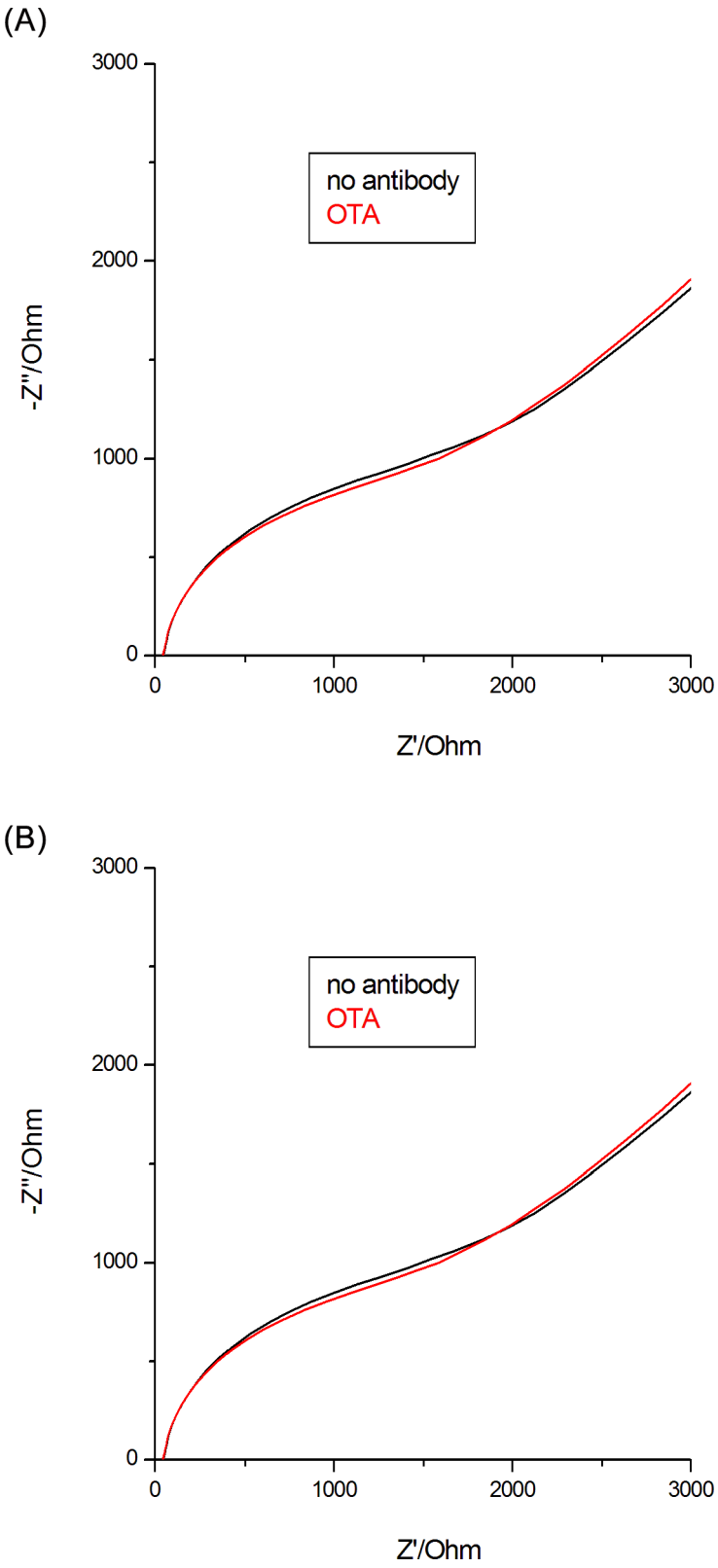

Fig 4. Nyquist plots at 10 mV sinusoidal ac potential perturbation, ferricyanide/ferrocyanide redox couple, for response of sensor with an antibody specific for OTA (A) or of sensor without antibody (B).

doi:10.1371/journal.pone.0160021.g004

Table 4. Values of the equivalent circuit parameters for electrodes with plant extracts.

Sample	Rs (Ω cm^2)	Q (10^{-6}μF)	n	Rct (Ω cm^2)	W (10^{-6} Ω cm^2)	ΔRct (Ω cm^2)
Sample 1 OTA 5 ng/mL	4.01	107	0.87	261	670	122
Sample 2 OTA 10 ng/mL	4.02	153	0.87	409	848	150.5

doi:10.1371/journal.pone.0160021.t004

which confirm that the observed impedance changes are due to specific antibody-OTA interactions.

We have proven the specificity of the interaction with OTA and the fact that non-specific adsorption effects are insignificant by making EIS determinations with a biosensor unmodified with antibody anti-OTA.

OTA detection in plant extracts samples

The liquorice obtained from local market was crushed into mortar with pestle and 1 g of powder was mixed for 6 minutes with 5 mL of acetate buffer (pH 5.6). The mixture was kept at rest for 5 minutes and then was filtered through absorbent filter paper and 0.2 μm Nylon syringe filter. This extract (stock solution) was further diluted 1:1000 in acetate buffer in order to be used for the experiment.

50 μL plant extract was mixed with 50 μL OTA in different concentrations before analysis with the electrochemical immunosensor. A volume of 75 μL of each sample was dropped on the surface of antibody- modified electrodes and allowed to incubate for 30 minutes. The Nyquist diagrams were recorded before and after incubation of the sensors with the plant extracts. The impedance data were fitted to equivalent circuit shown in Fig 2B, and the solution resistance, the electron transfer resistance, the constant phase element and the Warburg impedance element were determined (Table 4).

Using OTA calibration curve and ΔR_{ct} (the difference between R_{ct} values before and after incubation with plant extract) the OTA concentration of plant extracts was determined (Table 5).

In this way, our new label-free, sensitive, cost-effective and fast EIS immunosensor can be utilized for OTA detection. The sensor based on screen-printed gold electrodes was easily modified with a cross-linked film of BSA that further serves as "anchor" for the covalent immobilization of the anti-OTA antibody. The casting of the protective BSA layer on the gold electrode prevents any nonspecific binding between OTA and the gold surface.

The specific interaction between antibody and OTA induces an increase in electron transfer resistance at the interface sensor-solution that is correlated with the concentration of OTA in the sample. The detection of OTA was achieved by EIS on the linear range 2.5–100 ng/mL. Obtained results have the advantage of larger linear range, which include the maximum levels of OTA allowed by EC in various food products and are similar with some others obtained using immunosensors and EIS/SPR detection [36]. The he immunosensor can be further optimized and our next work will consider amplification strategies of the analytical signal in order to improve the sensitivity of this method for OTA detection. One possible future option to optimize the detection of these mycotoxins is the use of aptamers, where Catanante and colab.

Table 5. OTA concentration in spiked plant extracts.

Sample	ΔRct (Ω cm^2)	Concentration OTA (ng/mL)	Recovery degree of OTA (%)
Sample 1	122	4.63	92.6%
Sample 2	150.5	9.82	98.2%

doi:10.1371/journal.pone.0160021.t005

[37] obtained very promising results, with better dynamic range. Another possibility is to employ PEC (label-free photoelectrochemical) platform recommended as strategy for fabrication of label-free biosensor by Yang and colab. [38].

Conclusion

A new label-free immunosensor for ochratoxin A detection was developed. This sensitive, fast and cost-effective sensor based on a screen gold electrode, which was easily modified in order to immobilize the monoclonal antibody anti-OTA, induced an increase in electron transfer resistance at the interface immunosensor-solution that is related to ochratoxin A concentration in the sample. The method could be successfully used for detection of ochratoxin A from plant extracts using bioanalysis and biosensing.

Acknowledgments

The writing of this work has received partial funding from the European Community's Seventh Framework Programme (FP7/2007-2013) under grant agreement n° 245199. It has been carried out within the PlantLIBRA project (website: www.plantlibra.eu). This report does not necessarily reflect the Commission views or its future policy on these areas. LF, MB hereby acknowledge the structural funds project PRO-DD (POS-CCE, O.2.2.1., ID 123, SMIS 2637, ctr. No 11/2009) for access to the infrastructure used in this work, and also the project Bursa Univ. Transilvania 2016 for funding consumables used for the experiments. We would like to thank to Alina Vasilescu and Alis Vezeanu from International Centre of Biodynamics, Bucharest as well as to Arianna Scollo and Aurora Perini from University of Milan, for assistance with preliminary EIS work.

Author Contributions

Conceived and designed the experiments: MB LF PR. Performed the experiments: MB LF. Analyzed the data: SC MM. Contributed reagents/materials/analysis tools: SC MM. Wrote the paper: MB LF PR.

References

1. Amézqueta S, Schorr-Galindo S, Murillo-Arbizu M, González-Peñas E, López de Cerain A Guiraud JP. OTA-producing fungi in foodstuffs: A review. Food Control. 2012; 26:259–8.
2. Gerez CL, Dallagnol A, Ponsone L, Chulze S, Font de Valdez G. Ochratoxin A production by Aspergillus niger: Effect of water activity and a biopreserver formulated with Lactobacillus plantarum CRL 778. Food Control. 2014; 45:115–9.
3. Pfohl-Leszkowicz A, Manderville RA. Ochratoxin A: an overview on toxicity and carcinogenicity in animals and humans. Molecular Nutrition & Food Research. 2007; 51:61–99.
4. Prabu PC, Dwivedi P, Sharma AK. Toxipathological studies on the effects of aflatoxin B1 and ochratoxin A and their interactions in New Zeeland with rabbits. Exp Toxicol Pathol. 2013; 65:277–86. doi: 10.1016/j.etp.2011.09.003 PMID: 22015214
5. Jiang C, Shi J, Chen X, Liu Y. Effect of sulfur dioxide and ethanol concentration on fungal profile and ochratoxin a production by Aspergillus carbonarius during wine making. Food Control. 2015; 47:656–63.
6. Galarce-Bustos O, Alvarado M, Vega M, Aranda M. Occurrence of ochratoxin A in roasted and instant coffees in Chilean market. Food Control. 2015; 46:102–7.
7. Zhao X, Yuan Y, Zhang X, Yue T. Identification of ochratoxin A in Chinese spices using HPLC fluorescent detectors with immunoaffinity column cleanup. Food Control. 2014; 46:332–7.
8. Yogendrarajah P, Jacxsens L, De Saeger S, De Meulenaer B. Co-occurrence of multiple mycotoxins in dry chilli (Capsicum annum L.) samples from the markets of Sri Lanka and Belgium. Food Control. 2014; 46:26–34.

9. Kabak B. Determination of aflatoxins and ochratoxin A in retail cereal products from Turkey by high performance liquid chromatography with fluorescence detection. Food Control. 2012; 28:1–6.
10. Andrés E, Aragunde H, Planas A. Screening glycosynthase libraries with a fluoride chemosensor assay independently of enzyme specificity: identification of a transitional hydrolase to synthase mutant. Biochem. J. 2014; 458:355–63. doi: 10.1042/BJ20131057 PMID: 24341595
11. Gaulitz G, Piebler J, Bilitewski U. Affinity sensor systems. In: Bilitewski U, Turner APF, editors. Biosensors for environmental monitoring. Amsterdam: Harwood Academic Publishers; 2000. p. 150–78.
12. Katz E, Willner I. Probing Biomolecular Interactions at Conductive and Semiconductive Surfaces by Impedance Spectroscopy: Routes to Impedimetric Immunosensors, DNA-Sensors, and Enzyme Biosensors. Electroanalysis. 2003; 15(11):913–47.
13. Alonso-Lomillo MA, Domínguez-Renedo O, Ferreira-Gonçalves L, Arcos-Martínez MJ. Sensitive enzyme-biosensor based on screen-printed electrodes for Ochratoxin A. Biosensors and Bioelectronics. 2009; 10:1333–7.
14. Kaushik A, Solanki PR, Ansari AA, Ahmad S, Malhotra BD. Chitosan–iron oxide nanobiocomposite based immunosensor for ochratoxin-A. Electrochem. Commun. 2008; 10:1364–8.
15. Alarcón SH, Palleschi G, Compagnone D, Pascale M, Visconti A, Barna-Vetró I, Monoclonal antibody based electrochemical immunosensor for the determination of ochratoxin A in wheat. Talanta 2006; 69:1031–7. doi: 10.1016/j.talanta.2005.12.024 PMID: 18970676
16. Yu JCC, Lai EPC. Polypyrrole film on miniaturized surface plasmon resonance sensor for ochratoxin A detection. Synth. Met. 2004; 143:253–8.
17. Adànyi N, Levkovets IA, Rodriguez-Gil S, Ronald A, Váradi M, Szendro I. Development of immunosensor based on OWLS technique for determining aflatoxin B1 and ochratoxin A. Biosens. Bioelectron. 2007; 22:797–802. PMID: 16600588
18. Sapsford KE, Ngundi MM, Moore MH, Lassman ME, Shriver-Lake LC, Taitt CR, et al. Rapid detection of foodborne contaminants using an array biosensor. Sens. Actuat. B. 2006; 113:599–607.
19. Ngundi MM, Shriver-Lake LC, Moore MH, Lassman ME, Ligler FS, Taitt CR. Array biosensor for detection of ochratoxin A in cereals and beverages. Anal. Chem. 2005; 77:148–54. PMID: 15623290
20. Tsai WC, Hsieh CK, QCM-based immunosensor for the determination of ochratoxin A. Anal. Lett. 2007; 40:1979–91.
21. Taleat Z, Ravalli A, Mazloum-Ardakani M, Marrazza G. CA 125 Immunosensor Based on Poly-Anthranilic Acid Modified Screen-Printed Electrodes. Electroanalysis. 2013; 25:269–77.
22. Liu G, Iyengar SG, Gooding JJ. An Electrochemical Impedance Immunosensor Based on Gold Nanoparticle-Modified Electrodes for the Detection of HbA1c in Human Blood. Electroanalysis. 2012; 24:1509–16.
23. Siddiqui S, Dai Z, Stavis CJ, Zeng H, Moldovan N, Hamers RJ, et al. A quantitative study of detection mechanism of a label-free impedance biosensor using ultrananocrystalline diamond microelectrode array. Biosensors and Bioelectronics. 2012; 35(1):284–90. doi: 10.1016/j.bios.2012.03.001 PMID: 22456097
24. Suni II. Impedance methods for electrochemical sensors using nanomaterials. Trends in Analytical Chemistry. 2008; 27(7):604–11.
25. Daniels JS, Pourmand N. Label-Free Impedance Biosensors: Opportunities and Challenges. Electroanalysis. 2007; 19:1239–57. PMID: 18176631
26. Radi AE, Munoz-Berbel X, Lates, Marty JL. Label-free impedimetric immunosensor for sensitive detection of ochratoxin A. Biosensors and Bioelectronics. 2009; 24:1888–92. doi: 10.1016/j.bios.2008.09.021 PMID: 19013783
27. Papamichael KI, Kreuzer MP, Guilbault GG. Viability of allergy (IgE) detection using an alternative aptamer receptor and electrochemical means. Sensors and Actuators B: Chemical. 2007; 121(1):178–86.
28. Hayat A, Sassolas A, Marty JL, Radi AE. Highly sensitive ochratoxin A impedimetric aptasensor based on the immobilization of azido-aptamer onto electrografted binary film via click chemistry. Talanta. 2013; 15(103):14–9.
29. Vidal JC, Bonel L, Ezquerra A, Duato P, Castillo JR. An electrochemical immunosensor for ochratoxin A determination in wines based on a monoclonal antibody and paramagnetic microbeads. Anal Bioanal Chem. 2012; 403(6):1585–93. doi: 10.1007/s00216-012-5951-5 PMID: 22466259
30. Prabhakar N, Matharu Z, Malhotra B.D. Polyaniline Langmuir-Blodgett film based aptasensor for ochratoxin A detection. Biosens Bioelectron. 2011; 26(10):4006–11. doi: 10.1016/j.bios.2011.03.014 PMID: 21514815

31. Solanki PR, Kaushik A, Manaka T, Pandey MK, Iwamoto M, Agrawal VV, et al. Self-assembled monolayer based impedimetric platform for food borne mycotoxin detection. Nanoscale. 2010; 2(12):2811–7. doi: 10.1039/c0nr00289e PMID: 20953508

32. Ansari AA, Kaushik A, Solanki PR, Malhotra BD. Nanostructured zinc oxide platform for mycotoxin detection. Bioelectrochemistry. 2010; 77(2):75–81. doi: 10.1016/j.bioelechem.2009.06.014 PMID: 19648064

33. Polonschii C, David S, Tombelli S, Mascini M, Gheorghiu M. A novel low-cost and easy to develop functionalization platform. Case study: Aptamer-based detection of thrombin by surface plasmon resonance. Talanta. 2010; 80:2157–64. doi: 10.1016/j.talanta.2009.11.023 PMID: 20152466

34. Bard AJ, Faulkner LR. Electrochemical Methods: Fundamentals and Applications. New York: Wiley and Sons; 2007.

35. Bogomolova A, Komarova E, Reber K, Gerasimov T. Challenges of Electrochemical Impedance Spectroscopy in Protein Biosensing. Analytical Chemistry. 2009; 81(10):3944–49. doi: 10.1021/ac9002358 PMID: 19364089

36. Zamfir G, Geana I, Bourigua S, Rotariu L, Bala C, Errachid A, Jaffrezic-Renault N, Highly sensitive label-free immunosensor for ochratoxin A based on functionalized magnetic nanoparticles and EIS/SPR detection L Sensors and Actuators B: Chemical, 2011, 159, 178–184.

37. Catanante G, Mishra RK, Hayat A, Marty JL, Sensitive analytical performance of folding based biosensor using methylene blue tagged aptamers., Talanta. 2016; 153:138–44. doi: 10.1016/j.talanta.2016.03.004 PMID: 27130100

38. Yang J, Gao P, Liu Y, Li R, Ma H, Du B, Wei Q., Label-free photoelectrochemical immunosensor for sensitive detection of Ochratoxin A., Biosens Bioelectron. 2015; 64:13–8. doi: 10.1016/j.bios.2014.08.025 PMID: 25173733

RoboSmith: Wireless Networked Architecture for Multiagent Robotic System

doi:10.3991/ijoe.v6i4.1468

D. Floroian, D. Ursutiu, F. Moldoveanu and L. Floroian
Transilvania University of Brasov, Romania

***Abstract*—In this paper it is presented an architecture of a flexible mini robot in a multiagent robotic system wireless commanded. In a multiagent system the value of an individual agent is negligible since the goal of the system is essential. Thus, the agents (robots) need to be small, low cost and cooperative. RoboSmith is designed based on these conditions. The proposed architecture divides a robot into functional modules such as locomotion, control, sensors, communication, and actuation. Any mobile robot can be constructed by combining these functional modules for a specific application. Embedded software with dynamic task uploading and multi-tasking abilities is developed in order to create better interface between both robots and the command center and between the robots. The dynamic task uploading allows the robots change their behaviors in runtime. The flexibility of the robots is given by the fact that the robots can work in multiagent system, as master-slave, or hybrid mode, they can be equipped with different modules and they may be used in other applications such as mobile sensor networks remote sensing and plant monitoring.**

***Index Terms*—wireless network, intelligent agents, mobile robot, intelligent architecture.**

I. INTRODUCTION

The main goal of this work is to develop a flexible mini robot that to be used in implementation of a multiagent robotic system, and to present the software architecture. The nature of the multiagent systems (even if applied in robotics) brings some limitations and conditions to the design of a reliable platform [1, 5, 11, 13, 14]. The size, the cost, and the cooperative abilities via specific tools are some of the limitations and conditions. The size and cost limitations are closely related since smaller size means less material and thus less cost. With the advances in microelectronics fabrication technologies, the size and the cost of the chip used in the systems decreased significantly, which allows the designers to meet the cost limitation. Even though the electronic components have become smaller significantly, the mechanical parts and the battery sizes are still reasonably large. The size limitation on a mini robot is imposed by mostly the mechanical parts and the batteries [3, 6, 9]. The fundamental problem with reducing the size of the mechanical devices is that they become inefficient or not fully functional when their size is shrunken. For example, when the size of a DC motor or of a gear gets smaller, their power and their durability are reduced significantly. These limitations have determined our design.

There have been many definitions of a robot in the literature since the beginning of the robotics field in the 1940s. After they have been introduced in the factories, the robots became mobile and smaller with the progresses made in mechanical and electrical engineering fields. After the mobility of the robots was developed, the artificial intelligence field brings its contribution to robotics by making them autonomous and smarter [2, 4, 8, 12].

The multiagent systems represents a relatively new area in the computer science and a very new area in robotics, which started to be developed in 1980s but that only in the mid-1990s gained widespread interest [5, 7, 14, 16]. The multiagent systems are compositions of computing elements that possess autonomous action, and which are able to interact among themselves, not only for exchanging messages but also for a more elaborated kind of communication that resembles social activity (cooperation, coordination, negotiation, etc.).

The robot autonomy requires good communication and sensing skills. These skills can be achieved using multiagent technology, which uses agentified components. Also this problem can be approached by using conventional elements of the robot not necessarily by agentifying the whole robot [1, 12, 16].

The robots need sensors mainly for many reasons. First, the sensing is the purpose of the mission. Second, the sensing is necessary for survival in the robot's environment: e.g. to determine an obstacle on the planned path to the target. Finally, the sensing is needed to enable the robots to sense their own configurations and their relationships with the environment. Once with sensing, a robot needs to make decisions (to think) to be able to adapt to the environment and to change the environment according to the mission [4, 10, 15].

No machine can survive in an environment without proper feedback from it. The mechanical and sensor errors can easily accumulate and put the robot in a dangerous situation. Thus, cognition is essential for robots' survival. Acting is another essential requirement for the evolution of intelligence. Acting is an ability to act on the environment, to survive and accomplish the mission. Manipulation and mobility are key components of action even though they may not be necessary at the same time for small robots. Most of the time, mobility is enough for small robots to accomplish the mission. This changes the current image of a robot from "one-armed iron-laborer" to "a mobile creature" mostly moved by wheels. In recent years, special attention has been given to robots mostly inspired from the nature (e.g. from human cooperation).

The multiagent society is encouraged by the human society. The cooperation between agents let them accomplish a complex mission with their rather limited skills. This type of behavior brings the communication component to the picture because the robots can cooperate with each other only with effective communication between them. A

considerable number of papers have been devoted to these topics [1, 5, 10, 12, 13, 14, 16].

The organization of the paper is as follows. A flexible design architecture based on the multiagent technology is described in Section II. Then, in Section III, a modular mini robot is described following the concepts presented above. In Section IV is presented the robotic multiagent system, RoboSmith, which links together the mini robots. Finally, Section V gives the conclusions.

II. FLEXIBLE DESIGN ARCHITECTURE

There has been a significant amount of research in the reconfigurable, modular and flexible robotics in the recent years [4, 6, 12]. Most researches have been done on the multiple identical modules that construct a single robot. The proposed architecture has a vertical modularity based on the horizontal layers multiagent architecture in which the layers are not identical one to another. It slices a robot into functional abstract layers such as locomotion, control, sensors, communication and actuation.

These concepts avoid main disadvantages of the horizontal layering (which require control of race conditions over the actuators) because there is a single agent which controls the actuators. Any mobile robot can be constructed by combining the above layers for a specific application. A sub-module is a piece of hardware which accomplishes the functionality of an abstract functionality (and also provides the skilling for respective agent), i.e. a wireless communication sub-module for a communication layer.

In our flexible architecture, the robot can be built by combining a locomotion layer, the sensory layers, an actuator layer, and the purpose specific layers. The software flexibility is given by the multiagent technology. Fig. 1 presents the proposed hardware layers and Fig. 2 presents the software functionality [12].

In this model, each layer can be implemented by the corresponding hardware. For example, a sensor layer may be an ultrasound sensory board or a proximity sensory board, or perhaps both. The sub-modules are designed such that they have a unique signature and a standard pin connection. The sub-modules can be added at any level and the position does not affect its module's operation.

Since the layers can be combined in any order, an application specific robot can be quickly constructed. For example, if a new problem domain requires legs rather than wheels, the wheeled sub-module can be instantly swapped with the legged sub-module. Also, in the software application, the wheels agent is replaced by legs agent. This is essential for the flexibility of the applications since agents might be equipped with complementary skills instead of having the same skills.

The programming of the applications in robotics is far from standardized. The primary reason is that each robot is composed of very special hardware designed for a specific goal. The result is that the software also becomes specific. This is very convenient to the multiagent systems which promote the reengineering instead of reprogramming. Also the layers architecture can be easily implemented in the multiagent systems. The communications between agents are standardized by FIPA (Foundation of Intelligent Physical Agents) regulations. These facts make the multiagent technology to be very useful in this situation.

A layered architecture is simultaneously reactive and deliberative. The agents deliberate and make decisions based on the symbolic representation (model) they have on the external world. These agents make more effort to model the complex entities of the external world. The reactive agents suppose the existence of basic behaviors or sequences of actions that execute concurrently from the lowest level of intelligence. These behaviors are, in turn, used by more complex ones to create more complex levels of intelligence. A layered architecture contains a set of interacting layers in which some are deliberative and others are reactive. In horizontal layering the sensors are directly connected to each of existing layers, which also might drive output directly.

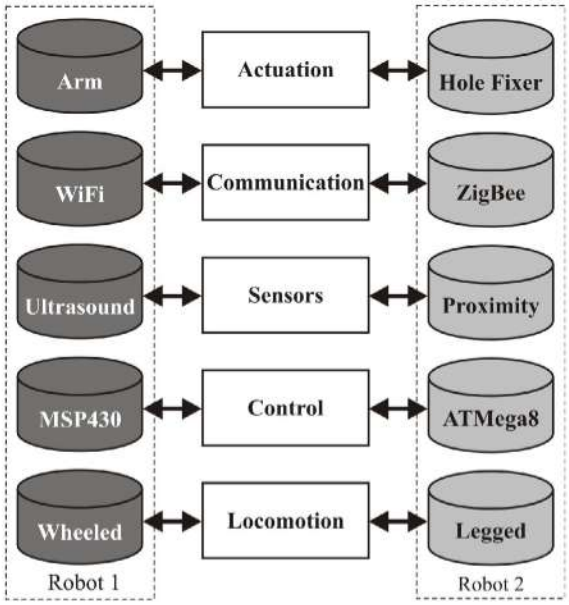

Figure 1. Flexible hardware structure.

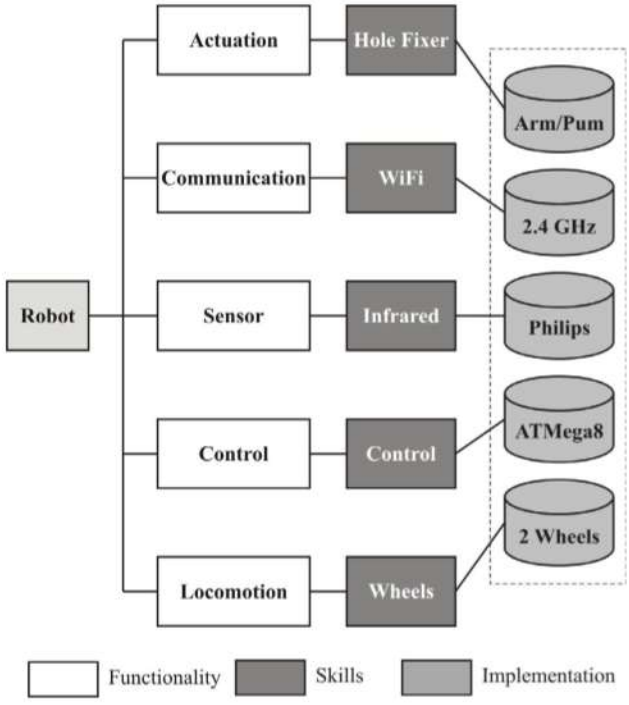

Figure 2. Flexible software structure.

The focus on this section moves from the architecture of the flexible mini robot to the architecture where a group of agents create a form. Individual agents are useless in the large majority of situations, because most scenarios involve several interacting agents. When dealing with multiagents the important aspects are to know how they communicate and how they interact. The communication and the interaction are the mechanisms that let the community of agents to have a more complex behavior than just the sum of their individual behaviors (see Fig. 3).

For the implementation of multiagent systems we will use JADE (Java Agent Development Environment) which is a middleware platform intended for the development of distributed multiagent applications based on peer-to-peer communication [17]. JADE includes Java classes to support the development of application agents and the run-time environment that provides the basic services for agents to execute. An instance of the JADE run-time is called a *container*, and the set of all containers is called the *platform*. These platforms provide the layers that hide from agents the complexity of the underlying execution system. This mechanism is depicted in Fig. 4.

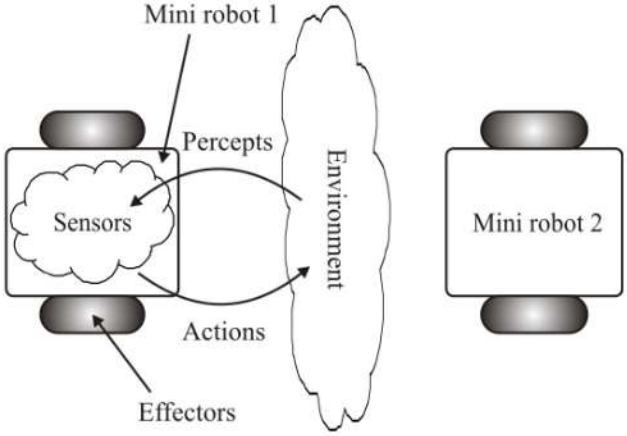

Figure 3. Agents interactions with the environment.

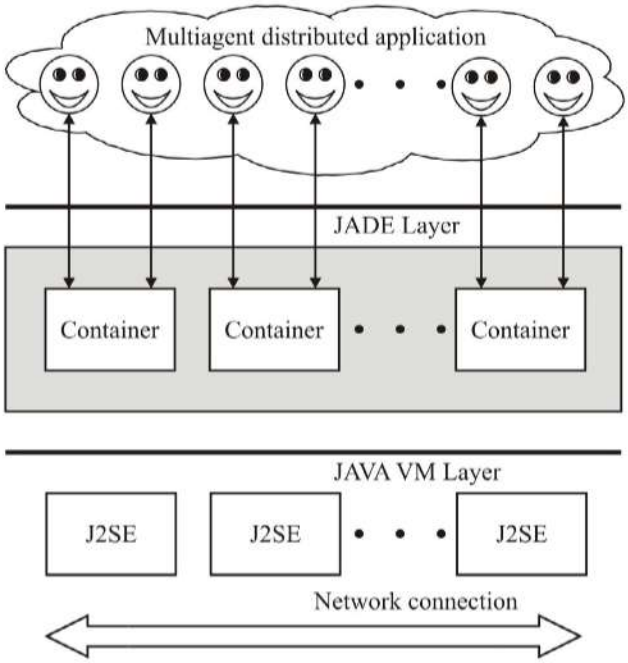

Figure 4. The JADE architecture.

III. THE MINI ROBOT

The RoboSmith's robots are flexible mini robots, which take the advantage of a layered design approach described in Section II. Even though there are five levels in the hardware and software architectures, the implementations (sub-modules) of the levels can be more than one. In addition, each level may also involve multiple closely related functionalities. The sub-modules are designed and manufactured at the Automation Laboratory. This section presents the mini robot and main sub-modules.

The locomotion module has a mechanical base and locomotion module hardware (sub-module). The base of the robot consists of an aluminum frame, two stepper motors, some gearing, two wheels and associated ball bearings, and the batteries. The base is designed by CAD tools and machined with high precision CNC machines. Fig. 5 shows the base with wheels, gears and motors. A legged version of the base is also in design process as an alternative locomotion to be used in different applications. The battery selected for the mini robot is an AA form factor NiMH rechargeable cell. Four of these cells connected in series are used in the system. The cells are nominally 1.2 volts each for 4.8 volts system voltage.

The two wheels module is very versatile and easily direction able. This mechanism allows the robot to make short turns by moving only a wheel and stopping the other. Another advantage is providing by the sensors. The time delay is not critical because, in this situation, the locomotion module has plenty of time to turn and the control module has plenty of time to make decisions.

The locomotion layer is implemented by first electronic module and the mechanical base described above. It's the most critical layer in the operation of the robot. It contains the circuit for the stepper controller, which provides the direction control for the motors and supplies the high current they require. This module is also manufactured in laboratory and includes common components. It also includes the power system, which consists of a DC-DC converter and some passive components. The power system provides +5 volts for the entire robot, and will accept from 1.5 - 15 volts on its input. This provides plenty of flexibility if a different battery system is put in place. This sub-

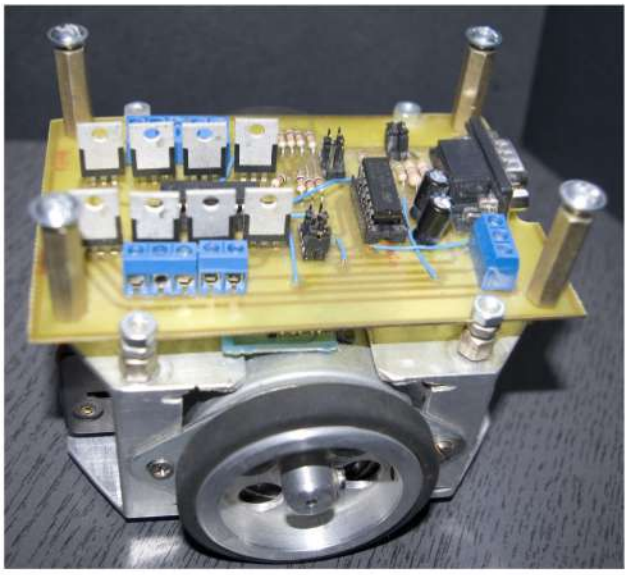

Figure 5. The base with wheels for flexible mini robot.

module also contains the charge circuit, which allows the battery to remain in the robot while it is recharged (see Fig. 6). Also by choosing the high capacity elements the robot has greater autonomy.

Over on this sub-module (as seen in Fig. 7), it is the main controller, an ATMega8 microcontroller running at 16 MHz. The 8 kB flash memory is included on the chip and also 512 B RAM and 1 kB SRAM. All other components are soldered directly to the board. Having improvements of the memory architecture, the mini robots are able to run in a flexible architecture.

At the top, the sub-module for communication layer is based on an XBee hardware board (serial version) (which is very similar to familiar ZigBee modules) [19]. This is necessary for the agent's interactions and for reporting to the main server unit which is hosted on a PC (see Fig. 8.). Another XBee module (an USB version this time) is connected to a host PC and connects the mini robot to the control program. Also many mini robots (a maximum of 16 is recommended) equipped with XBee module can be interconnected in this manner. The control program will coordinate the messages.

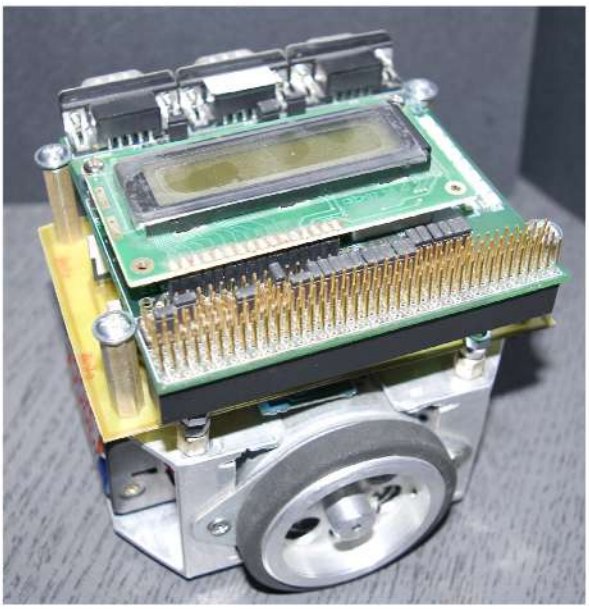

Figure 6. Implementation of locomotion layer of flexible mini robot.

IV. THE MULTIAGENT ROBOTIC SYSTEM

The RoboSmith architecture is based on a multiagent robotic system which coordinates the entire community of agents. This section presents the implementation of the RoboSmith architecture.

The RoboSmith is a networked organization of mini robots that have formed together a cooperative dynamic network to reach group benefits. RoboSmith is a society of agents (the mini robots) and therefore their interactions are at society level. The mini robots can be considered intelligent agents because they are proactive, reactive and have social ability. They are proactive since they have goal directed behavior that is seen when the layers involved participate in society with the best possible performance. Moreover, they can keep working even under the environmental coalitions. They are reactive in the sense that they react to changes in the external environment, which are "sensed" through messages. Although the RoboSmith agents are not purely reactive, the importance of messages in their behavior is so relevant that their architecture is more reactive than proactive. Finally, they have social ability because they are able to negotiate and to cooperate with the other mini robots.

Figure 7. Mini robot's CPU.

The communication and the interaction among individuals or within some domains can only take place if there is some of the conceptualisation of these domains. To guarantee a common semantic understanding, agents must use appropriate ontology to communicate with their partners. In the case of the RoboSmith, all the mini robots need to share some basic concepts, such as skills, requests, services and agent. Therefore all agents of the proposed architecture share a basic global ontology that patterns the basic referred concepts.

For our purposes, we have adopted the description of an agent as a software program with the capabilities of sensing, computing, and networking associated with the specific skills of the mini robots described above. This implementation is made in JADE because this development tool is very versatile and could be very well integrated with others development tools (like Protégé-2000 and Java [17, 18]). Also JADE is an open source FIPA compliant Java

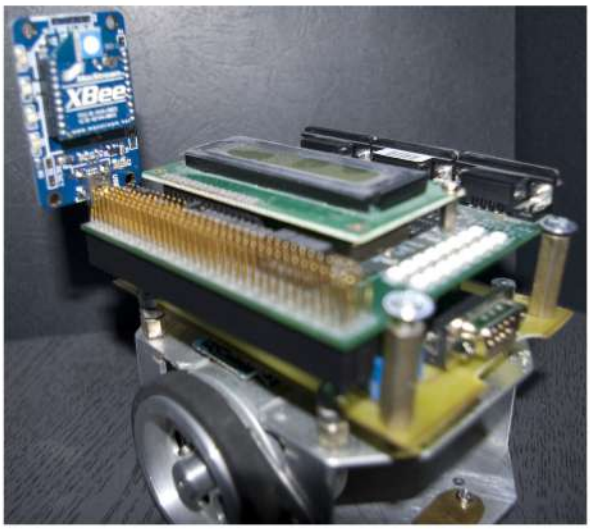

Figure 8. Implementation of hardware communication layer.

based software framework for the implementation of the multiagent systems. It simplifies the implementation of the agent communities by offering runtime and agent programming libraries, as well as tools to manage platform execution and monitoring and debugging activities. These supporting tools are themselves FIPA agents.

JADE offers simultaneously middleware for FIPA compliant multiagent systems, supporting application agents whenever they need to exploit some feature covered by the FIPA standard (message passing, agent life cycle, etc.), and a Java framework for developing FIPA compliant agent applications, making FIPA standard assets available to the programmer through Java object-oriented abstractions. The general management console for a JADE agent platform (RMA – Remote Monitoring Agent), like in Fig. 9, acquires the information about the platform and executes the GUI (Graphic User Interface) commands to modify the status of the platform (creating new agents, shutting down containers, etc) through the AMS (Agent Management System). The agent platform can be split between several hosts (provided that there is no firewall between them). The agents are implemented as one Java thread and Java events are used for effective and lightweight communication between agents on the same host. The parallel tasks can be still executed by one agent, and JADE schedules these tasks in a more efficient (and even simpler for the skilled programmer) way than the Java Virtual Machine (VM) does for threads. Several Java VM, called containers in JADE, can coexist in the same agent platform even though they are not running in the same host as the RMA agent. This means that a RMA can be used to manage a set of VMs distributed across various hosts. Each container provides a complete run time environment for the agent execution and allows several agents to concurrently execute on the same host. The DF (Directory Facilitator), AMS, and RMA agents coexist under the same container (main-container) together with the RoboSmith's agentified mini robots, as it is shown in Fig. 9.

To facilitate message reply, which, according to FIPA, must be formed taking into account a set of well-formed rules such as setting the appropriate value for the attributes *in-reply-to*, using the same *conversation-id*, etc., the method *createReply*() is defined in the class that defines the ACL (Agent Communication Language) message. Different types of primitives are also included to facilitate the implementation of content languages other than SL (Standard Languages), which is the default content language defined by FIPA for ACL messages. This facility is made with Protégé 2000 as depicted in Fig. 10.

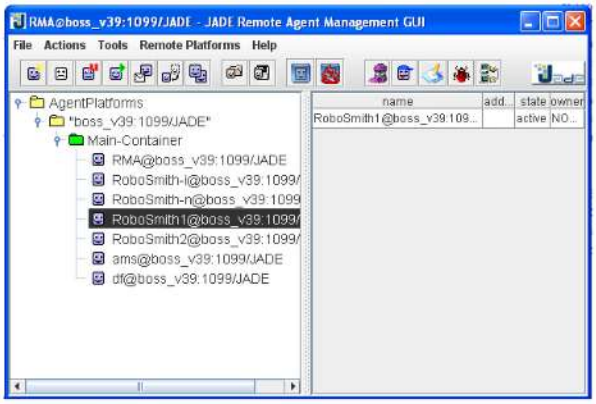

Figure 9. JADE Implementation of RoboSmith.

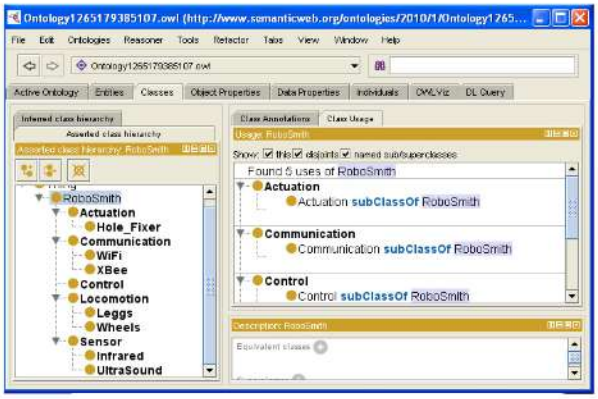

Figure 10. Defining ontologies for RoboSmith.

In Fig. 11 is presented a graphical view of ontology classes which facilitate understanding the fact that from the point of view of the programmer, a JADE agent is simply a Java class that extends the base *agent* class. It allows inheriting a basic hidden behavior (such as registration, configuration, remote management, etc.), and a basic set of methods that can be called to implement the application tasks of the agent (i.e. send/receive ACL messages).

Moreover, the user agents inherit from their Agent superclass some methods to manage agent behaviors. Also this diagram can be represented in UML (Unified Modeling Language) because behaviors are implemented as hierarchy of the classes.

The Protégé 2000 connects to RoboSmith JADE Agents by including a Protégé configuration file in the Java compiler. The RoboSmith ontology is divided in many concepts that follows the class hierarchy defined above.

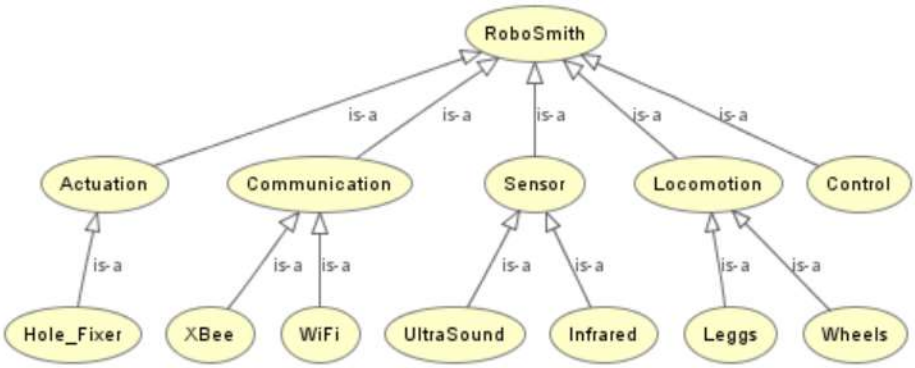

Figure 11. Classes hierarchy for RoboSmith architecture.

V. CONCLUSIONS

In this paper, the exploitation of the multiagent technology applied in flexible mini robotic system has been presented. A number of two robots were constructed and were implied in multiagent robotic system. It is possible to extend this number by adding similar robots.

The results presented confirmed the theoretical predictions made during the design phase. The proper function of the robotic system is important from a practical point of view since it provides a detailed framework about the design of the control structure and the behaviors tasks. This confirm that multiagent technology can be successfully implemented to control the robotic systems.

REFERENCES

[1] J. Barata, and L.M. Camarinha-Matos, "Multiagent Coalitions of Manufacturing Components for Shop Floor Agility – The CoBaSA Architecture", *Int. J. Networking and Virtual Organisation*, 2(1), pp.50-77, 2003. doi:10.1504/IJNVO.2003.003518

[2] B.S. Choi, J.J. Lee, "Localization for a mobile robot based on an ultrasonic sensor using dynamic obstacles", *J. Artificial Life and Robotics*, vol. 12, Springer Japan, pp. 280-283, March, 2008.

[3] V. Denneberg and P. Fromm, "OSCAR. An open software concept for autonomous robots", *Proc. of the 24th Annual Conference of the IEEE Industrial Electronics Society*, pp. 1192-1197, sep. 1998.

[4] L. Feng, J. Borenstein, and H. R. Everett, "*Where am I? Sensors and Methods for Autonomous Mobile Robot Positioning*", vol. 3, The University of Michigan, 1994, pp. 9-10.

[5] D., Floroian, *Multiagent Systems*, Cluj-Napoca (Romania), Ed. Albastra (In Romanian), 2009.

[6] W. Jueyao, Z. Xiaorui, T. Fude, Z. Tao, et al., "Design of a Modular Robotic System for Archaeological Exploration", *Int. Conf. on Robotics and Automation*, Kobe, Japan, pp. 1435-1440, 2009. doi:10.1109/ROBOT.2009.5152364

[7] T. Komatsu and N. Kuki, "Investigating the Contributing Factors to Make Users React Toward an On-screen Agent as if They are Reacting Toward a Robotic Agent", *18th IEEE Int. Symp. Robot and Human Interactive Communication*, Toyama, Japan, Sept. 2009. doi:10.1109/ROMAN.2009.5326350

[8] D., Lee, W., Chung, "Discrete-status-based Localization for Indoor Service Robots", *IEEE Trans. Ind. Electron.* Vol. 53, No. 5, Oct. 2006, pg.:1737–1746. doi:10.1109/TIE.2006.881949

[9] W.H. Lee and A.C. Sanderson, "Dynamics and distributed control of modular robotic systems", *Proc. of the 26th Annual Conference of the IEEE Industrial Electronics Society*, pp. 2479-2484, sep. 2000.

[10] W.J. Opp and F. Sahin, "An Artificial Immune System approach to Mobile Sensor Networks and Mine Detection", *IEEE SMC 2004, the Hauge*, Netherlands, oct. 2004.

[11] E., Petriu, T., Whalen, R., Abielmona, A., Stewart, "Robotic Sensor Agents: A New Generation of Intelligent Agents for Complex Environment Monitoring", *IEEE Instrum. Meas. Mag.*, Vol. 7, No.3, Sep. 2004, pg.:46–51. doi:10.1109/MIM.2004.1337913

[12] F. Sahin, "GroundScouts: Architecture for a Modular Micro Robotic Platform for Swarm Intelligence and Cooperative Robotics", *Int Conf. Syst., Man & Cyb.*, 2004, pp.929-934.

[13] D. Weyns, H. V. D. Parunak, F. Michel, T. Holvoet, and J. Ferber, "Environments for Multiagent Systems State-of-the-Art and Research Challenges", *E4MAS* 2004 *Springer-Verlag*, Berlin, pp. 1–47, 2005.

[14] M., Wooldridge, N.R., Jennings, "Agent Theories, Architectures, and Languages: A Survey", Proc. *ECAI-Workshop on Agent Theories, Architectures and Languages*, Amsterdam (The Netherlands), Aug. 1994, pg.:145–160.

[15] J., Zheng, P., Lorenz, P., Dini, "Guest Editorial: Wireless Sensor Networking", *IEEE Netw.*, Vol. 20, No. 3, May/Jun. 2006, pg.:4–5. doi:10.1109/MNET.2006.1637925

[16] S.A. Suboting and Al. A. Oleinik, "Multiagent Optimization Based on the Bee-Colony Method", *Cybernetics and Systems Analysis*, Vol. 45, No. 2, 2009.

[17] ***, Java Agent Development Framework – JADE, ´http://jade.tilab.com/

[18] ***, Protégé 2000, http://protege.stanford.edu/

[19] ***, XBee, http://www.digi.com

AUTHORS

D. Floroian, D. Ursutiu, F. Moldoveanu and L. Floroian are with Transilvania University of Brasov, Romania.

Submitted October 4th, 2010. Published as resubmitted by the authors October 17th, 2010.